AN ABSTRACT OF THE THESIS OF

Shane P. Lorona for the degree of Master of Science in Chemical Engineering presented on March 11, 2019.

Title: Investigation of the Initial Stages of SiGe(001) Dry Thermal Oxidation Using Ambient-Pressure X-ray Photoelectron Spectroscopy

Abstract approved: _____

Gregory Herman

Ambient-pressure X-ray photoelectron spectroscopy has been used to study the initial stages of dry thermal oxidation of $Si_{0.60}Ge_{0.40}$(001) grown epitaxially on Si(001). Chemical state resolved AP-XPS was performed at temperatures up to 300 ˚C and O_2 pressures up to 1 mbar. Comparisons were made to Si(001) and Ge(001). The Si 2p and Ge 3d core levels were monitored to study oxide growth *in-situ*. Experimental data was analyzed using the NIST Simulated Electron Spectra for Surface Analysis (SESSA) to determine oxide composition and thickness. Our analysis indicates that oxidation proceeds via three oxide growth rate regimes: rapid regime within the first 20 minutes of oxidation when the oxide was thin, a transitionary regime, and a quasi-saturated slow regime when the oxide was relatively thick. The oxidation of both Si and Ge during the rapid regime was found to be pressure dependent, where both rates decreased at lower O_2 pressures. The rapid regime oxidation rate for Ge was reduced compared to Si at lower O_2 pressures, resulting in significant suppression of GeO_2 formation compared to SiO_2. Results indicate that the rapid regime oxide growth rate at 300 ˚C was 96 and 65 Å/h for O_2

pressures of 1 and 0.01 mbar, respectively. This rapid regime rate was primarily driven by SiO_2 formation. At low pressure, significantly less Ge was incorporated into the oxide and the final oxide thickness was ~5 Å thinner. The Si and Ge oxidation rates in the slow regime were nearly the same for our experimental conditions. The slow regime growth rate at 300 ˚C was 3.3 and 3.9 Å/h for O_2 pressures of 1 and 0.01 mbar, respectively. Finally, the mixed oxide Ge fraction and thickness was found to be strongly dependent on rapid regime oxidation. An enhancement of the $Si_{0.60}Ge_{0.40}(001)$ oxidation rate was observed relative to Si(001) and Ge(001), and this was for both the rapid and slow regimes.

Investigation of the Initial Stages of SiGe(001) Dry Thermal Oxidation Using Ambient-Pressure
X-ray Photoelectron Spectroscopy

By

Shane P. Lorona

A THESIS

Submitted to

Oregon State University

In partial fulfillment of
The requirements for the
Degree of

Master of Science

Presented March 11, 2019
Commencement June 2019

Master of Science thesis of Shane P. Lorona presented on March 11, 2019.

APPROVED:

_____

Major Professor, representing Chemical Engineering

_____

Head of the School of Chemical, Biological, and Environmental Engineering

_____

Dean of the Graduate School

I understand that my thesis will become part of the permanent collection of Oregon State University libraries. My signature below authorizes release of my thesis to any reader upon request.

_____

Shane P. Lorona, author

ACKNOWLEDGEMENTS

I am eternally grateful to my mother, for in my transition to adult life being there to remind me what is truly important and what is not.

None of this would have been possible without Dr. Gregory S. Herman, who took a chance on an unfunded MSc student like me and let him work around the most expensive piece of equipment on campus. I am honored to have been a part of his research group. I would also like to thank J. Trey Diulus, whose expertise in APXPS experiment design, data collection, and analysis made this project possible.

TABLE OF CONTENTS

LIST OF FIGURES

LIST OF FIGURES (Continued)

LIST OF FIGURES (Continued)

LIST OF TABLES

Chapter 1: Silicon-Germanium Heterostructure Transistors and Nanostructuring by Oxidation

1.1   Electron Theory of Semiconductors

A crystal lattice may be thought of as individual atoms in a state of remote separation which are brought together to form a collection of atoms with an equilibrium separation that forms a periodic structure [1]. By the Pauli exclusion principle no two electrons can have the same quantum number so when individual atoms form a crystal lattice each atomic orbital splits into many discrete molecular orbitals on the order of the number of atoms in the solid ($\sim10^{22}$ cm^{-3}) [2]. Since there are so many energy states, they are closely spaced forming a continuum or "band." Core electron orbitals, with a small amount of overlap between adjacent atoms, form narrow and widely spaced bands. The outermost valence electron orbitals significantly overlap with their neighboring atoms forming relatively broad and closely spaced bands, so close as to sometimes overlap. At still higher energies, there can be completely empty bands. Every crystalline solid has its own characteristic band structure; this variation is responsible for the wide range of electrical and optical properties observed in materials [2].

Of importance in determination of electrical conduction properties is the presence of band gaps, or regions where wavelike solutions to the Schrödinger equation do not exist. These forbidden regions arise from the interaction of electron waves with the ion cores of the crystal. This interaction is called Bragg reflection [2]. A metal in band theory has its uppermost band only partially filled with electrons. There is no gap to prevent electrons from jumping from filled states to empty states, so with an applied electric field electrons easily make this jump and conduction results [2]. If the valence electrons exactly fill one or more bands, leaving others empty, the crystal will behave as an insulator. Provided that a filled band is separated by a band

gap from the next higher band, there is no continuous way to change the momentum of the electrons so no conduction results. However, the magnitude of Bragg reflection and size of the band gap depends on the material. A large band gap (>2.0 eV) makes it highly improbable that even under a strong applied electric field that an electron will make the jump from highest occupied molecular orbital to lowest unoccupied molecular orbital; this material is an insulator [2]. When the band gap is small (<2.0 eV), perturbations like energy from light/heat or impurities in the crystal lattice can easily force an electron from a filled valence band into the empty conduction band; this is the general requirement for a semiconducting material [2]. Figure 1.1 shows a schematic of electron occupancy of allowed energy bands for a metal, semi-metal, insulator, and semiconductor. The vertical extent indicates increasing energy states, shaded regions allowed and non-shaded forbidden.
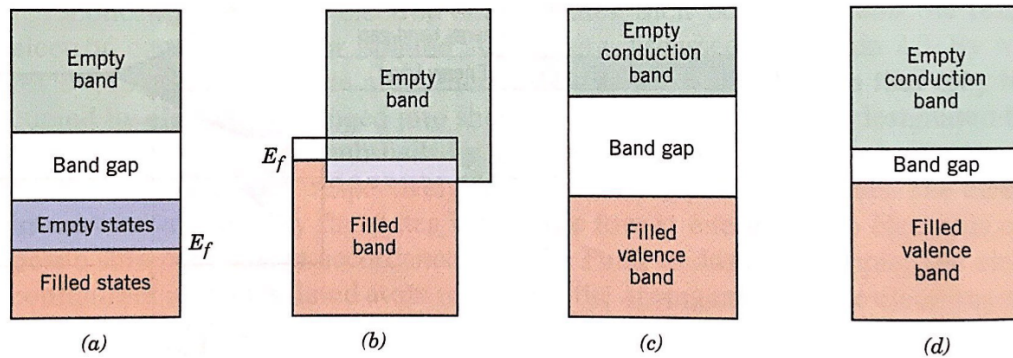
Figure 1.1: Schematic of electron occupancy of allowed energy bands for materials based on band theory (a) a metal, (b) a semimetal where bands overlap in energy leaving two partially filled bands, (c) an insulator, and (d) a semiconductor [3].

There are two distinct types of conduction in semiconductors, intrinsic and extrinsic. In an intrinsic semiconductor, when a valence electron is freed from a broken covalent bond and jumps into the conduction band two types of charge carriers are generated: free electrons and

holes. The number of electrons generated in the conduction band is equal to the number of holes generated in the valence band (hence the word intrinsic, no external source of electrons or holes) [3]. Solid-state theory has shown that these holes act precisely as though they were positively charged electrons with positive mass [1]. It is possible to ignore the electrons entirely, to suppose the band to be completely full, and to treat the holes as a free classical nondegenerate assembly of positive electrons obeying Maxwell-Boltzmann statistics [1]. The number of electrons per unit volume in the conduction band is called the electron-carrier concentration; the number of holes per unit volume in the valence band is called the hole-carrier concentration. In an intrinsic semiconductor these numbers are identical [3]. For pure semiconductors silicon and germanium, germanium has a higher carrier concentration than silicon at all temperatures. This is due to germanium's smaller band gap (0.67 eV versus 1.11 eV), meaning it is significantly easier to thermally excite electrons to the conduction band [3].

To create an extrinsic semiconductor, impurities are added to a pure semiconductor which increases the electrical conductivity by adding to the number of free electrons or holes and producing a mismatch [3]. This process is called doping, where pentavalent dopants like phosphorus or trivalent dopants like boron are added to pure semiconductor like silicon. The main stipulation is that the dopant must be similar enough in size that the doped atoms can fit in the semiconductor lattice without causing too much disorder. When a pentavalent dopant like phosphorus is added to a pure semiconductor like silicon, it is called n-type and has one extra free electron per phosphorus atom in the lattice. In silicon and germanium, these "donor" filled levels lie below and can be very close to (within 0.1 eV) the conduction band [3]. At finite temperatures a donor level may donate its electron to the empty band, leading to increased conduction. When a trivalent dopant like boron is added to a pure semiconductor like silicon, it is

called a p-type and has one extra hole per boron atom in the lattice. In silicon and germanium, these "acceptor" levels lie above and very close to (also within 0.1 eV) the filled valence band. At finite temperatures an acceptor level may accept electrons from the filled band, leaving a hole in the previously filled band [2]. Figure 1.2 shows a graphical representation of dopants in silicon and their associated charges.

(a) (b)
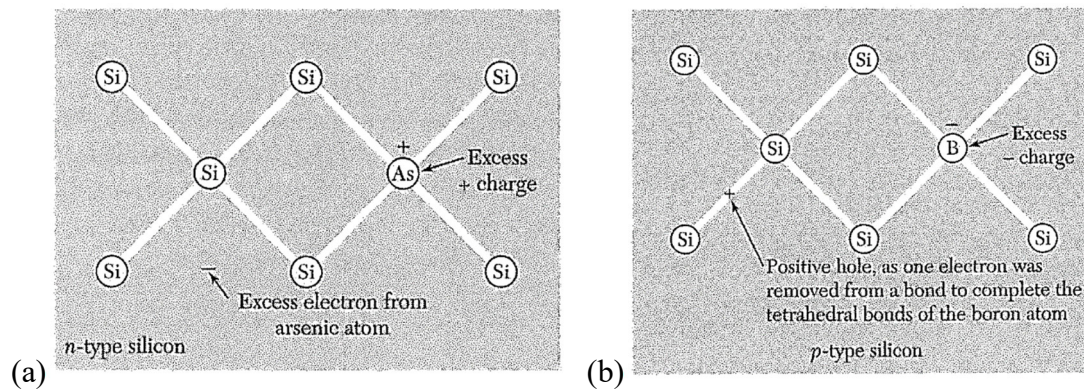
Figure 1.2: Charges associated with (a) an arsenic donor impurity atom in silicon and (b) a boron acceptor impurity atom in silicon. In (a) the excess electron is available for conduction and in (b) the excess positive hole is available for conduction [2].

Both donor and acceptor levels added by dopants increase the electrical conductivity of the material, as charge can be carried by either free electrons or holes. The carrier present in greater number in a semiconductor, the majority carrier, is largely responsible for carrying charge. While understanding the role that electrons and holes play in conduction in semiconductors is simple enough, the exact equations of motion of these charge carriers in valence and conduction bands is not. An electron in a periodic potential (crystal) is accelerated relative to the lattice in an applied electric or magnetic field as if the mass of the electron were equal to an effective mass which can be greater or less than the mass of the isolated electron [2]. This is due an anisotropic electron energy surface near the edges of bands [2].

1.2   Semiconductors in Transistors

In 1947, William Shockley of Bell Telephone Laboratories submitted the first patent for a circuit element utilizing semiconductive material [4]. He proposed manipulating the conduction characteristics, such as the impedance, of a barrier between two portions of a semiconductive body to advantageously alter the flow of current between the two portions [4]. While strides have been made to improve the form factor of these transistors, the fundamental operation remains the same.

Field effect transistors (FET) are essentially electrical switches that have been made with no moving parts by taking advantage of the properties of doped semiconductors. When n-type and p-type semiconductors are placed in electrical contact, free electrons from the n-type material will diffuse to the p-type material to fill the holes [5]. Doped semiconductors are electrically neutral, so when these electrons diffuse over to the p-type material it takes on a negative charge near the area of contact between the two materials. This negative charge screens further free electrons from diffusing, provided it is sufficiently thick to prevent tunneling, and results in the creation of what is called the depletion layer [5]. In a n-type junction FET (JFET), a channel of n-type doped semiconductor serves as a conduit for electron transport from a source to a drain. Two p-type regions are placed on either side of the channel in direct contact to form a "junction", and a small depletion layer exists around each. Without an applied gate bias (V_G), the depletion layer is small and the maximum current flows between the source and drain when there is a voltage between them (V_{DS}) [6]. In other words, the switch is closed (complete circuit). To open the switch (break the circuit), a reverse (-) bias is applied to the two p-type regions increasing the size of the depletion layer such that it prevents current flow from source to drain

[6]. This type of operation is called "depletion mode." The schematic on the left hand side of Figure 1.3 below shows a n-type JFET operating in depletion mode. The depletion layers are not large enough to pinch off current in this case, so the switch is closed as depicted.
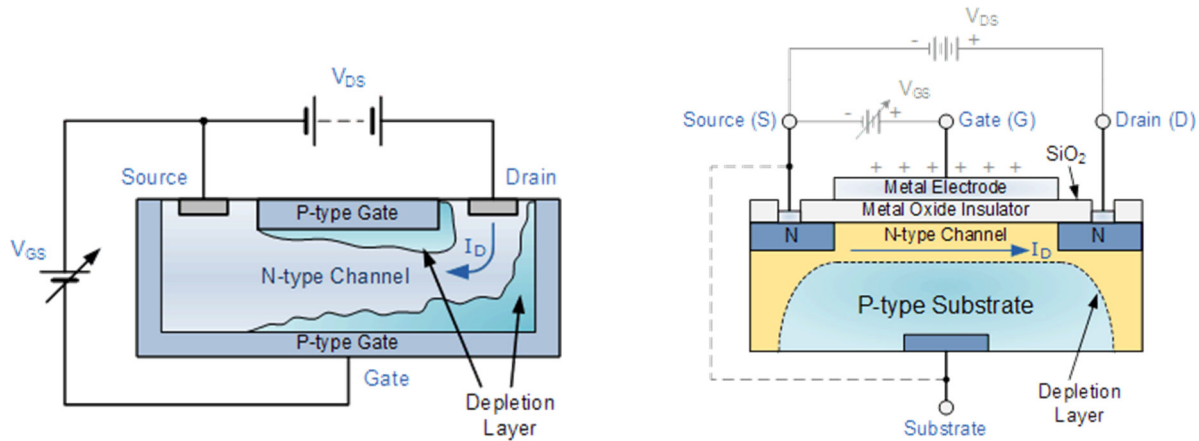
Figure 1.3: Schematic of n-type channel JFET (left) in depletion mode and MOSFET (right) in enhancement mode [Electronics Tutorials, www.electronics-tutorials.ws].

The metal oxide semiconductor FET (MOSFET), on the right in Figure 1.3, is named due to the metal gate electrode being electrically isolated from the rest of the transistor by an ultra-thin oxide layer. The large input impedance at the gate created by the oxide layer results in negligible current flow into the gate, so MOSFETs have almost no gate leakage current [5]. This allows the MOSFET to operate with the gate forward (+) and reverse (-) biased. In an n-type MOSFET like that depicted in Figure 1.3, a positive bias is applied to the gate electrode and builds up capacitance at the oxide insulator/semiconductor interface. This accumulation of positive charge at the gate induces negatively charged electrons to build up in a lightly or undoped p-type region between the n-type source and drain, forming a conductive channel. The result is an enhancement of current from source to drain, or "enhancement mode" operation [5]. The

MOSFET switches to depletion mode simply by changing to reverse bias at the gate electrode [5]. JFETs cannot operate with the gate forward biased due to leakage current; this flexibility is in part why MOSFETs are more widely used than JFETs. MOSFET technology offers high input resistance and is excellent for constructing simple, low-power logic gates [7].

Another important type of transistor is the bipolar junction transistor (BJT). JFETs and MOSFETs are called unipolar transistors because they function with the conduction of electrons alone in an n-type or holes alone in a p-type. Bipolar junction transistors (BJT) function with both types of charge carriers. They accomplish this with two junctions made by three regions of doped semiconductor materials, either NPN (n-type, p-type, n-type) or PNP (p-type, n-type, p-type) [8]. The emitter and collector regions, so named to indicate path of majority carriers, are of the same type but the emitter has a much higher dopant concentration. The base region, which is sandwiched between the emitter and collector regions, is opposite type, lightly doped, and very thin [8]. BJT nomenclature reflects how the regions are arranged: an NPN has a p-type base sandwiched between n-type emitter and collector. Like field effect transistors, depletion zones are created at the junctions between these regions. In normal NPN BJT operation, a forward bias is applied at the emitter-base junction forcing electrons across the depletion barrier and into the base where they become minority carriers. Then, due to differences in doping between emitter and collector the electrons diffuse across the base to the base-collector junction and are assisted across the depletion barrier by a reverse bias [8]. A schematic showing the arrangement of regions and path of electrons and holes in an NPN BJT can be found in Figure 1.4.
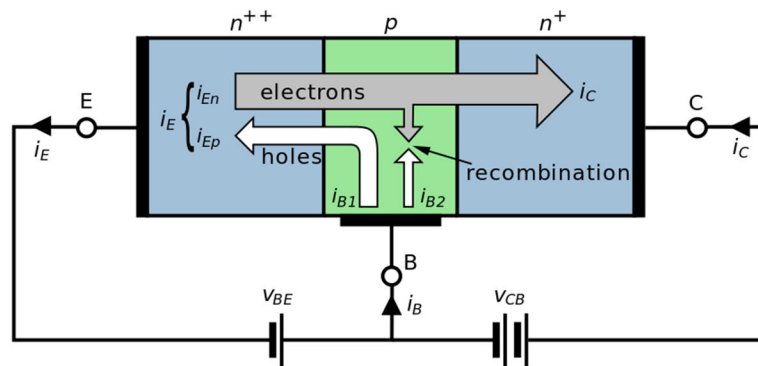
Figure 1.4: Schematic of an NPN bipolar junction transistor showing a high dopant n-type emitter region (E), a physically intermediate p-type base region (B), and low dopant n-type collector region (C). Note: circuit current arrows indicate direction of positive charge ["NPN BJT with forward-biased E–B junction and reverse-biased B–C junction" by Inductiveload, unrestricted].

By design, most of the BJT collector current is due to the flow of charge carriers injected from the high-concentration emitter into the base where they are minority carriers that diffuse toward the collector, so BJTs are classified as minority-carrier devices [9]. While for JFETs and MOSFETs the current flows from source to drain and is controlled by changing voltage at the gate, for BJTs current flows from emitter to collector and is controlled by changing current from base to emitter. More specifically, for an NPN BJT generation of holes in the base which can cross the emitter-base junction and annihilate free electrons can be used to modulate current from emitter to base. This is shown graphically by white arrows in Figure 1.4. Bipolar junction transistors offer high speed, high gain, and low output resistance, which are excellent properties for high-frequency analog amplifiers [7].

An important quantity characterizing the emitter of any BJT is the emitter efficiency defined as the fraction of the total emitter current that is minority-carrier injection current. In order to obtain a high current amplification factor, it is important that the ratio of the injected minority carrier current over the total emitter current be close to unity [10]. Efficiency of carrier injection from the emitter to the base is primarily determined by the doping ratio between the emitter and the base in a transistor made from a single semiconducting element. To encourage carrier injection from emitter to base, the base is lightly doped making its resistance relatively high. High resistance leads to decreased efficiency, which in turn leads to decreased processing speed of the electrical components containing BJTs. First suggested by William Shockley in the same 1947 patent [4] that established semiconductor transistors and later worked into theory by Herbert Kroemer in 1957 [10], the minority carrier injection efficiency can be improved with an emitter than has a wider band gap than the base material. Thus, the heterojunction transistor was born. The central principle is the use of energy gap variations besides electric fields to control the forces acting on electrons and holes, separately and independently of each other. The resulting greater design freedom permits a re-optimization of doping levels and geometries, leading to higher speed devices [11]. Figure 1.5 illustrates how gap design can be used to manipulate carrier mobility.
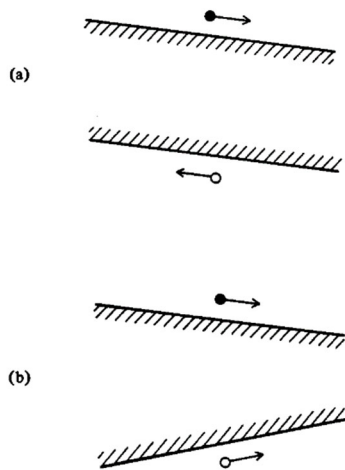
Figure 1.5: Forces on electrons and holes. In a uniform-gap semiconductor (a) the two forces are equal and opposite each other, and equal to the electrostatic force. In a graded gap structure, the forces in electrons and holes may be in the same direction [11].

Many attempts have been made to fabricate such structures. One of the first successful attempts was that by Brojdo et al. [12]. They fabricated structures with current gains of 10 from amorphous CdS deposited upon Si. With the development of close spaced vapor transport epitaxy technology, researchers were able to have more control over transistor materials. Jadus and Feucht [13] obtained current gains of about 15 in GaAs-Ge transistors [14]. In the late 1980s, molecular beam epitaxy and metal-organic chemical vapor deposition led to the first $Si_{1-x}Ge_x$ transistors. However, practical implementation was limited by a low demand due to the wide availability of silicon and the high quality of silicon's oxide. The properties of the Si/SiO_2 material system make it ideally suited for complex digital applications [15]. However, a variety of fast-growing market segments, especially in the areas of millimeter-wave and optical communication, are out of the performance regime allowed due the electronic and optoelectronic properties of Si [15].

1.3   Silicon-Germanium Alloy Heterostructure Transistors

Free electron and hole mobilities are a function of the semiconductor material. These mobilities are essential to the rate at which the transistor can switch, so if the switching speed can be increased then the processing speed of the circuit increases. Modern molecular beam epitaxy and metal-organic chemical vapor deposition techniques have allowed the design of transistors with compositionally tailorable band gaps by using more than one semiconducting material [16], [17]. Recall the central principle in the use of energy gap variations is the modification of electric fields to control the forces acting on electrons and holes, separately and independently of each other [11]. This led to the development of heterojunction transistors including heterojunction field effect transistors (HFET), heterojunction bipolar transistors (HBT), and heterostructure metal-oxide transistors. IBM discovered through the addition of Ge into an Si based BJT that the drive capability increased by a factor of three [18]. This was not achieved using classical HBT design, however.

The side of the unit Si cell, or lattice parameter, is well known from X-ray diffraction to be a_{Si} = 5.431 Å [19]. Germanium's lattice parameter has been found to be a_{Ge} = 5.658 Å [20], which is 4.2% larger than Si. Due to the lattice parameter mismatch the junction between Si and Ge regions may produce unpaired valence band electrons or dangling bonds with a density of 10^{14} cm^{-2} [14]. Two consequences can be expected: bending of the energy bands at the interface and extensive recombination of minority carriers in the interface region where they can become trapped [21]. To overcome this, IBM designed "graded" $Si_{1-x}Ge_x$ HBTs where the Ge content is not constant, but instead increases (low concentration closer to the junction to high concentration deeper into the device) and thus contains a decreasing bandgap in the direction of electron flow

[18]. Incorporation of substitutional Ge into the crystal lattice of the silicon creates a compressive strain in the material due to the 4.2% lattice mismatch and as a result, reduces the bandgap of the material [18]. Figure 1.6 below shows an $Si/Si_{1-x}Ge_x$ NPN HBT, with n-type Si emitter and collector and p-type graded $Si_{1-x}Ge_x$ base region. The difference in bandgap allows the barrier for holes to inject backward from the base into the emitter, denoted in the figure as $\Delta\varphi_p$, to be made large, while the barrier for electrons to inject into the base $\Delta\varphi_n$ is low.
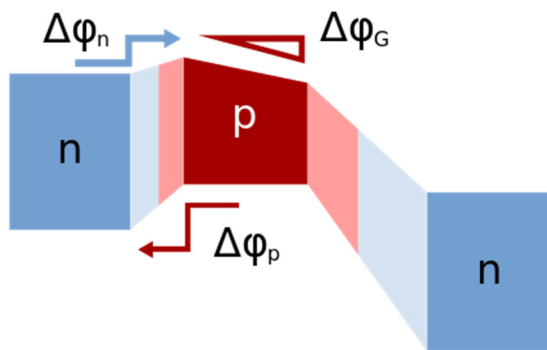
Figure 1.6: Bands in graded heterojunction NPN bipolar transistor. Barriers indicated for electrons to move from emitter to base and for holes to be injected backward from base to emitter; also, grading of bandgap in base assists electron transport in base region. Light colors indicate depleted regions ["Npn heterostructure bands" by Matthewbeckler licensed under CC BY SA 3.0].

Note that not only is the Ge content graded in the base, but the grading extends slightly into both emitter and collector to significantly reduce interface trap states. This barrier arrangement helps reduce minority carrier injection from the base when the emitter-base junction is under forward bias, and thus reduces base current and increases emitter injection efficiency. The improved injection of carriers into the base allows the base to have a higher doping level, resulting in lower resistance to access the base electrode [18]. The grading of composition in the base provides a

12

"built-in" field that assists electron transport across the base. That drift component of transport aids the normal diffusive transport, increasing the frequency response of the transistor by shortening the transit time across the base [18]. $Si/Si_{1-x}Ge_x$ HBT junction transistors integrated with complementary pairs of metal-oxide semiconductor transistors (BiCMOS) are the current state of the art [22], with industrial production level circuits featuring transit frequencies up to 320 GHz and maximum oscillation frequencies up to 400 GHz [22].

To make these BiCMOS circuits even faster, researchers are now investigating $Si_{1-x}Ge_x$ to replace the p-type Si channel in complimentary MOSFETs [23]. The improvements in performance $Si/Si_{1-x}Ge_x$ heterostructures can offer complimentary MOSFET technology is similar to what they offer to HBTs: at room temperature the carrier mobility can be increased by employing the band offset at the $Si/Si_{1-x}Ge_x$ heterojunction to spatially separate the mobile carriers from the ionized dopants on the one side, and from the interface with the oxide insulator on the other side [15]. With the arrival of these $Si_{1-x}Ge_x$ devices, researchers have had to confront many processing issues. To reach transistor specifications, the thickness and composition of the $Si_{1-x}Ge_x$ channel (or base) must be precisely controlled during the fabrication process [24]. Figure 1.7 describes the $Si_{1-x}Ge_x$ channel fabrication process. The process consists of (b) depositing an epitaxial $Si_{1-x}Ge_x$ layer on a silicon on insulator (SOI) substrate, (c) this layer is then oxidized at high temperature which leads to the migration of germanium atoms into the SOI substrate and finally (d) the top oxide layer is removed [24].
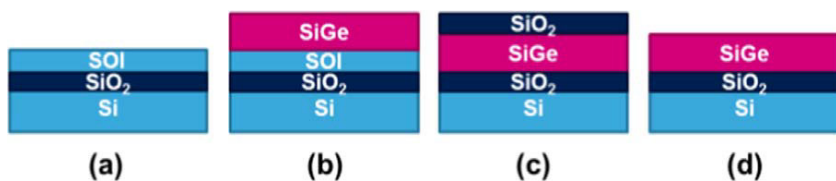
Figure 1.7: Illustration of the different processing steps for fully depleted $Si_{1-x}Ge_x$ channel formation on silicon-on-insulator substrates [24].

It follows then that for precise control over the composition of $Si_{1-x}Ge_x$ in the channel, the oxidation of $Si_{1-x}Ge_x$ must be well understood, as some of these channel layers can be very thin. To complicate things, depending on the processing step the preferential oxidation of silicon in $Si_{1-x}Ge_x$ is not always desired.

One of the biggest challenges in the fabrication of $Si_{1-x}Ge_x$ MOSFETs is the dielectric/$Si_{1-x}Ge_x$ interface control. The thermodynamic stability at the oxide/substrate interface becomes more serious in compound materials compared to homogeneous ones [25]. Attempts to thermally passivate alloys of $Si_{1-x}Ge_x$ using conventional thermal oxidation result in the selective oxidation of the Si in the alloy and resulting formation of a layer of Ge at the oxide/alloy interface [26]. These interfaces contain a relatively large number of defects which act as electron and hole traps. A device with a high trap density will affect the performance of the device because they steal the carriers from the channel thus lowering the conduction current. They can also trap and release mobile charge, leading to drain-current noise as well as reduced electrostatic control of the gate over the channel. Moreover, the carriers that are trapped will act as a charge scattering center [27]. CMOS process development require an intimate understanding of $Si_{1-x}Ge_x$ oxidation to accurately control the interface density in devices.

1.4   Silicon-Germanium Alloy Oxidation

Thanks to the important role Si/SiO_2 layers play in the manufacture of a large variety of transistors, the kinetics of this oxidation process are well understood. Established into a coherent model by Deal & Grove in 1965, silicon oxidation kinetics in the thick regime (neglecting

influences of the Si/SiO$_2$ interface) obey a linear-parabolic model of oxidation [28]. Their model successfully tracked experimental data for a wide range of temperatures (700-1300° C) and partial pressures (0.1-1.0 atm) for both molecular oxygen and water oxidants [28]. Linear growth could result if the rate limiting step were either the flux at the oxide-gas interface or that at the Si/SiO$_2$ interface. A parabolic growth law could result if the rate limiting process were either the diffusion of oxygen to the oxide-silicon interface or the diffusion of silicon to the oxide-gas interface [29]. Subsequent experiments provided additional information to help identify the diffusion of the oxidant as rate limiting in the parabolic regime and the reaction at the Si/SiO$_2$ interface as rate limiting in the linear regime.

The reaction at the Si/SiO$_2$ interface is controlled by the activation energy of the oxidation reaction. The activation energies 46.0 and 45.3 kcal/mole (2.0 and 1.96 eV) for dry and wet oxygen oxidation respectively are almost identical, indicating a similar surface control mechanism for the two oxidants (the energy required to break the Si-Si bond is 42.2 kcal/mol or 1.83 eV) [28]. The diffusion of the oxidants is controlled by the diffusivity activation energies and equilibrium oxidant solubility concentrations in the bulk oxide. Thus, the parabolic rate constant varies exponentially with temperature, corresponding to the available diffusivity activation energies of oxygen and water through SiO$_2$ (modeled as fused silica) [28]. Importantly, Deal & Grove identified that while the diffusivity of water in fused silica is lower than the diffusivity of molecular oxygen, the equilibrium solubility concentration of water is three orders of magnitude larger resulting in a higher overall reaction rate in the wet case [28]. However, in the early stages of oxidation when the oxide is very thin (less than 250 Å) dry oxidation is faster [28], so fast it cannot accurately be described by their own linear-parabolic

model. Figure 1.8 below shows how wet-oxidation fits well into the linear-parabolic model and extrapolates back to zero oxide at t = 0, but dry oxidation does not.
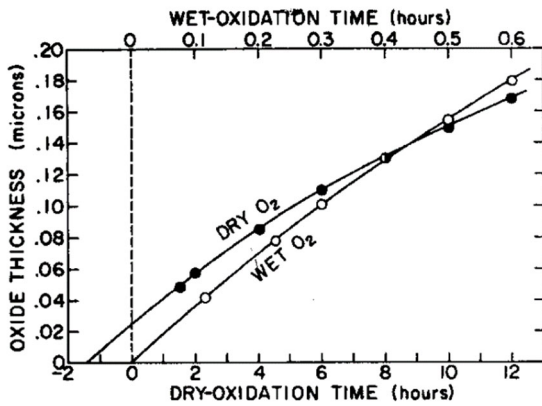
Figure 1.8: Comparison of initial oxide growth on silicon at 920 °C for oxidation in wet (95 °C H₂O) and dry-oxygen ambients. An offset of about 200 Å in the thickness data exists when data is extrapolated to t = 0 [28].

In the 20 years following Deal & Grove, various models were proposed to explain silicon dry oxidation rate enhancement in the thin regime. Tiller [30] suggested that the oxygen molecules were ionized at the outer surface via charge transfer between bulk Si and the thin SiO_2, leading to an electric field assist to diffusion. Revesz & Evans [31] suggested that microchannels in thin film oxides offered pathways for faster diffusion. Blanc [32] and Hu [33] proposed that both molecular and atomic oxygen took part in the reaction. This analysis will focus on the works of Massoud et al. [29] and Wong & Cheng [34], who using experimental results and previous models developed a comprehensive picture of dry oxidation in the thin regime.

Massoud et al. proposed that a higher oxidation rate than predicted by the Deal-Grove model is the result of additional parallel process fluxes. If these fluxes occurred in series they

16

would reduce the overall reaction rate if they are the rate limiting process, or the growth rate would remain unchanged if they are not [29]. The three main fluxes described by Deal-Grove in the thick regime are the flux of the oxidant from the gas to the vicinity of the outer silicon surface, F_1, the flux of the oxidant across the oxide layer, F_2, and the flux corresponding to the oxidation reaction at the Si/SiO$_2$ interface, F_3 [28]. The first two parallel fluxes described by Massoud et al. for the thin regime are the flux of oxidant species absorption at the outer surface of the oxide caused by possible field effects on the oxygen species or by the porous structure of SiO$_2$ at the onset of oxidation, ΔF_1, and field aided diffusion of ionized oxygen species or the transport of molecular and atomic oxygen in the neutral and ionized states across the oxide, ΔF_2. Reactions to form oxide that include molecular or atomic oxygen reacting at silicon-silicon bonds, partially bonded surface silicon atoms, or silicon vacancies account for additional flux ΔF_3. Finally, Flux F_4 possibly represents transport of oxygen species along microchannels in the oxide to reach the interface and react with the substrate, so occurs in parallel with the entire main three-flux process. Figure 1.9 below shows a schematic with all parallel and series fluxes included in the Massoud et al. model, in addition to a figure showing experimental data for silicon oxidation in the thin regime showing significant departure from the Deal-Grove linear-parabolic model.
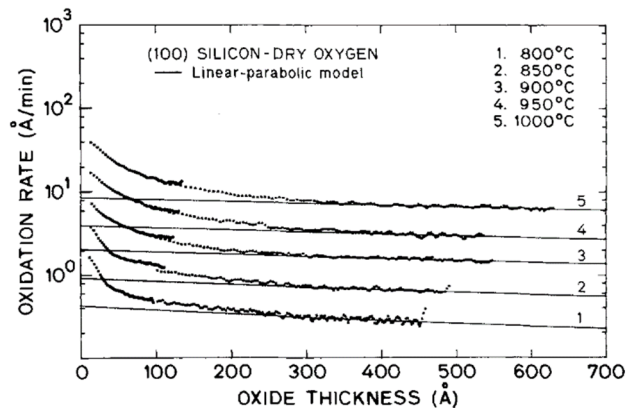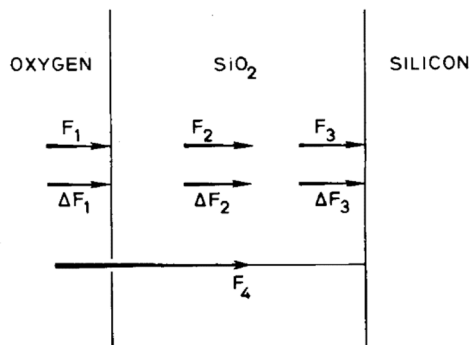
Figure 1.9: (a) Modeling oxygen-rate enhancement in the thin regime by adding additional processes in parallel to those described by the Deal-Grove linear-parabolic model, and (b) experimental data for silicon (100) oxidation in dry oxygen from 800-1000 °C showing departure from the linear-parabolic model in the thin regime at all temperatures [29].

Wong & Cheng [34], building upon the works of Massoud et al. [29], constructed a mathematical model of these hypothesized extra processes in the thin regime. They proposed that electrically neutral oxygen species are transported through the oxide via interstitial sites and charged species through the oxide network [34]. The transport of the charged species is assisted by an internal electric field created by potential difference between acceptor levels with trapped electrons formed due to dissociated oxygen species at the outer oxide surface and the energy level of silicon-oxide interface states [34]. In addition, they determined that the contribution of other proposed excess mechanisms such as stress relaxation in the oxide and microchannels are insignificant in comparison [34].

These models developed for oxidation of silicon in dry-oxygen in the thin oxide regime served as an important comparison point for research into the oxidation of silicon-germanium alloys. In lockstep with research into how silicon-germanium alloys can improve the carrier mobility in transistors, fundamental research into the oxidation of silicon-germanium alloy for composition controlled $Si_{1-x}Ge_x$ channels, $Si_{1-x}Ge_x$ based MOSFETs, and high quality $Si_{1-x}Ge_x$ surface passivation began to appear in the late 1980s to 1990s. As mentioned in the introduction to silicon-germanium heterostructure transistors, the thickness and composition of $Si_{1-x}G e_x$ layers must be precisely controlled during the fabrication process. This is also true for the oxide layers themselves, as they must be incredibly thin and to the extent possible should minimize

defect formation. Researchers began to look closely at thin regime oxidation to observe how the alloy would behave when compared the rate enhanced oxidation of silicon. It became clear early on that the oxidation of the alloy in the thin regime is distinctly different from the oxidation of its pure components.

Driving the difference in the oxidation behavior of the alloy is the much lower formation energy of SiO_2 than GeO_2 (E_{SiO_2} = -8.2 eV and E_{GeO_2} = -4.7 eV) which highly favors the formation of SiO_2 over GeO_2 [35]. As the alloy oxidizes a gradient is created in the Si and Ge mole fractions which causes inter-diffusion of Si and Ge so that a net flux of Si atoms is generated towards the oxidizing interface [36]. In parallel, the Ge atoms pile up at this new $Si_{1-x}Ge_x$/SiO_2 interface forming a germanium-rich layer (GRL) without loss of Ge until the silicon is fully oxidized [35]. A simple schematic of this oxidation process can be found in Figure 1.10 below.
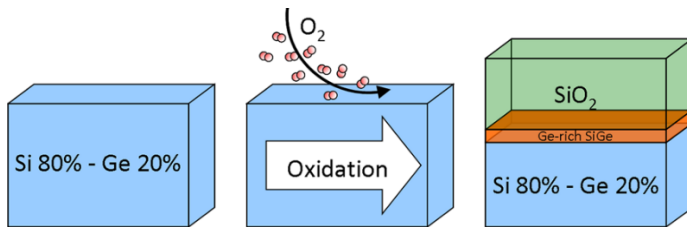
Figure 1.10: Oxidation of $Si_{1-x}Ge_x$ and formation of a Ge-rich layer by condensation of germanium at the interface [35]

Thermodynamics would dictate that since $Si_{1-x}Ge_x$ is a solid solution, a minimum of energy (elastic and free energy) should occur at a germanium content of x = 0.5. While this means GRLs should stabilize at a composition of $Si_{0.5}Ge_{0.5}$, formation is metastable and controlled by the kinetic barrier to interdiffusion of Ge [35]. Ge self-diffusion activation energies

in $Si_{1-x}Ge_x$ alloy have been reported to decrease with increasing germanium content, with the activation energy for x = 0.50 already very close to the known value for pure Ge [19]. Ab initio studies indicate that vacancies with four or three Ge nearest neighbors have the lowest formation energies, encouraging atoms to diffuse in pure-Ge like paths. As the Ge concentration decreases, nearest neighbor sites are more likely to be Si which complicates the diffusion path. Since Si and Ge are expected to diffuse by similar mechanisms [37], the presence of a high germanium content GRL (x=0.50) significantly reduces the activation energy for both Si and Ge inter-diffusion. At 750 °C, the diffusion coefficient of Ge in $Si_{0.5}Ge_{0.5}$ is 5 orders of magnitude higher than in $Si_{0.8}Ge_{0.2}$ [35]. The result being at low temperatures ($\leq$ 900 °C) the minimization of free energy of the whole system is prevented because of the high diffusion barrier of Ge in $Si_{0.8}Ge_{0.2}$, leading to GRL formation. At high temperatures Ge from the GRL diffuses toward the low concentration and homogenizes the $Si_{1-x}Ge_x$ layer concentration in the whole system [35].

While silicon oxidation is more favorable than germanium oxidation, stable germanium oxides can exist. This happens when the flux of the diffused silicon is insufficient to react with the arriving oxidant flux [36]. There are several kinetic factors affecting the silicon flux diffusing towards the oxidizing interface including temperature, pressure, and germanium concentration in the alloy. It has been observed that low temperature, high pressure, or high germanium concentration in the alloy can result in the silicon flux being insufficient to react with the arriving oxidant molecules and thus lead to the oxidation of germanium. If the flux of silicon is small enough (compared to oxidant flux), germanium is oxidized at a nearly equal rate to the rate of oxidation of silicon. The percent of Ge to Si in the oxide will be close to that found in the original $Si_{1-x}Ge_x$ alloy [36], and no GRL forms. In summary, for the fast regime (thin oxides <250 Å) the rate limiting step for $Si_{1-x}Ge_x$ oxidation is the same as for pure Si: reaction of the

oxidant with Si or Ge at the oxide/alloy interface. However, for $Si_{1-x}Ge_x$ this reaction is itself governed by the interdiffusion of silicon to the oxidation front. If diffusion is sufficient, a pure SiO_2 oxide forms. If diffusion is too slow, a mixed oxide forms with an increasing germanium content the slower the diffusion of Si. The expected oxides that will form on $Si_{1-x}Ge_x$ based on relative Si and O_2 fluxes and temperature can be found in Figure 1.11 below.
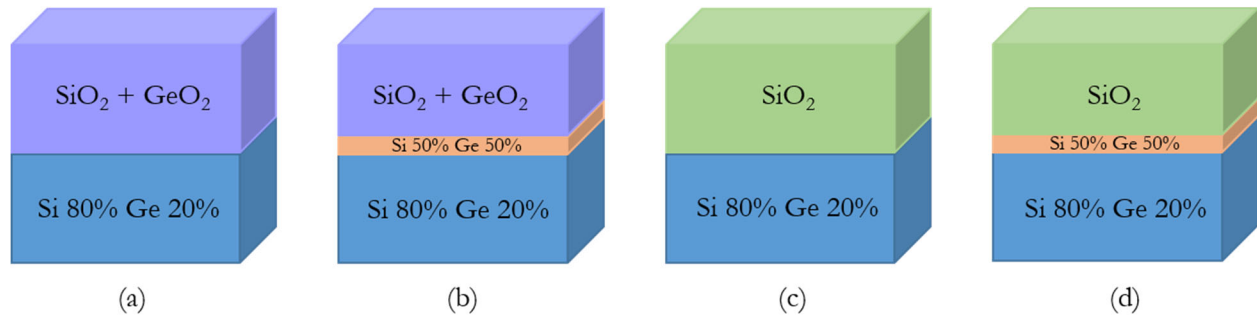
Figure 1.11: Oxidation of silicon germanium alloy when (a) Si flux is small compared to O_2 flux resulting in equal oxidation of Si and Ge, (b) Si flux is small compared to O_2 flux still slightly preferring oxidation of Si, (c) Si flux is large compared to O_2 flux at high temperature ($\geq 900°C$), and (d) Si flux is large compared to O_2 flux at low temperature ($\leq 900°C$).

In Figure 1.11 (a) & (b), the Si flux to the interface is small compared to O_2 flux resulting in the oxidation of both Si and Ge despite the thermodynamic preference for SiO_2 formation. If the oxidation rates are the same, no GRL will form. If they are different, a thin GRL is expected to form. In Figure 1.11 (c) & (d), the Si flux to the interface is large compared to O_2 flux resulting in preferential oxidation of Si. The stability of the GRL is temperature dependent, with the Ge content homogenizing at high temperatures as seen in (c). Note that due to a proportion of Ge being oxidized in (b), GRL growth is expected to be much slower than in (d).

Without a catalytic effect, this model would predict the oxide growth rate to always be somewhere between that for pure Si and pure Ge. However, it is generally agreed that Ge acts as a catalyst for the formation of SiO_2 in wet oxidation [38] and for dry oxidation either slightly enhances rate [39], or has no effect on rate [38]. Rabie et al. [36] summarized the possible contributors to the catalytic effect: (1) the weakness of the Si-Ge bond compared to the Si-Si bond causing more Si atoms to participate in the oxidation reaction, (2) the reaction of Ge with the oxidant forming GeO_2 and subsequent Si replacement for Ge in GeO_2 forming SiO_2 which is actually faster than direct oxidation of Si [40], and point defects. They concluded that since the first two occur in both wet and dry oxidation, the most important factor in explaining rate enhancement in wet oxidation is point defects. LeGoues et al. [40] determined that Ge affects the point defect concentration near the oxidizing surface, changing the mechanism from excess Si interstitial production, which occurs for pure Si oxidation, to excess vacancy production. They hypothesize this suppression of interstitial Si injection into the bulk favors diffusion of Si toward the oxidation interface through excess vacancies in the GRL. This causes more Si atoms to participate in the oxidation reaction, thus enhancing the oxidation rate. For dry thermal oxidation which is much slower than wet oxidation, it is hypothesized the interstitials have enough time to diffuse into the bulk [40]. In this case the rate enhancing effects of Ge are suppressed and the oxidation rate of $Si_{1-x}Ge_x$ is similar to Si.

Research by Song et al. [25] predicts that for dry oxidation, the replacement reaction, introduced above as a possible contributor to the catalytic effect, is not favored over direct Si reaction with the oxidant until some critical low pressure at fixed temperature. The consequence being that if a catalytic effect is observed at pressures above the critical pressure, the effect is likely due to breaking of substrate Si-Ge bonds and/or point defects. Tetelin et al. [41] observed

no $Si_{1-x}Ge_x$ oxidation rate enhancement over Si in molecular oxygen ambient, but a significantly enhanced $Si_{1-x}Ge_x$ rate in atomic oxygen. They attributed breaking of substrate bonds as limiting in atomic oxygen, and dissociation of oxygen as limiting in molecular oxygen [41]. However, Spadafora et al. [39] determined that the dry molecular oxygen $Si_{1-x}Ge_x$ oxidation rate increases approximately linearly with Ge concentration [39] due to the lower binding energy of Si-Ge compared to Si-Si [42]. They propose a unified view of dry and wet oxidation where the difference in Si-Si and Si-Ge binding energies and the role of point defects generated during oxidation can explain rate differences between Si and $Si_{1-x}Ge_x$ under all conditions [39].

1.5   Surface Morphology and Non-Abrupt Oxide Interface

In addition to the need for precise control over the thickness and composition of layers within a heterostructure transistor, the abruptness of the interface between oxide and bulk alloy must also be tightly controlled. State-of-the-art device technology demands that MOSFET gate-oxide film thickness be as thin as 1 nm where the chemical abruptness of the interface affects the performance of the device [43]. Researchers needed a way to observe the atomic arrangement and the nature of the chemical bonds at the surface of synthesized semiconducting alloys. Again, decades of studies on the Si/SiO_2 interface served as a launching point for similar studies into $Si_{1-x}Ge_x$ alloy.

Discussion of suboxide states warrants a brief discussion of crystal morphology. There is only limited interest in bulk $Si_{1-x}Ge_x$ alloys, as the lattice mismatch strain is relaxed as the layer grows. Lattice strain alters the valence and conduction bands by shifting them in energy, distorting them, and removing degeneracy all in a customizable way [13]. Of particular interest is biaxially strained thin films in the (001) plane, which corresponds to pseudomorphic growth on a

(001)-oriented substrate [13]. Accordingly, this analysis will focus on Si, Ge, and $Si_{1-x}Ge_x$

crystals cleaved along the (001) plane. Silicon has four bonds in a tetrahedral arrangement and

forms the diamond lattice structure. In the bulk of a silicon crystal viewed from the (001) plane,

two of these bonds orient to the level below and two orient to the next level above [3]. Figure

1.12 below shows three successive planes in the bulk crystal structure (dots of different shades of

red represent atoms on different planes). Cleaving a crystal along a (001) plane leaves the surface

atoms with only two bonds intact and the other two as dangling bonds as seen in Figure 1.12(a).

The surface atoms can then orient toward neighboring atoms to form pairs, known as dimers

forming a (1x2) surface as seen in Figure 1.12(b).

(a)   (b)
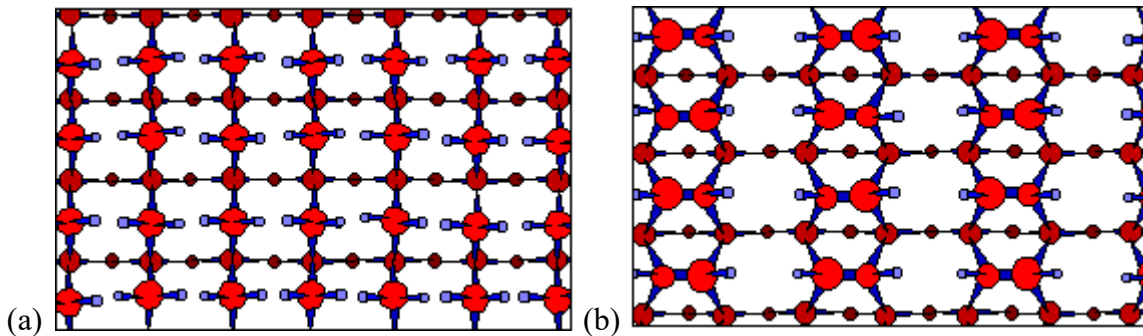
Figure 1.12: Bulk terminated and reconstructed Si (001)-2×1 surface [Univ. of Minnesota, Dept.

of Phys &Astronomy].

This leaves the reconstructed surface with only two dangling bonds per dimer, which is

thermodynamically more favorable. The surface will remain in the bulk terminated construction

if properly stabilized, but will often reconstruct in-situ after ion bombardment and thermal

annealing [44]. The number of dangling bonds at crystal surface is orientation dependent, so

upon exposure to an oxidant it is expected that the nature of the chemical bonds at the surface

will be orientation dependent as well.

It is generally agreed upon that the Si/SiO_2 interface is "quasiabrupt" with a SiO_x

transition layer which contains Si atoms in intermediate oxidation states [45]. However, early

research on this topic had technological limitations where the necessary surface sensitivity was

not available to confidently characterize oxidation at the Si/SiO_2 interface. This led to

contradicting conclusions on the thickness of the transition layer, abundance of suboxide states,

and depth distribution of the same. The atomic arrangement at the interface and nature of the

chemical bonds is difficult to observe mainly due to the fact that it is incredibly thin and as the

oxidation of the surface proceeds, the interface is slowly buried under the oxide. To probe the

chemical structure of the interface it is necessary to use a technique which is sensitive to the

local environment such as high resolution core level photoelectron spectroscopy. Using high

resolution X-ray photoelectron spectroscopy (XPS) and numerical techniques, Grunthaner et al.

[46] first hypothesized that the intermediate oxidation states at the Si/SiO_2 interface were Si^{1+}

(Si_2O), Si^{2+} (SiO), and Si^{3+} (Si_2O_3) and offered a relative abundance ratio of 2:3:2 for the first

through third oxidation states respectively [46]. Hollinger & Himpsel [45] confirmed the

presence of these oxidation states using synchrotron radiation, a technology allowing tunable X-

ray energy to vastly improve the surface sensitivity compared to the conventional XPS used by

Grunthaner. They were able to identify chemical shifts of 1.0, 1.8, and 2.7 eV (to be discussed

further in Chapter 2) assigned to silicon 1+, 2+, and 3+ oxidation states. Moreover, they

concluded that Si^{1+}, Si^{2+}, and Si^{3+} units are almost equally distributed (0.4:0.3:0.3) with no strong

differences between Si(111)-SiO_2 and Si(100)-SiO_2 interfaces or thickness of suboxide film in

the 5-11 Å range [45]. Later research by Grunthaner at al. [44] built upon these earlier works,

using data reduction to fit oxide XPS spectral data with symmetrical Gaussian curves (to be

discussed further in Chapter 2) to confirm broadening of suboxide peaks with increasing number

of Si-O bonds [44]. Additionally, due to structural differences between near-interface SiO_2 and bulk SiO_2 they concluded that this oxide peak will shift in binding energy (chemical shift from 3.8 eV to 4.4 eV for near-interface to bulk, respectively) and width (more disordered near-interface oxide will be broader) [44]. Using these methods of data reduction, they were further able to conclude that the Si^{1+} and Si^{2+} suboxide states are localized within 6-10 Å of the interface, while Si^{3+} state extends ~30 Å into the bulk oxide [44]. Moreover, the spatial distribution of Si^{1+} and Si^{2+} are strongly dependent on the crystal surface plane, with Si^{2+} dominating on (100) substrates and Si^{1+} dominating on (111) substrates [44]. It should be noted that their Si(100) substrates were not sputtered or thermally annealed, so are not expected to be the (2x1) reconstructed surface.

Himpsel et al. [47] conducted a quantitative study of the Si/SiO_2 interface also using synchrotron radiation photoemission spectroscopy. They found the chemical shifts of Si oxides to be 0.95, 1.75, 2.48, and 3.9 eV for the $Si^{1+,}$ Si^{2+}, Si^{3+}, and Si^{4+} oxidation states respectively. They explained the shift of the Si^{4+} oxidation state to be closer to the substrate peak for oxides less than 5 Å due to smaller valence-band offset and extra screening by the Si substrate [47]. Additionally they found the Si^{3+} and Si^{2+} states to move further from the substrate peak for films thinner than 5 Å due to absence of dielectric screening by the SiO_2 overlayer [47]. Figure 1.13 below shows the core level emission spectra Himpsel et al. obtained with synchrotron radiation at hv = 130 eV for ultrathin oxide layers on Si(100) and Si(111). The Si(111) substrate has less Si^{2+} and more Si^{1+} than the Si(100) substrate.
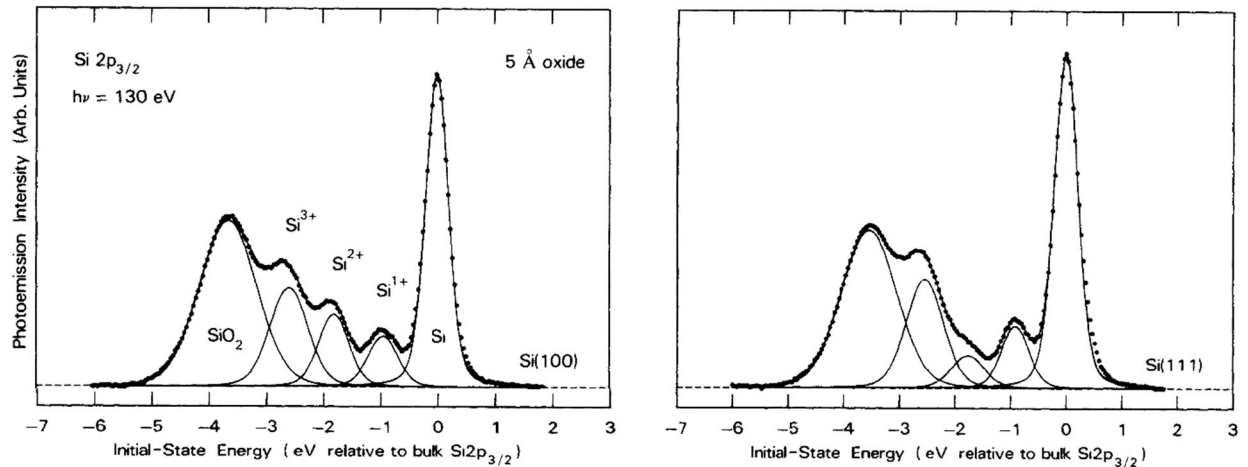
Figure 1.13: Core level emission spectra obtained with synchrotron radiation at $h\nu = 130$ eV of ultrathin oxide layers on Si(100) and Si(111) [47].

The existence of all three oxidation states on Si(100) clearly indicates deviations from an ideal, atomically abrupt interface. They posit that the density of intermediate oxidation states is correlated to the density of dangling bonds at the surface, thus defects at the surface could cause variation between two surfaces [47]. Compiling literature data on the XPS intensity ratios between bulk oxide and substrate, experimentally determined cross-sections, and photoelectron mean free paths (all to be discussed further in Chapter 2). Himpsel et al. also provided a detailed analysis on the density and distribution of intermediate oxidation states. They found that variations in pressure (10^{-5} to 20 Torr) and temperature (700 to 1100 °C) do not affect the distribution of oxidation states significantly for oxides up to 30 Å thick [47]. Additionally, they found the transition layer to be about two Si atomic layers thick, which corresponds to 3 Å of pure Si or to 6 Å of SiO_2, in agreement with field ion microprobe experiments giving the range as 3-5 Å [47].

Oh et al. [43] extended synchrotron photoemission studies to vary photoemission angle, thereby changing the depth from which photoelectrons are detected from the sample (discussed further in Chapter 2). This technique is called angle-resolved X-ray photoelectron spectroscopy (ARXPS). They plotted intensity ratios of the Si 2p Si^{1+} to Si^{4+} components to the total intensity of the Si-substrate related components as a function of the polar emission angle. The results can be found in Figure 1.14.
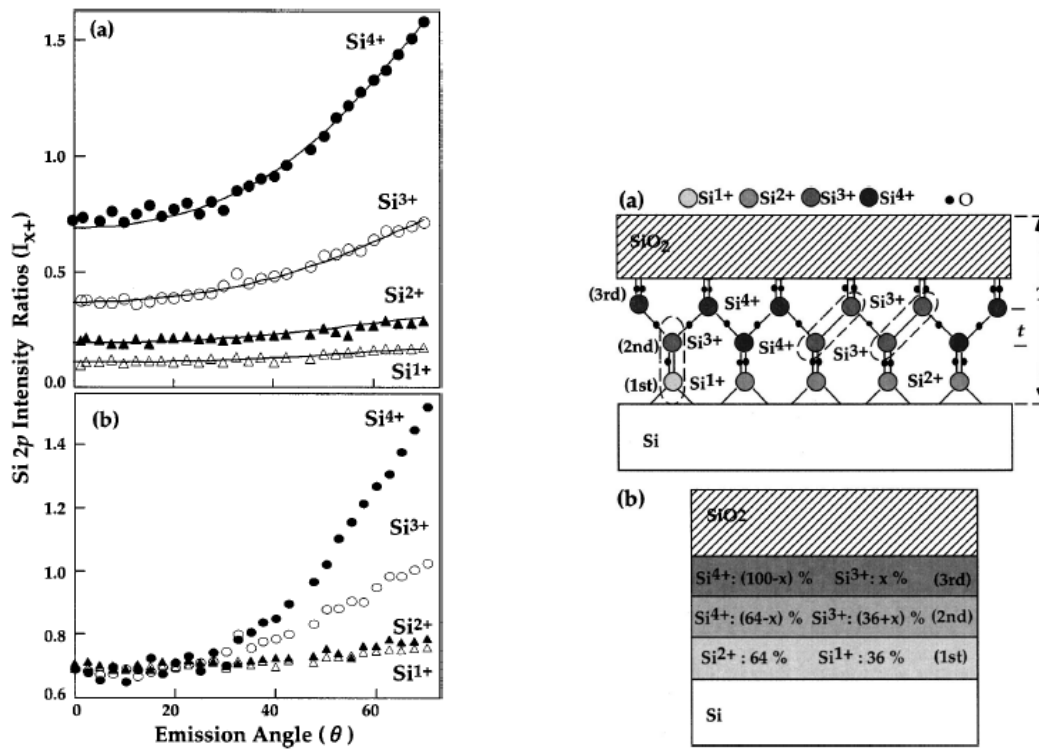
Figure 1.14: (left, a) Intensity ratios of the Si 2p Si^{1+} – Si^{4+} components to the Si^0 substrate as a function of the polar emission angle. The symbols represent experimental data, curves based on an interfacial structure model. (left, b) The same intensity ratios as in (a), but renormalized by the intensity at normal emission. (right, a) Side view of the chemically non-abrupt interface model for Si(100)/SiO₂. Different suboxide species are depicted with different symbols, and the transition layers at the interface are composed of three chemically different layers. (right, b)

Schematic illustration of the chemical composition of the transition layers based on the model shown in (a).

From the data presented in Figure 1.14, Oh et al. [43] concluded that while the intensity ratio of Si^{1+} and Si^{2+} is constant at 1:1.8 meaning consistent but different population, their dependence on emission angle is identical within experimental error suggesting these species have the same depth distribution most probably within the first few interfacial layers [43]. The intensity ratio of Si^{3+} shows a greater rate of increase, suggesting the Si^{3+} species is distributed over a wider region from the interface boundary toward the surface [43]. Oh et al. also concluded that the Si^{4+} component shows the steepest dependence on emission angle as the SiO_2 layers are on top of the suboxide layers, which makes the Si^{4+} component stronger in the more surface sensitive condition of larger emission angle [43]. From this ARXPS data, Oh et al. constructed the graded interface model as seen on the right side of Figure 1.14. The first layer of the interface should consist of only Si^{1+} and Si^{2+}, and taking into account the intensity ratio of 1:1.8, they concluded the relative abundance is 36% Si^{1+} to 64% Si^{2+} [43]. To account for the difference of the depth distribution between Si^{3+} and the other suboxides, the Si^{3+} species is included in the second and third layers from the interface. The parameter x in Figure 1.14(b) is then treated as a fitting parameter in simulating the emission angle dependence of the Si^{3+} state.

Similar studies have been performed on the oxidation of Ge(001). In a manner similar to the Si 2p peak observed during oxidation of Si(001), when a germanium sample is annealed in an oxidant ambient a high binding energy "shoulder" develops on the Ge 3d spectra which progressively shifts toward higher binding energy as oxidation progresses. Schmeisser et al. [48] determined that for both Ge(111) and Ge(001) four discrete chemically shifted core levels are

observed that yield a chemical shift of 0.85 eV per Ge-O bond. Upon initial exposure primarily

the Ge^{1+}, Ge^{2+}, and Ge^{3+} oxidation states are present [48]; drawing an analogy to silicon these are

germanium suboxides present at the interface. Molle et al. [49] exposed Ge(001) samples to an

atomic O beam at a partial pressure of $5x10^{-5}$mbar for a fixed exposure time of 20 min. They

then annealed these samples to a range of temperatures and observed changes in the Ge 3d

spectra. They curve fit the Ge 3d spectra to identify the chemical shift of the four expected

oxidation states. The GeO_2 (+4) and GeO (+2) components were identified by chemical shifts at

3.5 eV and 1.7 eV, respectively [49], in good agreement with the molecular oxygen oxidation

experiments performed by Schemisser. Two additional suboxide peaks were fit intermediate

between the previous oxide components, with a chemical shifts of 0.70 eV ascribed to Ge_2O (+1)

and 2.81 eV to Ge_2O_3 (+3), to interpolate the shape profile of the spectra [49]. These trends are

very similar to the oxidation behavior of silicon. However, the two diverge at annealing

temperatures of and above 300 °C. At this temperature, Molle et al. [49] observed that

chemisorption of oxygen is noted to provoke a core level shift of the bulk Ge peak compared to

the Ge 3d peak of the as-received sample. This shift is attributed to band bending due to the

higher electronegativity of the oxygen atoms. They also demonstrated a starkly higher rate of

formation of GeO_2 (+4) at 300°C [49]. At still higher temperatures of around 400 °C, they

observed a decrease in intensity of the GeO_2 peak and a shift to lower binding energy [49]. They

hypothesized that this is the result of chemical transformation of GeO_2 to GeO by thermal

decomposition [50]. The oxide continues to decompose and then desorb near 420 °C [50], in

contrast to silicon which will continue to form SiO_2 to much higher temperatures [50]. Figure

1.15 shows the XPS spectra of the Ge 3d peak after a 20 min long atomic oxygen exposure at

substrate temperatures T = RT, 200, 300, and 400 °C. The oxide species GeO_x and GeO_2 and the

Ge bulk peak marked as Ge B are shown.
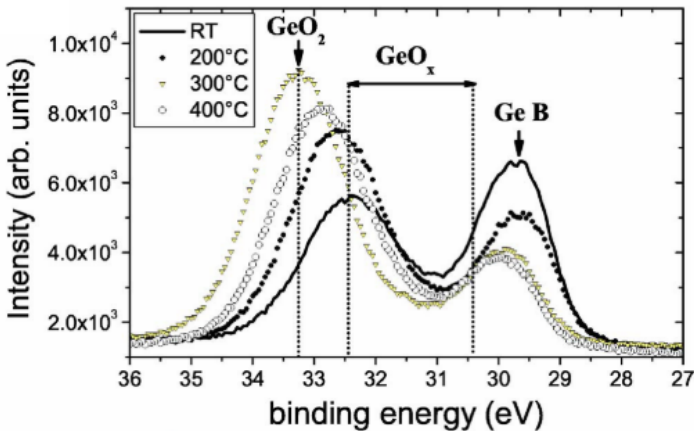
Figure 1.15: XPS spectra of the Ge 3d peak after a 20 min long atomic oxygen exposure at substrate temperatures T = RT, 200, 300, and 400 °C. The oxide species GeO_x and GeO_2 and the Ge bulk peak marked as Ge B are shown [49].

Note the shift in the core elemental peak, Ge B, due to band bending at 300 °C and decrease in intensity of the GeO_2 peak at 400 °C.

Many studies on thin regime oxidation of $Si_{1-x}Ge_x$ have used chemical state resolved XPS. In the literature surveyed in this analysis, Si 2p and Ge 3d curve fitting procedures have been extrapolated from studies on pure Si and Ge. In their foundational study on oxidation of $Si_{1-x}Ge_x$, LeGoues et al. [40] fit the Si 2p core level using the procedure from Hollinger & Himpsel [45] and the Ge 3d core level using chemical shifts from Schmeisser et al. [48]. Few other papers include complete details on alloy fitting procedures. Madsen et al. [51] fit the Si 2p core level using a procedure from Lu et al. [52], a synchrotron study on the SiO_2/Si interface, but do not provide a detailed Ge 3d fit. Kilpatrick et al. [53], [54] include curve fits for both Si 2p and Ge

3d, but do not include details on chemical shifts of the suboxides. Similarly, Bera et al. [55] and

Agarwal et al. [56] focus on the well documented positions of elemental and stoichiometric

oxide peaks likely due to uncertainty regarding the chemical shift of suboxides. Common to all

$Si_{1-x}Ge_x$ studies is the use of symmetric Gaussian peaks to fit oxide peaks, and Gaussian-

Lorentzian symmetric convolutions to fit elemental peaks (explained in more detail in Chapter

2).

1.6   References

[1]   H. C. Torrey and C. A. Whitmer, "Crystal Rectifiers," in *MIT Radiation Lab Series*, First., S. A. Goudsmit, L. B. Linford, J. L. Lawson, and A. M. Stone, Eds. New York: McGraw-Hill Book Company, 1948.

[2]   C. Kittel, *Introduction to Solid State Physics*, 8th ed. Hoboken, New Jersey, New Jersey: John Wiley & Sons, Inc., 2005.

[3]   W. D. J. Callister, *Materials Science and Engineering: An Introduction*, 7th ed. New York, NY, NY: John Wiley & Sons, Inc., 2007.

[4]   W. Shockley, "Circuit element utilizing semiconductive material," US2569347A, 1951.

[5]   P. Valizadeh, *Field effect transistors : A comprehensive overview : From basic concepts to novel technologies*. Hoboken, New Jersey: John Wiley & Sons, Inc., 2016.

[6]   Z. Huda and R. Bulpett, *Materials science and design for engineers*. Enfield, New Hampshire: Trans Tech Publications, 2012.

[7]   T. F. Schubert and E. M. Kim, *Fundamentals of Electronics*. 2015.

[8]   R. Lewis, *Solid-State Devices and Applications*. Kent: Elsevier Science & Technology, 2013.

[9]   C. H. Chenming, *Modern Semiconductor Devices for Integrated Circuits*, 1st ed. Pearson, 2009.

[10]   H. Kroemer, "Theory of a Wide-Gap Emitter for Transistors," *Proc. IRE*, vol. 45, no. 11, pp. 1535–1537, 1957.

[11]   H. Kroemer, "Heterostructure Bipolar Transistors and Integrated Circuits," *Proc. IEEE*, vol. 70, no. 1, pp. 13–25, 1982.

[12]   S. Brojdo, T. J. Riley, and G. T. Wright, "The heterojunction transistor and the space-charge-limited triode," *Br. J. Appl. Phys.*, vol. 16, no. 2, pp. 133–136, 1965.

[13] D. K. Jadus and D. L. Feucht, "The Realization of a GaAs-Ge Wide Band Gap Emitter Transistor," *IEEE Trans. Electron Devices*, vol. 16, no. 1, pp. 102–107, 1969.

[14] A. G. Milnes, *Heterojunctions and metal-semiconductor junctions*. New York: Academic Press, 2012.

[15] F. Schäffler, "High-mobility Si and Ge structures," *Semicond. Sci. Technol.*, vol. 12, no. 12, pp. 1515–1549, 1999.

[16] G. L. Patton, S. S. Iyer, S. L. Delage, S. Tiwari, and J. M. C. Stork, "Silicon-germanium base heterojunction bipolar transistors by molecular beam epitaxy," *IEEE Electron Device Lett.*, vol. 9, no. 4, pp. 165–167, Apr. 1988.

[17] G. L. Patton, J. H. Comfort, B. S. Meyerson, and F. Emmanuel, "SiGe-Base Heterojunction Bipolar Transistors," *IEEE Electron Device Lett.*, vol. 1, no. 4, pp. 171–173, 1990.

[18] J. S. Dunn *et al.*, "Foundation of rf CMOS and SiGe BiCMOS technologies," *IBM J. Res. Dev.*, vol. 47, no. 2.3, pp. 101–138, 2003.

[19] P. Venezuela, G. M. Dalpian, A. J. R. da Silva, and A. Fazzio, "Vacancy-mediated diffusion in disordered alloys: Ge self-diffusion in $Si_{1-x}Ge_x$," *Phys. Rev. B*, vol. 65, no. 19, pp. 193306–193309, May 2002.

[20] A. Strohm, T. Voss, W. Frank, J. Räisänen, and M. Dietrich, "Self-diffusion of ^{71}Ge in Si-Ge," *Phys. B Condens. Matter*, vol. 308–310, pp. 542–545, 2001.

[21] W. G. Oldham and A. G. Milnes, "Interface states in abrupt semiconductor heterojunctions," *Solid. State. Electron.*, vol. 7, no. 2, pp. 153–165, Feb. 1964.

[22] H. Rücker and B. Heinemann, "High-performance SiGe HBTs for next generation BiCMOS technology," 2018.

[23] F. Rozé *et al.*, "Oxidation kinetics of Si and SiGe by dry rapid thermal oxidation, in-situ steam generation oxidation and dry furnace oxidation," *J. Appl. Phys.*, vol. 121, no. 24, 2017.

[24] L. Fauquier *et al.*, "Benefits of XPS nanocharacterization for process development and industrial control of thin SiGe channel layers in advanced CMOS technologies," *Mater. Sci. Semicond. Process.*, vol. 70, pp. 105–110, Nov. 2017.

[25] W. Song and A. Toriumi, "Study of SiGe oxidation kinetics for preferential SiO_2 formation under a low O_2 pressure condition," *J. Appl. Phys.*, vol. 122, no. 18, pp. 185301–185307, Nov. 2017.

[26] D. C. Paine, C. Caragianis, and a. F. Schwartzman, "Oxidation of $Si_{1-x}Ge_x$ alloys at atmospheric and elevated pressure," *J. Appl. Phys.*, vol. 70, no. 9, pp. 5076–5084, 1991.

[27] B. K. Boksteen, J. Schmitz, and R. J. E. Hueting, "Interface Trap Density Estimation in FinFETs Using the gm/ID Method in the Subthreshold Regime," *IEEE Trans. Electron Devices*, vol. 63, no. 5, pp. 1814–1820, 2016.

[28] B. E. Deal and A. S. Grove, "General relationship for the thermal oxidation of silicon," *J. Appl. Phys.*, vol. 36, no. 12, pp. 3770–3778, 1965.

[29] H. Z. Massoud, "Thermal Oxidation of Silicon in Dry Oxygen Growth-Rate Enhancement in the Thin Regime," *J. Electrochem. Soc.*, vol. 132, no. 11, pp. 2685–2693, 1985.

[30] W. A. Tiller, "On the Kinetics of the Thermal Oxidation of Silicon," *J. Electrochem. Soc.*, vol. 127, no. 3, p. 619, 1980.

[31] A. G. Revesz and R. J. Evans, "Kinetics and mechanism of thermal oxidation of silicon with special emphasis on impurity effects," *J. Phys. Chem. Solids*, vol. 30, no. 3, pp. 551–564, Mar. 1969.

[32] J. Blanc, "A revised model for the oxidation of Si by oxygen," *Appl. Phys. Lett.*, vol. 33, no. 5, pp. 424–426, 1978.

[33] S. M. Hu, "New oxide growth law and the thermal oxidation of silicon," *Appl. Phys. Lett.*, vol. 42, no. 10, pp. 872–874, 1983.

[34] H. Wong and Y. C. Cheng, "A new growth model of thin silicon oxide in dry oxygen," *J. Appl. Phys.*, vol. 64, no. 2, pp. 893–897, 1988.

[35] T. David *et al.*, "Kinetics and Energetics of Ge Condensation in SiGe Oxidation," *J. Phys. Chem. C*, vol. 119, no. 43, pp. 24606–24613, 2015.

[36] M. A. Rabie, Y. M. Haddara, and J. Carette, "A kinetic model for the oxidation of silicon germanium alloys," *J. Appl. Phys.*, vol. 98, no. 7, pp. 074904–074913, Oct. 2005.

[37] P. Laitinen *et al.*, "Self-Diffusion of ^{31}Si and ^{71}Ge in Relaxed $Si_{0.20}Ge_{0.80}$ Layers," *Phys. Rev. Lett.*, vol. 89, no. 8, p. 085902, 2002.

[38] F. K. LeGoues, R. Rosenberg, and B. S. Meyerson, "Kinetics and mechanism of oxidation of SiGe: Dry versus wet oxidation," *Appl. Phys. Lett.*, vol. 54, no. 7, pp. 644–646, 1989.

[39] M. Spadafora *et al.*, "Oxidation rate enhancement of SiGe epitaxial films oxidized in dry ambient," *Appl. Phys. Lett.*, vol. 83, no. 18, pp. 3713–3715, 2003.

[40] F. K. LeGoues, R. Rosenberg, T. Nguyen, F. Himpsel, and B. S. Meyerson, "Oxidation studies of SiGe," *J. Appl. Phys.*, vol. 65, no. 4, pp. 1724–1728, 1989.

[41] C. Tételin, X. Wallart, J. P. Nys, L. Vescan, and D. J. Gravesteijn, "Kinetics and mechanism of low temperature atomic oxygen-assisted oxidation of SiGe layers," *J. Appl. Phys.*, vol. 83, no. 5, pp. 2842–2846, 1998.

[42] O. W. Holland, C. W. White, and D. Fathy, "Novel oxidation process in Ge$^+$ implanted Si and its effect on oxidation kinetics," *Appl. Phys. Lett.*, vol. 51, no. 7, pp. 520–522, 1987.

[43] J. H. Oh *et al.*, "Chemical structure of the ultrathin SiO_2/Si(100) interface: An angle-resolved Si 2p photoemission study," *Phys. Rev. B*, vol. 63, no. 20, p. 205310, 2001.

[44] P. J. Grunthaner, M. H. Hecht, F. J. Grunthaner, and N. M. Johnson, "The localization and crystallographic dependence of Si suboxide species at the SiO_2/Si interface," *J. Appl.*

Phys., vol. 61, no. 2, pp. 629–638, 1987.

[45] G. Hollinger and F. J. Himpsel, "Probing the transition layer at the SiO$_2$-Si interface using core level photoemission," *Appl. Phys. Lett.*, vol. 44, no. 1, pp. 93–95, 1984.

[46] F. J. Grunthaner, P. J. Grunthaner, R. P. Vasquez, B. F. Lewis, J. Maserjian, and A. Madhukar, "High-Resolution X-Ray Photoelectron Spectroscopy as a Probe of Local Atomic Structure: Application to Amorphous SiO$_2$ and the Si-SiO$_2$ Interface," *Phys. Rev. Lett.*, vol. 43, no. 22, pp. 1683–1686, Nov. 1979.

[47] F. J. Himpsel, F. R. McFeely, A. Taleb-Ibrahimi, J. A. Yarmoff, and G. Hollinger, "Microscopic structure of the SiO$_2$/Si interface," *Phys. Rev. B*, vol. 38, no. 9, pp. 6084–6096, 1988.

[48] D. Schmeisser *et al.*, "Surface oxidation states of germanium," *Surf. Sci.*, vol. 172, no. 2, pp. 455–465, Jul. 1986.

[49] A. Molle, M. N. K. Bhuiyan, G. Tallarida, and M. Fanciulli, "In situ chemical and structural investigations of the oxidation of Ge(001) substrates by atomic oxygen," *Appl. Phys. Lett.*, vol. 89, no. 8, pp. 083504–083506, Aug. 2006.

[50] K. Prabhakaran, F. Maeda, Y. Watanabe, and T. Ogino, "Distinctly different thermal decomposition pathways of ultrathin oxide layer on Ge and Si surfaces," *Appl. Phys. Lett.*, vol. 76, no. 16, pp. 2244–2246, 2000.

[51] J. M. Madsen, Z. Cui, and C. G. Takoudis, "Low temperature oxidation of SiGe in ozone: Ultrathin oxides," *J. Appl. Phys.*, vol. 87, no. 4, pp. 2046–2051, Feb. 2000.

[52] Z. H. Lu, M. J. Graham, D. T. Jiang, and K. H. Tan, "SiO$_2$/Si(100) interface studied by Al Kα x-ray and synchrotron radiation photoelectron spectroscopy," *Appl. Phys. Lett.*, vol. 63, no. 21, pp. 2941–2943, 1993.

[53] S. J. Kilpatrick, R. J. Jaccodine, and P. E. Thompson, "Experimental study of the oxidation of silicon germanium alloys," *J. Appl. Phys.*, vol. 93, no. 8, pp. 4896–4901, 2003.

[54] S. J. Kilpatrick, R. J. Jaccodine, and P. E. Thompson, "A diffusional model for the oxidation behavior of Si$_{1-x}$Ge$_x$ alloys," *J. Appl. Phys.*, vol. 81, no. 12, pp. 8018–8028, 1997.

[55] M. K. Bera *et al.*, "Rapid thermal oxidation of Ge-rich Si$_{1-x}$Ge$_x$ heterolayers," *J. Vac. Sci. Technol. A Vacuum, Surfaces, Film.*, vol. 24, no. 1, pp. 84–90, 2006.

[56] A. Agarwal, J. K. Patterson, J. E. Greene, and A. Rockett, "Ultraviolet ozone induced oxidation of epitaxial Si$_{1-x}$Ge$_x$(111)," *Appl. Phys. Lett.*, vol. 63, no. 4, pp. 518–520, 1993.

Chapter 2: Experimental Review of Ambient Pressure X-ray Photoelectron Spectroscopy

2.1   Introduction to X-ray Photoelectron Spectroscopy

In Chapter 1, the use of X-ray photoelectron spectroscopy (XPS) was introduced as an experimental method of observing the atomic composition and nature of chemical bonds at the near-surface region of semiconductor materials (Si, Ge, and $Si_{1-x}Ge_x$) and their respective oxides. In this chapter, the details of how this experimental technique is particularly suited for this task will be discussed. Two important concepts to understand XPS are the photoelectric effect and photoelectron mean free path.

In section 1.1 of Chapter 1, the band theory of semiconductors was introduced which briefly discussed valence band electrons and core electrons of atoms in a crystal. It is the core electrons that are the primary interest in XPS for our studies. The binding energy (E_b) of each core electron, which is conceptually (but not strictly) equivalent to ionization energy of that electron, is characteristic of the individual atom to which it is bound [1]. When photons with an energy greater than the binding energy of electrons impinge on an atom, photoionization takes place and photoelectrons are emitted in a process called the photoelectric effect. This process results in the formation of core holes. The resultant photoelectrons have a kinetic energy (E_k) which is related to the impinging photon energy (hν), work function of sample (Φ), and E_b by the Einstein relation which is given in equation 1 [1].

$$E_k = h\nu - E_b - \Phi \qquad (1)$$

Since the energy levels in an atom are quantized, the photoelectrons have an energy distribution N(E) consisting of a series of discrete bands that essentially reflects the "shell" form of the electron structure of the atom [1]. When X-rays impinge on a semiconductor surface,

photoelectrons with sufficient kinetic energy can escape the surface of the sample and if their trajectory is right they can be "collected" and analyzed to reveal the electronic structure and thus nature of the chemical bonds in the sample. The photoelectric effect is the core process that describes how XPS works.

When a photoelectron is created in a sample, before it can be collected and analyzed it can experience a variety of energy loss events. The deeper in a sample that the photoelectron originates, the higher the probability that that it will be scattered by collisions with other atomic nuclei (elastic) and other electrons (inelastic). This in essence is how XPS is a surface sensitive experimental technique, as photoelectron must travel through the solid and escape into vacuum, without energy loss, before it can be energy analyzed and detected as a characteristic subshell photoelectron [1]. X-rays are able to penetrate 1-3 μm into a sample [2], but the stopping power for electrons in a solid is several orders of magnitude higher than for X-rays. For take-off angles normal to the surface, roughly the first 10 nm (20-40 atomic layers) of material are probed before they lose energy through inelastic scattering events with other electrons and hence cannot contribute to the characteristic elastic photoelectron peak [2]. The intial photoelectron intensity (counts per second) from a characteristic peak, I_0, is attenuated as a function of depth into the sample (x), emission angle of the photoelectrons relative to the surface normal (θ), and a material and energy dependent constant known as the inelastic mean free path (IMFP, λ). The λ represents the average path length than an electron travels between two successive inelastic interactions [3]. Since it is a random process governed by probability, inelastic scattering is described by the standard exponential decay law given by equation 2 [1].

$$I(x) = I_0 \exp(-x/ \lambda(E_k, Z) \cdot \cos(\theta) \qquad (2)$$

Where Z is the atomic number. The λ dependence on E_k and Z was derived from experimental data by Seah & Dench [4] to be $\lambda \propto E_k^{1/2}$. The "universal curve" of IMFP with electron energy has a minimum where elastic scattering is surface sensitive, and is only weakly dependent on the chemical identity of the solid [2]. Synchrotron radiation experiments performed by Hollinger & Himpsel discussed in Chapter 1 had an incident photon energy of $h\nu = 130$ eV, which for Si 2p emission results in photoelectrons near the minimum of the universal curve and thus maximized surface sensitivity for their interfacial experiments. The experiments by Oh et al. [5] utilized the fact that approximately 63% of the photoelectrons contributing to a particular feature must originate within a distance of $\lambda \cdot \cos(\theta)$ of the surface, which for practical purposes can serve as a measure of sampling depth, d [1]. Since d varies with $\cos(\theta)$, sampling depth may be controlled by varying the angle of emission from 0° ($d=\lambda$) to 80° ($d=0.17\lambda$) [1]. It is important to note the difference between λ and attenuation length, as these terms are often used interchangeably but the difference between them can vary by as much as 30% [6]. The elastic mean free path, or the distance an electron travels before elastic collisions with atomic nuclei, is several times smaller than λ [3] so many of these collisions can occur in an electron's path before an inelastic event. These elastic collisions increase the mean path length, which are accounted for in λ, but are neglected in the attenuation length, L. The result is for a Si 2p photoelectron from SiO_2, the L/λ ratio reported in literature ranges from 0.885 to 0.918 for Mg Kα and Al Kα excitation, respectively [7]. Standard XPS quantification equations adopt the straight line approximation (SLA), which assumes that electrons follow straight line paths from creation to emission, therefore experience no elastic scattering [8]. Therefore when using these equations, the most accurate results are obtained by using in L instead of λ when accounting for electron transport [8].

After ionization of a core level, the atom can relax in a couple ways. A higher lying (core or valence) electron can fill the resulting hole and relax in a radiative process: a core hole created in the K band is filled by one in the higher L_{II} band resulting in the emission of radiation with hv $= (E_K – E_{LII})$, or in the same process the system relaxes by ejection of a second electron, say from the L_{III} band. The kinetic energy of this electron would be given by $E_k = E_k – E_{LII} – E_{LIII} – \Phi$. If these electrons have enough kinetic energy to escape into vacuum and are emitted in the right direction they can also be detected by the spectrometer. These electrons are called Auger electrons and can be used for quantitative chemical analysis. However, the energy of an Auger transition is difficult to calculate precisely as many electron effects and final state energies have to be considered [2]. The exact energy and lineshape of an Auger transition need only be considered in the highest resolution applications [2].

In addition to the main photoelectron and Auger electrons, the spectra from XPS is defined by other signals originating from scattered electrons and other forms of radiation induced by the incident X-rays. Each spectrometer analyzer (to be discussed more later) has a solid acceptance angle, a term which dictates the portion of the sample photoelectrons that the spectrometer can "see." Any photoelectron which has sufficient kinetic energy and is emitted within the acceptance angle of the spectrometer can be detected, this includes scattered electrons and secondary electrons [2]. Scattered electrons are photoelectrons that make it to the analyzer but have been scattered either by atomic nuclei in an elastic event or by another electron in an inelastic event. Inelastically scattered primary and Auger electrons can excite the emission of other electrons from the sample called secondary electrons with a continuous range of energies down to zero (or the low energy cut-off in the spectrometer) [2]. The signal acquired by an XPS spectra, or the number of electrons as a function of kinetic energy of the electrons N(E), is then

composed of photoelectrons and Auger electrons with a continuous background formed by the

scattered and secondary electrons [2]. The background can also have some structure, including

loss features known as plasmons which arise from collective oscillation of the sea of electrons;

these oscillations have frequencies characteristic of the solid [9]. Depending on the type of

excitation X-rays used (discussed more later), and its purity, satellite and ghost peaks can appear

in the background as well. Weaker satellites near the background intensity arise from less

probable transitions or transitions in a multiply ionized atom [9]. "Shake up" satellites have a

strong signal, and arise from perturbation of the valence band electrons due to loss of a core level

electron [9]. Ghost peaks are due to excitations arising from impurity elements in the anode [9].

With the primary signals and background defined, a complete XPS spectra can be presented.

Figure 2.1 below is a survey spectra, or complete photoelectron energy distribution, of an

oxidized $Si_{1-x}Ge_x$ sample with carbonaceous contamination.
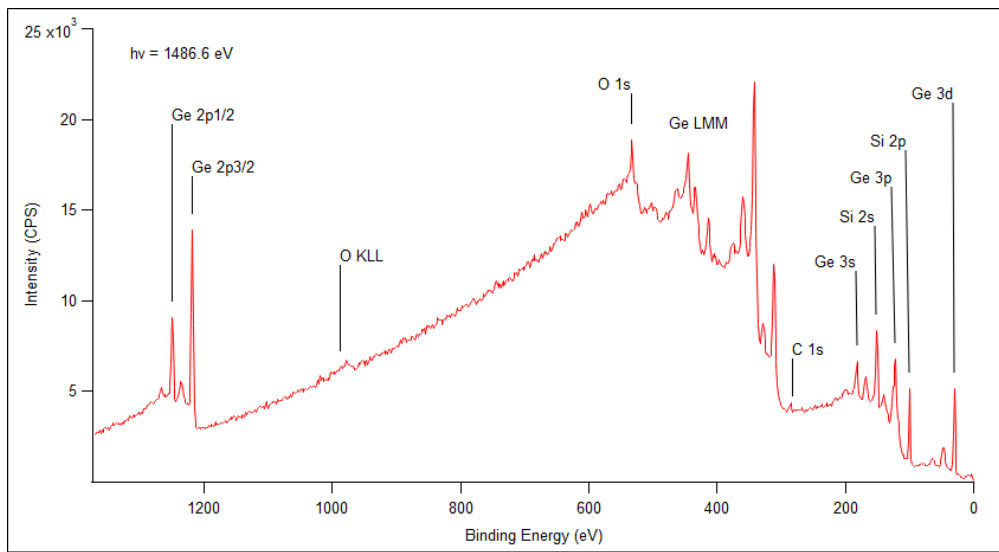
Figure 2.1: Photoelectron energy distribution N(E) with binding energy for a $Si_{1-x}Ge_x$ sample with carbonaceous contamination using Al Kα X-rays with hν = 1486.6 eV. Primary "no loss" peaks commonly used for chemical analysis have been labeled.

The characteristic core photoelectron peaks are much narrower and simpler when compared to the broad and complicated Auger peaks, labeled as Ge LMM and O KLL. The O 1s and C 1s XPS peaks arise due to small amounts of surface oxidation and adventitious carbon contamination, respectively, on the surface of the $Si_{1-x}Ge_x$ sample. On the high binding energy side of the core photoelectron peaks are "inelastic tails" from inelastically scattered photoelectrons that have lost energy [10]. In the inelastic tail region of some transitions are unlabeled peaks, which are due to plasmon losses [10].

The number of photoelectrons that arrive at the spectrometer for any given characteristic transition is paramount, as more photoelectrons increases the signal to noise ratio and statistical confidence in statements made about changes in the chemical environment. Many factors can severely reduce the number of substrate photoelectrons detected for a core level photoelectron, these include scattering by gas molecules between the specimen surface and the spectrometer analyzer and attenuation by contamination layers. The mean free path of electrons in the gas phase should be much greater than the dimensions of the spectrometer; considering scattering by gas molecules alone this imposes a pressure limitation for conventional XPS of about 10^{-5} to 10^{-6} mbar [11]. However, pressures much lower are required to prevent a deleterious amount of gas molecules from sticking to the surface of the sample. From kinetic gas theory, a monolayer of gas will accumulate on a surface in 1.5 seconds at a pressure of 10^{-6} mbar and room temperature if every molecule hitting the surface stays there on impact (sticking probability of unity) [11]. As even a small amount of surface contamination can alter the experimental results significantly, in practice the base pressure for conventional XPS is usually around 10^{-10} mbar. This results in a contamination accumulation rate that is much slower than the rate of chemical change being observed at the surface [11]. These operating pressures are considered ultra-high vacuum (UHV),

a specification that is a defining characteristic of XPS spectrometers. To achieve these conditions a spectrometer must have an extensive system of vacuum pumps. This includes roughing pumps (down to $\sim 10^{-2}$ mbar), turbo pumps (down to $\sim 10^{-9}$ mbar), and ion entrapment pumps. Before use of ion entrapment pumps, the system typically will also be baked out to temperatures $>100°C$. This is done to desorb contaminants like water from the inner surfaces of the spectrometer. After bake out and using ion entrapment pumps pressures of about 10^{-9} to 10^{-10} mbar can routinely be achieved. Improvements in spectrometers have drastically increased the counts per second (CPS) of electrons from a given characteristic transition; average achievable CPS in 1974 was about 1000 and by 1992 was near 150,000 [12]. Much of this improvement was achieved by modifying electron optics and electron detectors, not in vacuum design. These advances have allowed the advancement of ambient pressure XPS techniques [13], which will be discussed in more detail later in this chapter.

Qualitative analysis of photoelectron energy distributions require high resolution spectra, obtained to distinguish between electrons from a specific transition and ones that may have been shifted by small changes in the chemical environment. The chemical shift depends on the oxidation state of the atom. As more electrons are removed from the host nucleus by a substituent, the effective positive charge increases causing greater electrostatic attraction and increasing binding energy with each oxidation state [2]. Moreover, the greater the electron withdrawing power of the substituents bound to an atom the higher the binding energy [2].

Resolution in XPS can be expressed in two forms. The first, called the absolute resolution, ΔE, is usually measured as the full width at half-maximum (FWHM) height of a chosen peak [11]. The absolute resolution is due to many factors including instrumental and intrinsic effects. Often, the absolute resolution of the instrument can be estimated using the Ag

$3d_{5/2}$ transition from a clean Ag sample [14]. The other measure of resolution is the relative resolution defined as $R = \Delta E/E_0$ where E_0 is the kinetic energy at the peak position and ΔE is the peak FWHM; this can alternatively be expressed as the resolving power $\rho = 1/R = E_0/\Delta E$ [11]. XPS utilizes characteristic X-ray emission lines from an anode which is bombarded by high energy electrons. A suitable X-ray source material should have a photon energy high enough to excite core electrons of all elements, should have a clean X-ray spectrum with few satellites (low atomic number), and should have a narrow characteristic linewidth compared to the sample core-level linewidths and expected chemical shifts [1]. The most commonly used X-ray sources in XPS are Al-Kα (hν = 1486.6 eV, FWHM = 0.85 eV) and Mg-Kα (hν = 1253.6 eV, FWHM = 0.7 eV) [1]. These line widths represent the highest possible resolution in XPS quantitative analysis without using a monochromator. For the electron analyzer to match the absolute resolution to these X-ray natural line widths would require a relative resolution of $\sim 6 \times 10^{-4}$ (or resolving power of $\sim 1,700$) [11]. Higher X-ray resolution has been achieved by monochromatization of Al-Kα X-ray lines using diffraction from the (1010) face of a bent quartz single crystal [1]. In this manner the X-ray linewidth is reduced to about 0.2 eV and all satellite, ghost, and Bremsstrahlung radiation is filtered out [1]. This changes both resolution and signal to noise ratio. However, to match the absolute resolution to a monochromatized X-ray line would require a relative resolution of $\sim 10^{-4}$ (resolving power of 10,000) [11]. This would require very large and expensive analyzer, without some other sort of processing.

The analyzer is where processing of the energy distribution spectrum occurs. This analysis will focus on the concentric hemispherical analyzer (CHA) and its basic operation. A CHA uses an electrostatic field to disperse the electron energies so that for a given field only those electrons with energies in a certain narrow energy range are measured [11]. Before

entering the analyzer the electron energies are retarded. Measurements are typically obtained in

two modes for CHAs. In the constant retard ratio (CRR) mode, electrons are decelerated by a

constant factor from their initial kinetic energies. In constant analyzer energy (CAE) mode,

electrons are decelerated to a constant pass energy [11]. In either case, retardation enables the

same absolute resolution to be obtained for a lower relative resolution [11]. For example, if

retardation to a 50 eV pass energy were chosen an absolute resolution of 0.7 eV would require a

relative resolution of only $\sim10^{-2}$. With this retardation feature, CHAs are able to achieve relative

resolutions as high as 5×10^{-4} (resolving power ~2000) and are therefore the most appropriate

commercially available analyzer if very high resolution is required [12]. Figure 2.2 offers a

summary of how a monochromator filters out satellites and background to excite photoelectrons

from a sample with the Al-Kα characteristic line only, and how the CHA retards electrons to

achieve an absolute resolution of 0.4 eV.
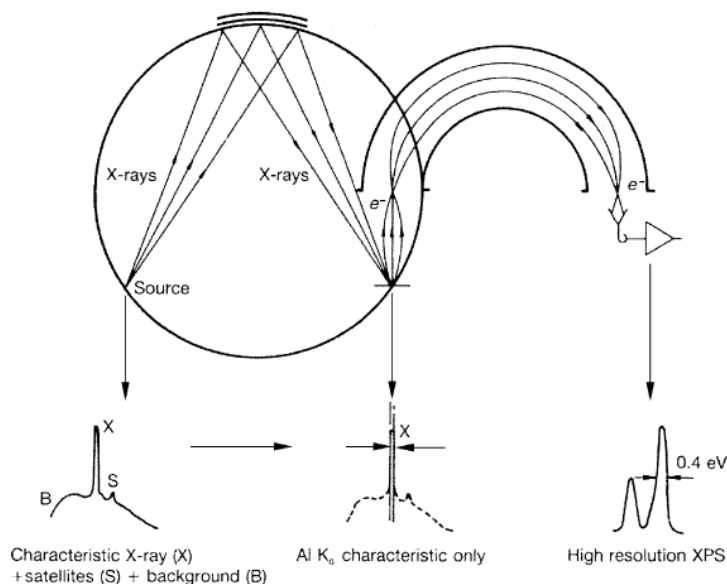
Figure 2.2: Mode of operation of the monochromator used in X-ray photoelectron spectroscopy. X-ray satellites and background are filtered out so that only Al-Kα X-rays impinge on the sample. CHA retards electrons to achieve 0.4 eV absolute resolution [12].

There exists a tradeoff between resolution and signal to noise ratio that must be considered. The spectra in Figure 2.1 was obtained with pass energy of 100 eV, and is defined by high signal to noise ratios for the core transitions but with low resolution. The high resolution XPS shown inlaid in Figure 2.2 would require lower pass energy, e.g. around 24-50 eV, and is defined by high enough resolution to observe spin orbit separations but lower signal to noise ratio. When designing an experiment in XPS it is necessary to consider what resolution is needed as well as the signal to noise ratio. Considerations should also include the rate necessary to obtain spectra compared to the rate of chemical change at the surface.

2.2   Ambient Pressure X-ray Photoelectron Spectroscopy

In the past, most XPS experiments were performed in UHV conditions to control exposure of the sample surface to contaminants and to minimize scattering by gas molecules. However, for the study of many important surface phenomena investigations under elevated pressure conditions are essential to overcome the pressure gap. This can be explained by the difference in chemical potential of a gas at UHV conditions (10^{-9} mbar) compared to realistic pressure in a technical process or in the environment (10^{-2} to 10^2 mbar) [15]. Experimental methods have been used, such as ex-situ oxidation, to monitor chemical changes at interfaces without having to expose the XPS chamber to higher than UHV pressures. This method was an effective, albeit indirect, method of characterizing surface reactions. The potential of XPS to monitor a variety of reactions in real time (e.g. oxidation, catalytic, electrochemical) drove research towards the development of an ambient pressure X-ray photoelectron spectrometer [15].

The ability of XPS to detect the transformation of gaseous reactants, changes in surface oxidation states, and shifts in surface potential makes ambient pressure XPS (APXPS) ideal to monitor catalytic reactions and electrochemical processes [13]. The first studies at conditions above high vacuum were performed by Seigbahn's group in the 1970s which introduced differential pumping as a method of having the analysis chamber and analyzer at different pressures [16]. Kelly et al. achieved analysis pressures as high as ~0.02 mbar with a differentially pumped system and electrostatic grid lenses to improve count rates [17]. Ogletree et al. designed a prototype system which built upon differential pumping and electrostatic lenses to achieve reasonable count rates at pressures up to 7 mbar [18]. These studies suggested that photoemission experiments would be possible up to 100 mbar. A second generation analyzer developed with improved electron optics and a new chamber design for easier sample manipulation and transfer demonstrated that APXPS at ~100 mbar was possible [19]. While typical pressures in APXPS experiments are in the mbar range, Pt 4f spectra have been collected at 133 mbar of O_2 with an accumulation time of 90 minutes [13]. The primary improvements that make these second generation APXPS instruments possible will be discussed here.

Recall from section 2.1 that for an XPS instrument to operate, the mean free path of the photoelectrons in the gas phase must be longer than the dimensions of the spectrometer. This becomes much more difficult when working in pressures above UHV, as electron scattering dramatically reduces signal and steps must be taken to protect the sensitive electronics in the analyzer. Differential pumping systems were developed as a method to keep the analyzer at UHV while holding the analysis chamber at higher pressures for experimentation. For the SPECS instrument used in this analysis, three differentially pumped stages with a total of four turbomolecular pumps protect the analyzer. The pumping efficiency is improved by placing the

entrance to the first pumping stage far from the sample with a small entrance aperture (if the radius of the aperture is R, a large distance is +8R), but this comes at the cost of detection efficiency. Small apertures spaced at large distances improve differential pumping, but decrease the effective solid angle of the transmitted electrons, while large apertures increase transmission of electrons but compromise the vacuum in the electron energy analyzer [20]. Additionally, there is a minimum distance at which the sample should be kept from the aperture to ensure homogenous pressure conditions across the sample surface [20]. Assuming molecular flow of gas and a sample placed distance z from an entrance aperture R, the local pressure varies with background pressure by distance z such that at $z = R$ the pressure is less than 90% of background pressure while at $z = 2R$ the pressure is already >95% of background pressure [20]. With these factors in consideration, an experimental summary by Salmeron et al. found that for a common entrance aperture of $R = 0.25$ mm, sample distance z was varied between $0.5 – 2$ mm (2R to 8R) depending on the experiment so that pressure near the sample is very close to the background pressure [21].

Electron attenuation is a function of the type of gas and electron kinetic energy in addition to travel distance, pressure, and temperature. Using gases with large scattering cross sections (discussed more in section 2.3) and observing electrons with low kinetic energy require even higher sensitivity [20]. As mentioned earlier through the works of Kelly and Ogletree, this was accomplished with electrostatic lenses in addition to optimizing photon source flux [17], [18]. Due to the solid acceptance angle of each entrance aperture, only a fraction of the photoelectrons that enter the first aperture make it through the second. Using Einzel lenses in each pumping stage, the electron beam is refocused to collect all of the electrons that are accepted through the aperture [21]. In a commercial SPECS Phoibos analyzer, a quadrupole lens

in the third chamber steers the emitted photoelectrons to the entrance of the concentric

hemispherical analyzer [21]. Finally, to maximize the number of photoelectrons making it

through the first aperture a photon source with high flux and a small photon beam size, as closely

as possible matching that of the entrance aperture, is ideal [13]. Synchotron radiation is best for

this, however commercial focused Al Kα monochromatized sources can be used as well [13].

Figure 2.3 shows the typical orientation of the sample, aperture, and incident photon beam, as

well as how the differential pumping and electrostatic lens system in APXPS instruments work

to minimize attenuation and focus photoelectrons for analysis.
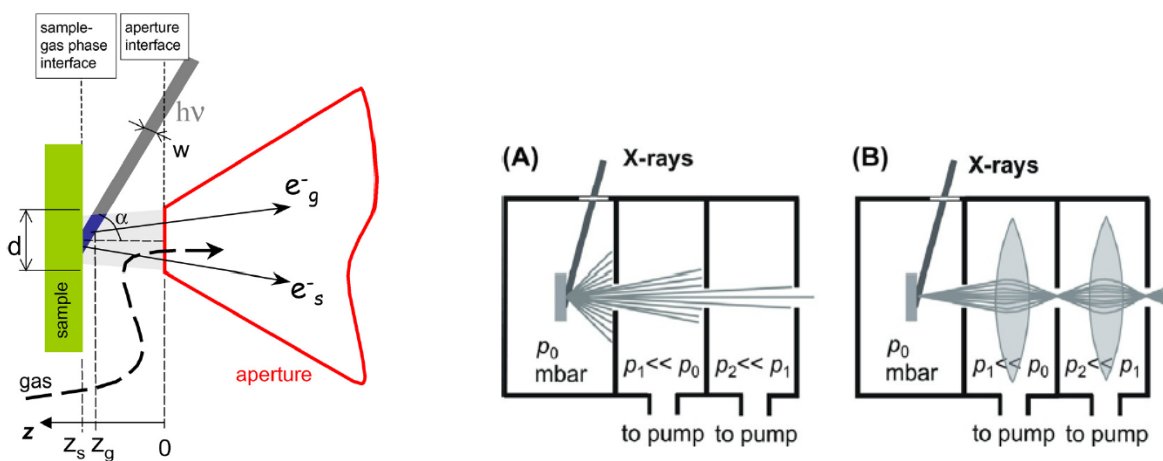
Figure 2.3: (left) Orientation of the sample, aperture, and photon beam that irradiates both the surface

and gas phases. (right) Transmission of photoelectrons through the differential pumping system (a)

without electrostatic lenses resulting in loss of intensity and (b) with electrostatic lenses to collect

electrons for analysis [13].

The minimum aperture size, d, will be selected to closely match the surface area irradiated by the

photon beam, and is typically larger than 100 μm [13]. Referring to Figure 2.3, the irradiated

area is a function of the X-ray beam width, w, and X-ray incident angle relative to the surface

normal, α. As the aperture size increases the flux of gas through the aperture will also increase.

Thus, aperture size selection will be a function of desired pressure in the analysis chamber to maintain pumping efficiency.

An unavoidable side effect of APXPS is the gas-phase adsorption of incoming photons and subsequent photoemission that can be detected at pressures above 10^{-2} mbar [13]. This side effect has proven to be quite advantageous, as it can offer simultaneous chemical information about gas-phase reactants and products particularly when coupled with mass spectrometry [13]. Moreover, electrons generated in the gas phase can help reduce sample charging in the case of insulating samples depending on the type of gas and incident photon energy [13].

As nearly all the other components of the APXPS instrument must be kept at UHV, the analysis chamber and aperture to the differential pumping section is isolated by a thin silicon nitride window. Low-stress silicon nitride windows with an active window area of 0.5mm × 0.5mm and a thickness of 100 nm can withstand pressure differentials of one atmosphere, i.e. the sample cell can be vented to atmosphere without compromising the vacuum in the X-ray source [10]. While transmission through this silicon nitride window is high for Al Kα X-rays, it does result in a slight decrease in intensity of the incident photon beam.

2.3   SPECS APXPS Instrument Testing

Before accurate chemical analysis using an XPS instrument can be performed, where observed binding energies are compared with literature values to characterize surface chemistry, the binding energy scale should be defined. Without an accurately defined scale, a full interpretation of the spectra gathered on different instruments is limited [22]. Energy calibrations are often performed by presenting binding energy tabulations for copper, silver, and gold. These elements have the advantages of being easily cleaned and chemically inert as well as being stable

conductors [22]. To calibrate the spectral scale of the SPECS APXPS instrument, a silver sample was used to monitor the binding energy of the $Ag3d_{5/2}$ characteristic transition using Al-Kα X-rays. From literature, the binding energy of $Ag3d_{5/2}$ under Al-Kα excitation should occur at 368.27 ± 0.02 eV [22]. Figure 2.4 shows high-resolution spectra taken from the UHV manipulator of the SPECS AP-XPS instrument using Al-Kα monochromatized X-rays with an analyzer pass energy of 35 eV.
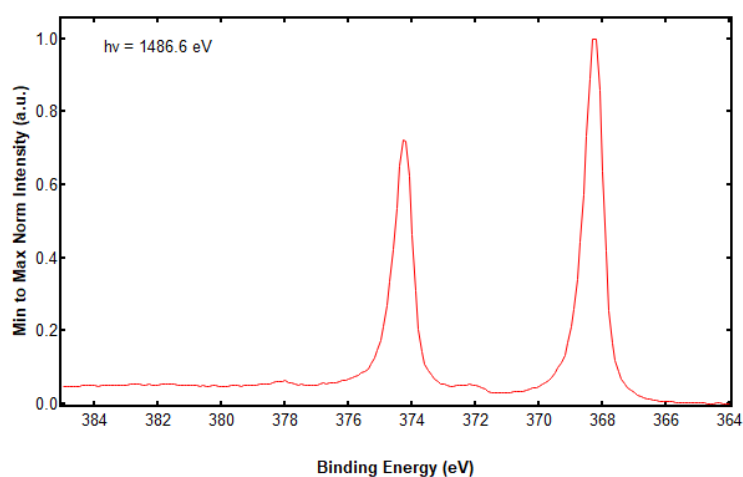
Figure 2.4: High resolution Ag 3d spectra excited with Al-Kα monochromatized X-ray source. Intensity has been normalized to raw data minimum and maximum intensity.

The experimentally determined binding energy of the $Ag3d_{5/2}$ transition is 368.28 eV, which is within error of the literature tabulated value. The data indicate that the spectral scale for the instrument in correctly calibrated. It should be noted that the most accurate calibration is referencing zero to the Fermi level of conducting samples, however it has been determined through XPS data meta-analysis that positioning of the zero point introduces an error of about 0.3 eV [22]. This error should be taken into consideration when comparing binding energies between literature references.

From the discussion in Chapter 2, it is known that in ambient pressure XPS there is a tradeoff between instrument sensitivity (counts from no-loss photoelectron peaks) and desired experimental chamber pressure. Moreover, the silicon nitride window which allows X-rays to pass into the NAP cell can reduce photon flux at the sample surface slightly thus decreasing photoelectron counts. To optimize future experiment sensitivity, understanding how photoelectron counts change with analysis cell (UHV versus NAP) and pressure in the NAP chamber at varying pass energies is essential. As the surface should be inert during these experiments to eliminate surface chemistry as contributing to observed changes, nitrogen gas was used in the NAP cell at pressures from 0.1 mbar to 10 mbar. In Figure 2.5 FWHM of the $Ag3d_{5/2}$ transition was plotted with pass energy at UHV in both cells (UHV and NAP) and at 0.1, 1, and 10 mbar in the NAP cell.
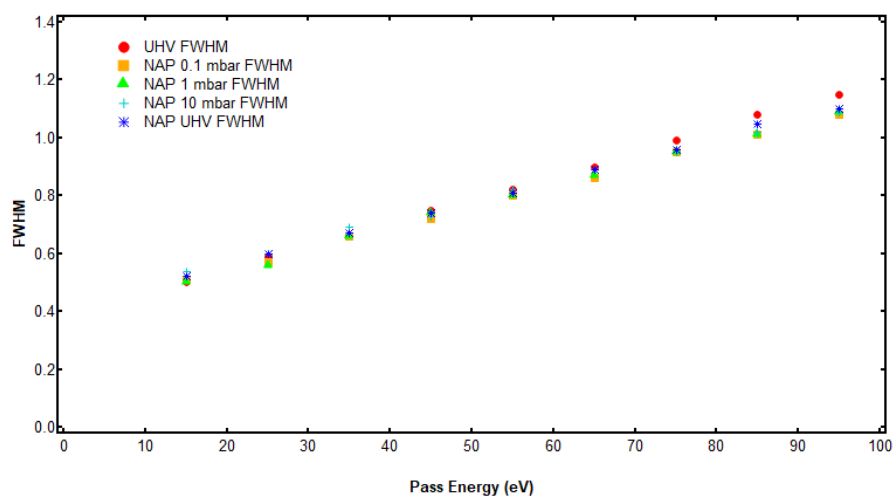
Figure 2.5: High resolution Ag $3d_{5/2}$ FWHM dependence on pass energy in both SPECS analysis chambers at UHV, and at 0.1 to 1 mbar nitrogen in NAP cell.

As expected FWHM increases monotonically with pass energy. SPECS instrument manipulator cell (UHV or NAP) and nitrogen pressure have little effect on $Ag3d_{5/2}$ FWHM, verifying a

chemically inert surface even at high pressures of nitrogen. While UHV cell data appears to deviate from NAP UHV at high pass energies, the relatively large error introduced by peak fitting suggests the difference is likely within error and thus no difference is present.

With a chemically inert surface verified, the change in instrument sensitivity with analysis cell and NAP pressure can be observed. Raw experimental Ag3d spectral data was fit with a convolution of a symmetrical Gaussian-Lorentzian and asymmetrical Doniac-Šunjić profiles (described in more detail in section 2.5), the latter to account for a large inelastic tail attributed to the many-body effects observed in some transition metals like Ag [23]. The calculated Ag3d$_{5/2}$ areal intensity was then plotted against pass energy; the results can be seen in Figure 2.6.
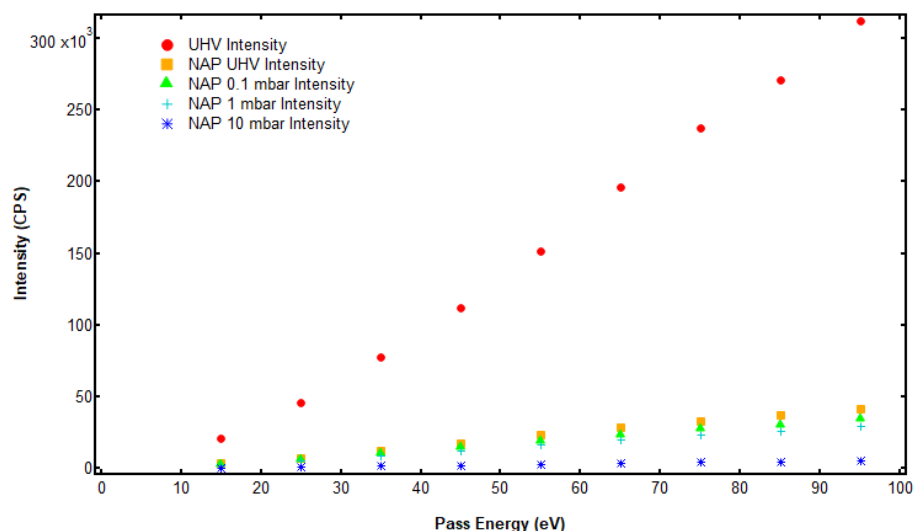
Figure 2.6: High resolution Ag 3d$_{5/2}$ areal intensity dependence on pass energy in both SPECS analysis chambers at UHV, and at 0.1 to 1 mbar nitrogen in NAP cell.

It is observed that the analysis chamber has a strong effect on Ag3d$_{5/2}$ intensity, with intensity in the NAP cell significantly lower than UHV cell intensity at all pass energies. This difference

becomes more pronounced as pass energy is increased. This decrease in sensitivity can be contributed to the small area of acceptance of the cone and, to a much smaller degree, the silicon nitride window. Importantly, little to no decrease in sensitivity is observed from NAP UHV to NAP 1 mbar. This is to say that the kinetic energy of the $Ag3d_{5/2}$ photoelectrons is large enough, and the electron scattering cross section of nitrogen small enough, that only a very small number of photoelectrons are attenuated at pressures up to 1 mbar. The effect of NAP cell gas pressure, distance between the sample and entrance aperture, and electron scattering cross section on the signal intensity compared with the same signal at UHV conditions is given by the Beer-Lambert law [13]. The relationship dictates exponential decrease in intensity with pressure relative to UHV conditions; this explains the quite large sensitivity decrease observed for NAP cell nitrogen pressure of 10 mbar.

Using the data in Figure 2.6, decisions can be made about ideal experimental conditions for future experiments. As mentioned in section 2.2, XPS studies at pressures in the range of 10^{-2} to 10^2 mbar are desirable as many oxidative, catalytic, and electrochemical reactions of interest take place at these conditions [15]. Thus, experiments in the APXPS instrument should be run at pressures as close to realistic conditions as possible without sacrificing too much sensitivity. The observed $Ag3d_{5/2}$ intensities at 10 mbar nitrogen are quite low, which could make accurate analysis difficult. However, the data indicates experiments can be run at 1 mbar without compromising photoelectron counts. A decision on appropriate pass energy should be made based on the tradeoff between resolution, sensitivity, and collection time. Figure 2.6 does however suggest a lower limit on pass energy of 35 eV, below which $Ag3d_{5/2}$ areal intensity is quite low.

2.4   Quantitative Surface Analysis

Quantitative analysis with X-ray photoelectron spectroscopy requires accurate intensity measurements of spectral lines for different elements or different chemical states of one element [24]. These intensity measurements can be used to determine the location, relative intensity, and line shapes of the various peaks observed even when they are not clearly resolved from one another [10]. This process is complicated by the inelastic scattering tail on the low kinetic energy side of each transition, e.g. plasmons, the background from secondary electrons, Bremsstrahlung radiation, and a host of processes that determine the basic peaks shape observed in XPS [10].

The number of photoelectrons produced from any given core level of an element, or its spectral line intensity, is determined by the photoionization cross-section of that level for the photon energy concerned [1]. The photoelectric cross-section, σ, is defined as the transition probability per unit time for exciting a single atom, single molecule, or solid specimen to an excited state with a unit incident photon flux of 1 $cm^{-2}s^{-1}$ [10]. The photoelectric cross-section depends on incident photon energy hν, E_b atomic number (Z), and the angle between the photon incidence and photoelectron emission, α [1]. When considering α a differential a cross section (dσ/dΩ) can be determined, where dΩ is the differential solid angle into which electron emission occurs [10]. In practice, the differential cross-section for a given subshell n for a randomly-oriented ensemble of atoms excited by monochromatized light is given by the expression

$$\frac{d\sigma_n}{d\Omega}(E_k) = \frac{\sigma_n}{4\pi}\left[1 + \frac{1}{2}\beta_n(E_k)\left(\frac{3}{2}\sin^2\alpha - 1\right)\right] \qquad (1)$$

β_n is the asymmetry parameter which is dependent on the core level of a given atom (n) at a certain photon energy (E_k) and 4π is the complete solid angle of acceptance [1]. Comprehensive tabulations of σ and β can be found in the literature [25]. At a source to analyzer angle of α = 54.7° the effects of the asymmetry parameter in equation 1 are neglected and the differential

cross-section is equal to $\sigma_n/4\pi$ [10]. Equation 1 represents the angular distribution of photoelectrons ionized from a given subshell; this angular distribution has a pronounced effect on intensity of the peak as different lines may have different angular distributions [26]. Therefore at a given sampling depth, the differential cross-section of the expected subshells will play a critical role in their relative intensities [26].

The differential peak intensity from a subshell n can be expressed as the following product for a three dimensional sample in Cartesian space (x, y, z): dN_n= (X-ray flux at x, y, z) · (Number of atoms or molecules in dx, dy, dz) · (differential cross-section for n subshell) · (acceptance solid angle of electron analyzer at x, y, z) · (probability of no-loss escape from specimen with negligible direction change) · (instrumental detection efficiency) [10]. Assuming a homogenous and bounded sample, the differential peak intensity from the substrate k can be represented in the following mathematical form

$$dN_{nk} = I_0 \cdot \rho dx dy dz \cdot \frac{d\sigma_{nk}}{d\Omega} \cdot \Omega(E_k, x, y, z) \cdot \exp(-1/L(E_k)) \cdot D_0(E_k) \quad (2)$$

where dN is the differential peak intensity, I_0 is the X-ray flux, ρ is the atomic density varying with differential volume (dx, dy, dz), $d\sigma_{nk}/d\Omega$ is the differential cross-section, Ω is the solid angle of acceptance, L is the attenuation length in the substrate, and D_0 is the instrumental detection efficiency. Simplifying assumptions are made in order to obtain a form of equation 2 that is integrable. These assumptions are based on an idealized spectrometer; a schematic of such a spectrometer with all accompanying assumptions, along with a list of variables, can be found in Appendix A.1. Using the idealized spectrometer assumptions, the integrated form of equation 2 for a sample of semi-infinite thickness and an atomically clean surface is

$$N_{nk} = I_0 \Omega_0(E_k) A_0(E_k) D_0(E_k) \rho \frac{d\sigma_{nk}}{d\Omega} L(E_k) \quad (3)$$

55

The semi-infinite sample assumption can be made when the sample thickness is large compared to the λ of electrons from the sample. As the sample thicknesses of concern in this study are orders of magnitude larger than λ this is a safe assumption. To account for overlayers whose structure is well understood, like a surface oxide, equation 3 is altered to account for attenuation of the bulk photoelectrons by an oxide of thickness t.

$$N_{nk} = I_0 \Omega_0(E_k) A_0(E_k) D_0(E_k) \rho \frac{d\sigma_{nk}}{d\Omega} L(E_k) \times \exp(-t/L'(E_k) \cos \theta) \qquad (4)$$

where L$^{'}$ is the attenuation length in the overlayer. According to equation 4, the intensity of the substrate peak is exponentially attenuated by the overlayer of thickness t as a strong function of emission angle relative to surface normal, θ. Attenuation of the substrate peak with emission angle is tied to a concurrent increase in intensity from the overlayer.

$$N_{nc} = I_0 \Omega_0(E_k) A_0(E_k) D_0(E_k) \rho' \frac{d\sigma_{nc}}{d\Omega} L'(E_k) \times [1 - \exp(-t/L'(E_k) \cos \theta)] \qquad (5)$$

The new variable $\rho^{'}$ is atomic density in the overlayer. The overlayer/substrate ratio (equation 5/equation 4) is predicted to increase as θ increases, an effect that suggests a general method for increasing surface sensitivity by using grazing angles for electron emission [10]. When studying the fundamental properties of semiconductor surfaces, an atomically clean surface is of vital importance [1], however XPS is often used to analyze industrial samples [1]. In these cases, the pristine surfaces achieved by surface scientists are not possible and as a result surfaces with small amounts of carbon and oxygen contamination are also of interest. The attenuation length of ultra-thin contamination layers is difficult to estimate, so basic quantification can assume no inelastic attenuation in the overlayer [10]. The peak intensity from a contamination overlayer subshell n can then expressed as

$$N_{nc} = I_0 \Omega_0(E_k) A_0(E_k) D_0(E_k) s' \frac{d\sigma_{nc}}{d\Omega} (\cos\theta)^{-1} \qquad (6)$$

The new variable s' is the mean surface density from which peak l originates. Note that from equation 6, the peak intensity from an overlayer is predicted to increase with increasing emission angle θ, similar to equation 5.

The equations above allow the calculation of absolute intensities, however because of sample roughness and a variety of other factors that can influence absolute intensities it is desirable to work with intensity ratios [27]. For substrate and overlayer peaks there are multiple kinetic energy dependent spectrometer terms including the mean solid angle Ω_0, the effective aperture A_0, and the detection efficiency D_0. When comparing the relative intensities of two peaks from photoelectrons that are widely separated in kinetic energy, e.g. Ge $2p_{3/2}$ and Ge 3d, these factors introduce progressively larger amounts of instrument error that are dependent on the specific instrument used. The differential cross-section and attenuation length vary from material to material, but when quantifying the relative intensities of peaks from two elements the ratio of these two quantities remains nearly constant [28]. Therefore with a given X-ray source and angle of emission, the ratios $d\sigma_{n1}/d\Omega$ / $d\sigma_{n2}/d\Omega$ and L_1 / L_2 do not change significantly. This allows relative sensitivity factors (RSF) to be calculated for all elements for a given instrument [28]. These RSFs are empirically derived and account for the kinetic energy dependent instrument factor product $\Omega_0(E_k)$ $A_0(E_k)$ $D_0(E_k)$ and constant differential cross-section and attenuation length ratios. For an instrument they will be determined for different α angles, X-ray sources, and the various electron optics options for the analyzer. For well-established and studied instruments, such as those with an electron analyzer with transmission characteristics of the spherical capacitor analyzer supplied by Perkin-Elmer, documented RSFs are available [28]. For

newer APXPS instruments, no documented RSFs are available so must be calibrated based on empirical data. With equation 3, along with experimentally determined RSFs, chemical concentrations from atomically clean samples can be determined. If we consider photoelectron peaks from each of the two elements, a ratio of equation 3 for each element yields

$$\frac{\rho_1}{\rho_2} = \frac{N_{nk1}/\Omega_0(E_k)A_0(E_k)D_0(E_k)\frac{d\sigma_{nk1}}{d\Omega}L_1(E_k)}{N_{nk2}/\Omega_0(E_k)A_0(E_k)D_0(E_k)\frac{d\sigma_{nk2}}{d\Omega}L_2(E_k)} = \frac{N_{nk1}/S_1}{N_{nk2}/S_2} \qquad (7)$$

where S_1 and S_2 are the RSFs for the two photoelectron peaks. In the case of a thin, poorly characterized overlayer of contamination dividing equation 6 by equation 3 gives an overlayer/substrate ratio, which can be used to solve for fractional coverage by substituting the density, ρ, in equation 3 with the mean surface density of substrate atoms, s, divided by the mean separation between layers of density s in the substrate, d. The non-attenuating overlayer at fractional monolayer coverage expression is useful in surface studies at very low exposures to adsorbate molecules, as they allow an estimation of the fractional coverage from observed peak intensities [10].

$$\frac{s'}{s} = \frac{N_{nc}/\Omega_0(E_k)A_0(E_k)D_0(E_k)\frac{d\sigma_{nc}}{d\Omega}d}{N_{nk}/\Omega_0(E_k)A_0(E_k)D_0(E_k)\frac{d\sigma_{nk}}{d\Omega}L(E_k)\cos\theta} \qquad (8)$$

Note that since equation 8 assumes a non-attenuating overlayer, RSFs cannot be used in the same manner in which they were used in equation 7. However, since RSFs assume a constant attenuation length ratio knowing the RSF and one of the attenuation lengths a priori would allow calculation of the other and subsequent calculation of the fractional coverage.

In chapter 1, it was discussed that precise control over oxide growth on semiconductor material is necessary in device fabrication. To fit the needs of the industry, researchers have

developed accurate methods for calculating the thickness of ultrathin oxides grown on semiconductor substrates like silicon that are accurate to within fractions of a nanometer [7]. A ratio of equations 4 and 5 can be used to calculate the thickness of a well characterized overlayer, however this form of the equation is quite complicated as it includes multiple spectrometer dependent terms. Due to similar kinetic energy for the chemically shifted components the analyzer terms cancel out. This leads to a simplification in the calculation of the intensity ratio of the oxide overlayer to the pure semi-infinite substrate and the experimentally observed intensity ratio of ultrathin oxide to the substrate [7]. In this manner, a ratio of equations 5 and 4 can be simplified to the following equation.

$$\frac{I_{ox}}{I_{sub}} = \frac{I_{ox}^{\infty}}{I_{sub}^{\infty}} \frac{[1-\exp(-t/L'(E_k)\cos\theta)]}{\exp(-t/L'(E_k)\cos\theta)} \qquad (9)$$

which can be rearranged to solve for the thickness of the oxide, d_{ox}.

$$d_{ox} = L'(E_k)\cos\theta \cdot \ln\left(1 + \frac{I_{ox}}{I_{sub}}\frac{I_{sub}^{\infty}}{I_{ox}^{\infty}}\right) \qquad (10)$$

Equation 10 is the basic equation for many studies to determine the oxide thickness on silicon, or alternatively to determine the attenuation length of Si 2p photoelectrons in silicon oxide given the oxide thickness [7]. The same approach has been used to calculate the thickness of germanium oxides on germanium [29]. These equations assume that the kinetic energy of the electrons from the oxide and substrate are the same. Silicon oxide Si 2p electrons have 4 eV lower kinetic energy than for elemental Si 2p electrons from the substrate [7]. The percent difference in kinetic energy is ~0.26% which results in a minor error [7]. Corrections should be made to account for carbonaceous contamination overlayers, however measurements show a small apparent increase in oxide thickness of ~0.015 nm per nm of carbonaceous overlayer [7].

Typical contamination levels are in the range of 0.15-0.3 nm, leading to an estimated increase of

<0.005 nm in the oxide thickness [7]. Seah and Spencer [7] propose increased accuracy in the

oxide thickness can be achieved by including suboxide intensities, with the suboxide method

yielding physical thicknesses on average 0.118 nm larger than the method accounting only for

Si^{4+}. However, there is some uncertainty in the accuracy of suboxide XPS analysis [30] so to

minimize propagation of error the suboxide contribution to physical thickness has been ignored.

Most of the error in calculation of the oxide thickness is attributed to error in estimation of $L'(E_k)$

and the intensity ratio [7].

For a given X-ray flux, only a fraction of the photons result in photoionization from a

given subshell. Of the ionized electrons, only a fraction will be able to make it out of the sample

without experiencing a loss event due to the attenuation length. Of the electrons that make it out

of the sample, only a fraction will be directed toward the aperture according to the analyzer solid

angle. Of the remaining, only a fraction will be detected according to the detection efficiency of

the analyzer. These electrons correspond to the no loss peaks which are used for quantitative

analysis. When instrumental error can be controlled, comparing relative intensities of peaks from

a sample can yield a vast amount of information without detailed calculations. This is

particularly true when the emission angle is varied, which changes the sampling depth. This

method of analysis is called angle-resolved XPS, where the attenuation length allows an estimate

of the thickness and with more rigorous analysis the composition of the different layers

constituting a film [31]. Figure 2.7 is an example of angle resolved XPS applied to a germanium

sample which has some surface contamination.
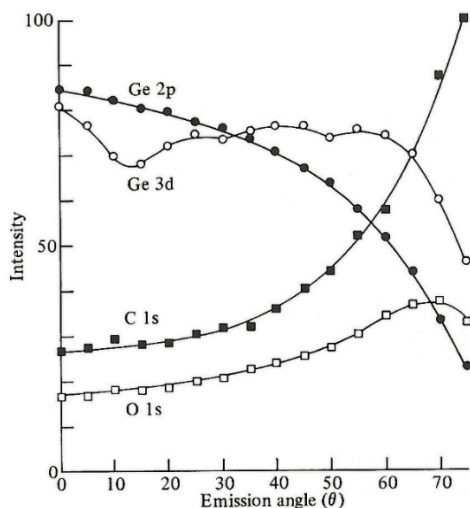
Figure 2.7: Angle resolved XPS applied to a germanium sample. Variation in photoelectron peak intensity (area) with emission angle (θ, with respect to surface normal) [1].

Interpreting Figure 2.7 with equations 4 and 5 yields a significant amount of information. At an emission angle of 0° with respect to surface normal the sampling depth is maximized for all transitions and is equal to λ. The monotonic increase in C 1s intensity from $\theta = 0$ to 75° is indicative of a carbon contamination overlayer, and this behavior mirrors the decrease of the Ge 2p intensity over the same range. This behavior is precisely what one would expect with substrate intensity Ge 2p following equation 4 and overlayer intensity C 1s following equation 5. The O 1s intensity is observed to rise with increasing θ up to = 70°, but then decreases at greater angles. This suggests an oxygen-rich subsurface layer [1]. The Ge 3d intensity is seen to have a complex dependence on θ. This may be understood in terms of the anisotropy of emission of Ge 3d photoelectrons from the single crystal germanium substrate due to diffraction and inelastic scattering events [1]. No structure is observed in the Ge 2p ARXPS profile because these electrons have a very low mean free path compared to the Ge 3d electrons and are influenced less by the substrate crystal structure [1]. The higher mean free path of the 3d photoelectrons is reflected in the relative insensitivity of the 3d intensity to angle, for values of θ up to 60° [1].

61

In addition to the no loss peak intensity, the binding energy of a peak can be used for further analysis. Chemical shifts (i.e. the change in binding energy of a peak from its nominal position) is a very useful characteristic of XPS [32]. These chemical shifts are used to identify the chemical state of an atom (its oxidation state and/or its chemical environment) [32]. Databases like the NIST X-ray Photoelectron Spectroscopy Database [33] offer a nearly complete index of chemical shifts for many compounds along with their corresponding references. The core concept is that any change in the electron attraction by the atomic nucleus or change in the valence band will affect the local state of the electron. This will therefore result in a change in the corresponding binding energy and/or peak shape [32]. Using high-resolution XPS on various polymers, researchers were able to identify the following effects, where the hybridization state of carbon induces a chemical shift, the electronegativity of first substituents has a major influence on chemical shift, and the electronegativity of secondary substituents also has an influence on chemical shift [32]. In the studies by Schmeisser et al. [34] the electronegativity of oxygen was attributed to an average 0.89 eV shift in silicon per oxide substituted and an average 0.85 eV shift in germanium. However, Himpsel et al. [35] showed that these chemical shifts can be influenced by the structure of the oxide, with dielectric screening from a thicker oxide reducing chemical shift compared to thinner amorphous oxides. No single theory has been developed that has succeeded in explaining more than general trends in binding energy variations [1]. Interpretation of chemical shifts is often accomplished on an empirical basis, where unknown binding energies are compared with measured binding energies of standard materials [1], such as the Ag $3d_{5/2}$ transition used in calibration of the SPECS instrument in section 2.3.

Binding energies by convention refer to the core-level energy relative to the spectrometer Fermi level [1]. For conducting samples in good electrical contact with the spectrometer, the Fermi levels of the sample and the spectrometer will be equivalent and absolute measurements of the binding energies can be made [1]. However in insulating samples absolute binding energy measurements are not possible and as a result an internal standard for reference must be used [1]. As adventitious carbon is observed on almost every as-received surface, the most widespread method is to use the C 1s binding energy of adventitious carbon (sp3 hybridized with C-C and C-H bonds) which has a well-known binding energy of 284.8 eV [28].

2.5   Data Processing and Peak Fitting

Quantitative analysis with XPS is complicated by the fact that the no-loss peak lineshapes are determined by a convolution of the X-ray photon energy distribution, the electron energy distribution in the ground state, the electron energy distribution in the photoionized state, lifetime broadening effects, electron energy loss structure, and the spectrometer energy resolution function [1]. Therefore, the intensity of a no-loss peak is more accurately accounted for by a peak area or energy probability distribution. The interpretation of XPS lineshapes must consider the intrinsic and extrinsic broadness of the XPS peak which is influenced by the above material and instrument factors [32]. The overall energy resolution ΔE, discussed in section 2.1, in XPS is given approximately by

$$\Delta E = (\Delta E_x^2 + \Delta E_A^2 + \Delta E_2^2)^{1/2} \qquad (11)$$

where ΔE_x is the FWHM of the X-ray line, ΔE_A is the proper absolute energy resolution of the analyzer operating in constant analyzer energy mode (CAE) which depends on the pass energy applied, and ΔE_2 is the natural line width of the orbital of the atom [32]. Equation 11 assumes

that all components have a perfect Gaussian (normal) statistical distribution, or lineshape [9]. This equation implies that the FWHM of XPS lineshapes will increase from narrowest to broadest by Al-Kα monochromated, Mg-Kα non-monochromated, to Al-Kα non-monochromated. Additionally, the analyzer FWHM will increase with higher pass energies. Care should be taken when comparing lineshapes between experimental observations and literature unless an identical source and resolution calibration procedure are used.

Actual XPS lineshape analysis is complicated by inelastic energy loss features including satellites and secondary electrons, and the fact that the line profile itself cannot be described by an analytical function [23]. Asymmetry in XPS signals can arise from several physical effects such as (i) a close overlap of several sub-signals due to the presence of different unresolved chemical states of one element, (ii) vibrational excitations during the photoionization of molecular species, and (iii) multi-electron excitations and the creation of electron-hole pairs in the valence band of metallic samples [23]. Through the research of Gelius [36] and Beamson & Briggs [37], asymmetry caused by the first two can be modeled by creating a sum of symmetric peaks. Gaussian functions include the transmission properties of the spectrometer and the lineshape of monochromatized X-rays, while Lorentzian functions represent the finite lifetime of the created core hole [23]. These lineshapes are convoluted with an idealized function representing the lineshape that would result using a perfectly monochromated source, a spectrometer with infinite resolution, and infinitely long core hole lifetimes to obtain the symmetric Voigt profile which has no analytical representation [23]. The lines are often approximated by Pseudo-Voigt functions, e.g. the product of a Gaussian and Lorentzian function or a weighted sum of the two curves [23]. The description of multielectron excitations in metal samples leading to asymmetry requires an advanced mathematical approach [23], summarized in

depth by Werner [38] and Werner & Schattschneider [39]. From many studies, the lineshapes of both germanium and silicon are expected to be symmetric, since they are both semiconductors, so in this analysis asymmetry can be attributed to a close overlap of several sub-signals and vibrational excitations during the photoionization of molecular species as described above.

With a mathematical description of the XPS lineshape selected based on expected behavior and prior literature, the spectra can be fit using peak fitting software like CasaXPS [40]. Because both the natural line widths of XPS signals and their chemical shifts are on the order of 1 eV, peak fitting is an essential part of XPS analysis [41]. However, peak fitting can be a highly subjective exercise [41]. A possible pitfall includes adding too many unconstrained peaks or other fit parameters without a reasonable chemical or physical basis [41]. Provided the function used to fit the lineshape, number of peaks included, and the location of them on the binding energy scale all have such a chemical or physical basis, a tremendous amount of information can be obtained.

Beamson & Briggs [37] described the underlying factors that influence no-loss lineshapes peak widths. Differences in vibrational degrees of freedom were used to explain the relative broadening of the $Si^{1+,}$ Si^{2+}, and Si^{3+} oxidation states in the Si/SiO_2 system [42]. Structural effects such as average bond angle disorder were also considered where FWHM increased as the structure becomes more disordered and amorphous [32]. These effects were identified in the Si/SiO_2 system where the FWHM of the Si 2p core level from a thin amorphous SiO_2 film was observed to be broadened with respect to the ordered crystalline oxide [42]. Citrin et al. [43] also identified phonon broadening and its increase with temperature arising from a difference between the before and after ionization states of electrons allowing for vibrational excitation. It

is important to note that the binding energy, lineshape, and FWHM for a single chemical identity can vary [32] so fitting parameters should be constrained when possible using literature values.

Other possible pitfalls of XPS peak fitting include using inappropriate backgrounds [41]. From Section 2.1, the background in the photoelectron energy distribution is composed of inelastically scattered and secondary electrons and is the background upon which the no loss peaks sit. The intensity used in quantitative analysis is the area under the appropriate peak only [27] so the background must be subtracted. For some peaks this is easy to do; however, with others shake-up, shake-off, and multiplet scattering can lead to features appearing over a wide energy range so the appropriate type of background subtraction must be used [27]. In the literature for Si 2p and Ge 3d core levels the most common background approximation is that of Shirley, where the background intensity at a point is determined, by an iterative analysis, to be proportional to the intensity of the total peak area above the background and to higher energy [27]. This method assumes that each electron in the characteristic peak is associated with a flat background of losses [27]. End points must also be chosen, but the precise position of the end points can be relaxed [27], or selected to achieve the best approximation of the background on either side of the no loss peak.

2.6   New Research and Experimental Techniques

This experimental review will begin with a summary of techniques used in single crystal solid/vapor interfaces, as these fundamental studies used techniques that largely formed the basis on which future experiments were built. Then more complex morphologies will be discussed, where APXPS spectra is often used in conjunction with other experimental methods to explain complex behavior. Finally, exemplary cases of APXPS studies will be discussed, including

spatial resolution in electrochemical reactions, solid/2-D layer interfaces, small molecule

intercalation in graphene, liquid/vapor interfaces, and solid/liquid interfaces.

The study of the interaction between gas molecules and a surface has significant

relevance in many real-world systems including catalysis, corrosion, geochemistry,

environmental, and atmospheric science [13]. APXPS provides direct information on surface

composition, including reactants, products, contaminants, and spectator species that might only

be present under a steady state of exchange with the gas phase [21]. Depending on the speed of

the reaction and the resolution/scan time of the instrument, kinetic information may be obtained

as well [13]. Single crystal surfaces provided a natural starting point for fundamental studies, due

to their well-defined periodic structures. Adsorption studies on single crystal surfaces have

provided information on site specific adsorption and occupation, new chemical phases formed on

surfaces upon exposure to gas, how changing surface orientation and defect density affects

adsorption and reaction pathways [44]. Studying CO adsorption on Pd(111), Kaichev et al. used

APXPS to differentiate between the different binding geometries of molecular CO on the surface

where the binding energy difference was 0.75 eV due to differences in coordination [45].

Studying the oxidation and reduction of Pd(111) in O_2, Ketteler et al. observed chemical shifts in

Pd 3d and O 1s at constant photon energy and varying temperature and pressure, and were able

to construct a phase diagram as oxidation progresses from surface oxide, subsurface oxide, to

bulk Pd oxide [46]. Growth of the bulk oxide PdO was monitored over time by comparing the

deconvoluted peak intensities for elemental Pd 3d. In addition, they acquired a depth profile of O

1s by changing the photon energy (i.e. the photoelectron kinetic energy) and thus the sampling

depth. Gunther et al. studied of adsorbate coverages and surface reactivity in methanol oxidation

over Cu(110), where the intensities of adsorption species were deconvoluted from O 1s and C 1s

spectra [47]. It was found that the deconvoluted spectra changed with substrate temperature and varying mixing ratios of methanol and oxygen and allowed the authors to explain the surface reaction mechanism [47]. Andersson et al. did a similar experiment to explain the quantitative partitioning of water between its molecular and dissociated forms on Cu(110) [48]. Researchers built upon these fundamental single crystal studies by expanding to more complex morphologies. Zhang et al. investigated surface modified carbon nanotubes for catalysis in the dehydrogenation of n-butane. Using APXPS at oxidative dehydrogenation conditions (butane:oxygen 1:1 at 0.25 mbar, T_{sample} = 350-375 °C), they compared relative intensities of ketonic and ether/hydroxyl components of the O 1s spectra to test the reaction selectivity [49]. Caballero et al. studied Ni nanoparticles deposited on CeO_2 to study the strong metal-support interaction which causes complete inhibition of hydrogen adsorption capacity by metallic Ni burial by oxide moieties [50]. Using APXPS and chemical shift analysis, they were able to show that partially oxidized Ni is reduced by hydrogen at 300°C, and upon further heating to 500°C the Ni intensity completely disappears supporting the burial hypothesis [50].

The distinct advantage of APXPS in studying electrochemical systems is the contactless measurement of local potentials across the different interfaces in the cell [15]. The working electrode is grounded to the APXPS analyzer, so the core level photoelectrons measured show a shift in kinetic energy that is related to the local potential, which serve as a basis for calculating overpotentials associated with individual cell components [15]. Zhang et al. investigated the solid-oxide electrochemical cell consisting of Au/CeO_{2-x} working electrodes and Pt counter electrodes on polycrystalline yttria-stabilized zirconia (YSZ) [51]. They utilized a new beamline at the Advanced Light Source with APXPS capabilities and a two dimensional detector that allows imaging of the electrochemically active region directly and provides spectra with a spatial

resolution of 20 μm in one direction [51]. In this manner they monitored the Ce 4d core level intensity and observed changes in the Ce^{+3}/Ce^{+4} (reduction/oxidation) ratios under different applied potentials [51].

Recently APXPS has been used for atomic mechanism studies of chemical vapor deposition of ultra-thin layers on solid substrates, with two studies focusing on mono and few layer graphene on Ni(111) [52], [53]. Comparing LEED patterns and XPS of pristine and defective graphene layers, along with C 1s chemical shifts of the different surface graphene conformations, the authors were able to identify competing atomistic mechanisms of graphene formation on Ni. Granas et al. exposed graphene on Ir(111) to CO in the mbar regime in an attempt to observe CO intercalation, a topic of interest as catalyst selectivity could be based on a molecules ability to intercalate past the graphene barrier [54]. In intercalation studies peak widths have been correlated to the height modulation of the graphene layer above the Ir(111) surface [54]. The C 1s deconvolution associated with intercalated CO is narrower than the C 1s for pristine graphene on Ir(111), which is attributed to decreased height modulation upon CO intercalation [54].

The liquid/vapor interface has been of interest since the early days of XPS, however the UHV requirement made observing most liquids nearly impossible with traditional XPS setups. Faubel et al. [55] demonstrated that photoelectron spectroscopy data from a liquid water jet can be obtained on a constantly refreshed surface. With the development of near-ambient and ambient pressure XPS, studies have been able to focus on higher vapor pressure liquids [15]. Studies have demonstrated that APXPS spectra can be obtained with a variety of creative liquid sample preparation methods including static drop, continuously wetted surface, and meniscus dip & pull [15]. Solid/liquid interfaces have also been studied by taking advantage of these

developments. Brown et al. [56] used a liquid jet to study colloidal SiO_2 nanoparticles in high pH aqueous solution. With high resolution spectra they proposed the outermost layer of the nanoparticles is composed of deprotonated silanol groups, which interacts with the solution while the core of the nanoparticles remain unaffected [56].

2.7   References

[1]   A. B. Christie, "X-ray photoelectron spectroscopy," in *Methods of Surface Analysis*, J. M. Walls, Ed. Cambridge, UK: Cambridge University Press, 1989, pp. 127–168.

[2]   K. W. Kolasinski, *Surface Science: Foundations of Catalysis and Nanoscience*, 3rd ed. New York, NY: John Wiley & Sons, Inc., 2012.

[3]   Y. F. Chen, C. M. Kwei, and C. J. Tung, "Electron inelastic mean free paths versus attenuation lengths in solids," *J. Phys. D. Appl. Phys.*, vol. 25, no. 2, pp. 262–268, 1992.

[4]   M. P. Seah and W. A. Dench, "Quantitative electron spectroscopy of surfaces: A standard data base for electron inelastic mean free paths in solids," *Surf. Interface Anal.*, vol. 1, no. 1, pp. 2–11, Feb. 1979.

[5]   J. H. Oh *et al.*, "Chemical structure of the ultrathin SiO_2/Si(100) interface: An angle-resolved Si 2p photoemission study," *Phys. Rev. B*, vol. 63, no. 20, p. 205310, 2001.

[6]   A. Jablonski, "Effects of Auger electron elastic scattering in quantitative AES," *Surf. Sci.*, vol. 188, no. 1–2, pp. 164–180, 1987.

[7]   M. P. Seah and S. J. Spencer, "Ultrathin SiO_2 on Si II . Issues in quantification of the oxide thickness," pp. 640–652, 2002.

[8]   P. J. Cumpson and M. P. Seah, "Elastic Scattering Corrections in AES and XPS. II. Estimating Attenuation Lengths and Conditions Required for their Valid Use in Overlayer/Substrate Experiments," *Surf. Interface Anal.*, vol. 25, no. 6, pp. 430–446, Jun. 1997.

[9]   D. Briggs and J. C. Riviere, "Spectral Interpretation," in *Practical Surface Analysis by Auger and X-ray Photoelectron Spectroscopy*, D. Briggs and M. P. Seah, Eds. New York, NY: John Wiley & Sons, Inc., 1983, pp. 87–139.

[10]   C. S. Fadley, "Basic Concepts of X-ray Photoelectron Spectroscopy," in *Electron Spectroscopy: Theory, Techniques, and Applications*, vol. 2, C. R. Brundle and A. D. Baker, Eds. New York, NY: Academic Press, 1978, pp. 1–155.

[11]   J. C. Riviere, "Instrumentation," in *Practical Surface Analysis by Auger and X-ray Photoelectron Spectroscopy*, D. Briggs and M. P. Seah, Eds. New York, NY: John Wiley & Sons, Inc., 1983, pp. 17–85.

[12]   F. Reniers and C. Tewell, "New improvements in energy and spatial (x, y, z) resolution in AES and XPS applications," *J. Electron Spectros. Relat. Phenomena*, vol. 142, no. 1, pp. 1–25, 2005.

[13]   A. R. Head and H. Bluhm, "Ambient Pressure X-Ray Photoelectron Spectroscopy," in *Reference Module in Chemistry, Molecular Sciences and Chemical Engineering*, vol. 27, no. 2, Elsevier, 2016, pp. 14–23.

[14]   E. Atanassova and A. Paskaleva, "Influence of the rapid thermal annealing in vacuum on the XPS characteristics of thin SiO_2," *Appl. Surf. Sci.*, vol. 103, no. 4, pp. 359–367, 1996.

[15] L. Trotochaud, A. R. Head, O. Karslioğlu, L. Kyhl, and H. Bluhm, "Ambient pressure photoelectron spectroscopy: Practical considerations and experimental frontiers," *J. Phys. Condens. Matter*, vol. 29, no. 5, p. 053002 2017.

[16] H. Siegbahn and K. Siegbahn, "ESCA applied to liquids," *J. Electron Spectros. Relat. Phenomena*, vol. 2, no. 3, pp. 319–325, Jan. 1973.

[17] M. A. Kelly, M. L. Shek, P. Pianetta, T. M. Gür, and M. R. Beasley, "In situ x-ray photoelectron spectroscopy for thin film synthesis monitoring," *J. Vac. Sci. Technol. A Vacuum, Surfaces, Film.*, vol. 19, no. 5, pp. 2127–2133, Sep. 2001.

[18] D. F. Ogletree, H. Bluhm, G. Lebedev, C. S. Fadley, Z. Hussain, and M. Salmeron, "A differentially pumped electrostatic lens system for photoemission studies in the millibar range," *Rev. Sci. Instrum.*, vol. 73, no. 11, p. 3872, 2002.

[19] H. Bluhm *et al.*, "Soft X-ray microscopy and spectroscopy at the molecular environmental science beamline at the Advanced Light Source," *J. Electron Spectros. Relat. Phenomena*, vol. 150, no. 2–3, pp. 86–104, Feb. 2006..

[20] H. Bluhm, "Photoelectron spectroscopy of surfaces under humid conditions," *J. Electron Spectros. Relat. Phenomena*, vol. 177, no. 2–3, pp. 71–84, 2010.

[21] M. Salmeron and R. Schlögl, "Ambient pressure photoelectron spectroscopy: A new tool for surface science and nanotechnology," *Surf. Sci. Rep.*, vol. 63, no. 4, pp. 169–199, 2008.

[22] M. T. Anthony, "Spectrometer Calibration," in *Practical Surface Analysis by Auger and X-ray Photoelectron Spectroscopy*, D. Briggs and M. P. Seah, Eds. New York, NY: John Wiley & Sons, Inc., 1983, pp. 429–435.

[23] M. Schmid, H. P. Steinrück, and J. M. Gottfried, "A new asymmetric Pseudo-Voigt function for more efficient fitting of XPS lines," *Surf. Interface Anal.*, vol. 46, no. 8, pp. 505–511, 2014.

[24] S. Hüfner, *Photoelectron Spectroscopy - Principles and Applications*, 3rd ed. Berlin Heidelberg: Springer-Verlag, 2010.

[25] S. M. Goldberg, C. S. Fadley, and S. Kono, "Photoionization cross-sections for atomic orbitals with random and fixed spatial orientation," *J. Electron Spectros. Relat. Phenomena*, vol. 21, no. 4, pp. 285–363, 1981.

[26] R. F. Reilman, A. Msezane, and S. T. Manson, "Relative intensities in photoelectron spectroscopy of atoms and molecules," *J. Electron Spectros. Relat. Phenomena*, vol. 8, no. 5, pp. 389–394, 1976.

[27] M. P. Seah, "Quantification of AES and XPS," in *Practical Surface Analysis by Auger and X-ray Photoelectron Spectroscopy*, D. Briggs and M. P. Seah, Eds. New York, NY: John Wiley & Sons, Inc., 1983, pp. 181–216.

[28] J. F. Moulder, W. F. Stickle, P. E. Sobol, and K. D. Bomben, *Handbook of X-Ray Photoelectron Spectroscopy*. Eden Prairie, MN: Perkin-Elmer Corporation, 1992.

[29]   V. Craciun, I. W. Boyd, B. Hutton, and D. Williams, "Characteristics of dielectric layers grown on Ge by low temperature vacuum ultraviolet-assisted oxidation," *Appl. Phys. Lett.*, vol. 75, no. 9, pp. 1261–1263, 1999.

[30]   M. Rossi *et al.*, "In situ observation of wet oxidation kinetics on Si(100) via ambient pressure x-ray photoemission spectroscopy," *J. Appl. Phys.*, vol. 103, no. 4, 2008.

[31]   C. S. Fadley, "Angle-resolved x-ray photoelectron spectroscopy," *Prog. Surf. Sci.*, vol. 16, no. 3, pp. 275–388, 1984.

[32]   B. Nisol and F. Reniers, "Challenges in the characterization of plasma polymers using XPS," *J. Electron Spectros. Relat. Phenomena*, vol. 200, pp. 311–331, 2015.

[33]   A. V. Naumkin, A. Kraut-Vass, S. Gaarenstroom, and C. J. Powell, "NIST X-ray Photoelectron Spectroscopy Database," 2012.

[34]   D. Schmeisser *et al.*, "Surface oxidation states of germanium," *Surf. Sci.*, vol. 172, no. 2, pp. 455–465, Jul. 1986.

[35]   F. J. Himpsel, F. R. McFeely, A. Taleb-Ibrahimi, J. A. Yarmoff, and G. Hollinger, "Microscopic structure of the SiO2/Si interface," *Phys. Rev. B*, vol. 38, no. 9, pp. 6084–6096, 1988.

[36]   U. Gelius, "Binding energies and chemical shifts in ESCA," *Phys. Scr.*, vol. 9, no. 3, pp. 133–147, 1974.

[37]   G. Beamson and D. Briggs, "High resolution monochromated x-ray photoelectron spectroscopy of organic polymers: A comparison between solid state data for organic polymers and gas phase data for small molecules," *Mol. Phys.*, vol. 76, no. 4, pp. 919–936, 1992.

[38]   W. S. M. Werner, "Electron transport in solids for quantitative surface analysis," *Surf. Interface Anal.*, vol. 31, no. 3, pp. 141–176, 2001.

[39]   W. S. M. Werner and P. Schattschneider, "On the energy dissipation process in incoherent electron scattering," *J. Electron Spectros. Relat. Phenomena*, vol. 143, no. 2–3 SPEC. ISS., pp. 65–80, 2005.

[40]   N. Fairley, "CasaXPS." Neal Fairley.

[41]   B. Singh, A. Diwan, V. Jain, A. Herrera-Gomez, J. Terry, and M. R. Linford, "Uniqueness plots: A simple graphical tool for identifying poor peak fits in X-ray photoelectron spectroscopy," *Appl. Surf. Sci.*, vol. 387, pp. 155–162, 2016.

[42]   P. J. Grunthaner, M. H. Hecht, F. J. Grunthaner, and N. M. Johnson, "The localization and crystallographic dependence of Si suboxide species at the SiO2/Si interface," *J. Appl. Phys.*, vol. 61, no. 2, pp. 629–638, 1987.

[43]   P. H. Citrin, P. Eisenberger, and D. R. Hamann, "Phonon broadening of x-ray photoemission linewidths," *Phys. Rev. Lett.*, vol. 33, no. 16, pp. 965–969, 1974.

[44]   D. E. Starr, Z. Liu, M. Hävecker, A. Knop-Gericke, and H. Bluhm, "Investigation of

solid/vapor interfaces using ambient pressure X-ray photoelectron spectroscopy," *Chem. Soc. Rev.*, vol. 42, no. 13, pp. 5833–5857, 2013.

[45]   V. V. Kaichev, I. P. Prosvirin, V. I. Bukhtiyarov, H. Unterhalt, G. Rupprechter, and H. J. Freund, "High-pressure studies of CO adsorption on Pd(111) by X-ray photoelectron spectroscopy and sum-frequency generation," *J. Phys. Chem. B*, vol. 107, no. 15, pp. 3522–3527, 2003.

[46]   G. Ketteler, D. F. Ogletree, H. Bluhm, H. Liu, E. L. D. Hebenstreit, and M. Salmeron, "In situ spectroscopic study of the oxidation and reduction of Pd(111)," *J. Am. Chem. Soc.*, vol. 127, no. 51, pp. 18269–18273, 2005.

[47]   S. Günther, L. Zhou, M. Hävecker, E. Kleimenov, R. Schlögl, and R. Imbihl, "Adsorbate coverages and surface reactivity in methanol oxidation over Cu(110): An in situ photoelectron spectroscopy study," vol. 114709, no. 110, 2017.

[48]   K. Andersson *et al.*, "Bridging the pressure gap in water and hydroxyl chemistry on metal surfaces: The Cu(110) case," *J. Phys. Chem. C*, vol. 111, no. 39, pp. 14493–14499, 2007.

[49]   J. Zhang, X. Liu, R. Blume, A. Zhang, R. Schlögl, and S. S. Dang, "Surface-modified carbon nanotubes catalyze oxidative dehydrogenation of n-butane," *Science*, vol. 322, no. 5898, pp. 73–77, 2008.

[50]   A. Caballero, J. P. Holgado, V. M. Gonzalez-Delacruz, S. E. Habas, T. Herranz, and M. Salmeron, "In situ spectroscopic detection of SMSI effect in a Ni/CeO$_2$ system: Hydrogen-induced burial and dig out of metallic nickel," *Chem. Commun.*, vol. 46, no. 7, pp. 1097–1099, 2010.

[51]   C. Zhang *et al.*, "Measuring fundamental properties in operating solid oxide electrochemical cells by using in situ X-ray photoelectron spectroscopy," *Nat. Mater.*, vol. 9, no. 11, pp. 944–949, 2010.

[52]   R. S. Weatherup *et al.*, "On the mechanisms of Ni-catalysed graphene chemical vapour deposition," *ChemPhysChem*, vol. 13, no. 10, pp. 2544–2549, 2012.

[53]   L. L. Patera *et al.*, "In situ observations of the atomistic mechanisms of Ni catalyzed low temperature graphene growth," *ACS Nano*, vol. 7, no. 9, pp. 7901–7912, 2013.

[54]   E. Graìšnäs *et al.*, "CO intercalation of graphene on Ir(111) in the millibar regime," *J. Phys. Chem. C*, vol. 117, no. 32, pp. 16438–16447, 2013.

[55]   M. Faubel, B. Steiner, and J. P. Toennies, "Photoelectron spectroscopy of liquid water, some alcohols, and pure nonane in free micro jets," *J. Chem. Phys.*, vol. 106, no. 22, pp. 9013–9031, 1997.

[56]   M. A. Brown *et al.*, "Electronic structure of sub-10 nm colloidal silica nanoparticles measured by in situ photoelectron spectroscopy at the aqueous-solid interface," *Phys. Chem. Chem. Phys.*, vol. 13, no. 28, pp. 12720–12723, 2011.

Chapter 3: Characterization of Oxide Growth on Silicon-Germanium Alloys with Ambient Pressure X-ray Photoelectron Spectroscopy

3.1   Brief Synopsis

Binary $Si_{1-x}Ge_x$ (or SiGe) alloy has attracted significant attention in integrated circuit design due to increasing demand for high speed and low power electronics. Band gap engineering by controlling the Ge content significantly improves the performance of Si-based devices [1]. Grading of substitutional Ge in the crystal lattice of Si in heterojunction bipolar transistor (HBT) base regions can provide an accelerating field in the direction of electron flow [2] due to the lower bandgap of Ge (0.67 eV) relative to Si (1.11 eV) [3]. Moreover, the 4.2% lattice parameter mismatch between Ge (5.657 Å) and Si (5.431 Å) allows control of strain in metal oxide semiconductor field effect transistor (MOSFET) channels [2]. When SiGe alloys are grown pseudomorphically on a Si(001) substrate, the in-plane lattice constant of the substrate is conserved throughout the alloy layer biaxially compressing the SiGe film [4]. Conduction band valleys drop in energy resulting in a monotonic reduction of the indirect bandgap with increasing Ge content [4]. Compressively strained SiGe(001) is one of the most promising candidates for p-type MOSFET (p-MOSFET) channel materials, thanks to its high hole mobility [5]. A critical step for p-MOSFET fabrication is to grow or deposit a high quality oxide for the gate, masking, and other device applications [1]. Silicon-germanium on insulator (SGOI) structures could provide lower leakage current and better electrostatic control of the channel representing a key milestone in enhancing performance of p-MOSFETs [5]. Despite their importance, it is difficult to grow high-quality oxides on SiGe films while at the same time limiting damage to the SiGe semiconductor [1].

Nanostructuring of SiGe by oxidation is an effective method for fabrication of a wide variety of SiGe-based electronic devices [6]. Tezuka et al. [7] describe the condensation technique, which can be used for the fabrication of unique structures. The process involves selective oxidation of Si in SiGe, causing Ge condensation into the bulk of the alloy [6] accompanied by the formation of a Si flux from the bulk alloy toward the oxidizing interface [8]. The gradient in the Si and Ge mole fractions drives the interdiffusion of Si and Ge [8], and the rate of diffusion determines the Ge concentration profile. Further processing involves thermal Ge concentration homogenization in the alloy [5], ideally resulting in a low-defect SiO_2 dielectric grown on a homogenized compressively strained SiGe alloy layer. Several things can go wrong during the fabrication process: Si is not selectively oxidized leading to mixed oxide formation and oxide thermal instability [9]; Ge condensation and germanium rich layer (GRL) formation leading to high oxide-alloy interface trap density [10]; Ge condensation and GRL formation causing strain dislocations which degrade the SiGe-Si substrate interface [11]; and complete strain relaxation of the alloy layer [1]. Chang et al. [9] identify that preferential oxidation of Si without GeO_x formation and no Ge pile-up at the interface as key requirements for the fabrication of SiGe devices. A deep understanding of the mechanisms and kinetics of SiGe thermal oxidation is thus required to develop optimized nanostructuring processes [1].

In spite of a recent renaissance in SiGe oxidation research since the early 1990s pioneered by LeGoues et al. [12], [13] there is still a lack of consensus regarding the oxidation kinetics of SiGe, especially early during the initial stage. It is generally agreed that due to the large difference in thermal stability between SiO_2 and GeO_2, oxygen atoms in GeO_2 can be taken up by adjacent Si atoms in a replacement reaction [14]. However, by calculating the free energy for the oxidation reaction of Si and the replacement reaction it can be shown that Si prefers to react with the oxidant

[8]. When the flux of diffused silicon is insufficient to react with the arriving oxidant flux, a mixed oxide will form. It has been observed that low temperature, high pressure, or high Ge concentration in the alloy can result in the Si flux being insufficient to react with the arriving oxidant molecules and thus lead to the co-oxidation of Ge and Si [8]. Chang et al. [9] hypothesize that Ge oxidation can be suppressed by keeping the oxygen chemical potential at the SiGe interface low. Moreover, they stated the interfacial oxide layer should be kept as thin as possible [9]. The interfacial region thickness is expected to vary with oxidation temperature from 1-2 monolayers (ML) (3-6 Å SiO_x) [15], with gate quality dielectric interfaces as thin as 0.8 ML possible at 530°C [10]. Song et al. demonstrated this could be done most effectively by reducing O_2 pressure at the SiGe surface [14].

It has been reported that diffusion of the oxidant in the oxide is rate limiting for SiGe oxides over 50 Å, and for dry thermal oxidation overall rates for SiGe are consistently higher than for pure Si under identical conditions [5]. A possible explanation for this is the strain influence on the oxide density, which effectively increases the O_2 diffusion rate in the oxide [5]. Currently there is no consensus on thin regime (< 50 Å) rate limiting steps. Tetelin et al. [16] observed no SiGe oxidation rate enhancement over Si in a molecular oxygen ambient, but a significantly enhanced SiGe rate in atomic oxygen. They attributed breaking of substrate bonds as the limiting mechanism for atomic oxygen, and dissociation of oxygen as the limiting mechanism for molecular oxygen [16]. However, Spadafora et al. [17] determined that the SiGe oxidation rate in dry molecular oxygen increases approximately linearly with increasing Ge concentration. It was proposed that this is due to the lower bond energy of Si-Ge compared to Si-Si [18]. They propose a unified description of dry and wet oxidation where the difference in Si-Si and Si-Ge bond energies and the role of point defects generated during oxidation can explain rate differences between Si and SiGe under all the conditions studied [17]. Rabie et al. [8] hypothesize that point defects is also

significant in increasing the oxidation rate of Ge in SiGe relative to pure Ge, as point defects serve to increase the interdiffusion of both Si and Ge. Depending on the oxidation conditions, the oxidation of Ge in SiGe can be suppressed relative to Si due to a hypothesized reaction where Si replaces Ge in GeO_2, resulting in the formation of SiO_2 via a two-step process that is faster than the direct oxidation of Si [8]. This reaction pathway occurs in both wet and dry oxidation processes [8].

Many studies on thin regime oxidation of SiGe have used X-ray photoelectron spectroscopy (XPS) due to its strength in collecting surface sensitive chemical state information [1], [5], [6], [10], [14], [19], [20]. These studies have been useful in analysis of the composition of the oxide, oxide thickness, and Ge/Si compositional profiles with angle resolved and sputter depth profile techniques. Real time measurements can provide direct information on the dynamics of all the oxidation states while the oxide growth is in progress [21]. However, due to the requirement of ultrahigh vacuum (UHV) or near-UHV for standard XPS, real time oxidation studies have been limited to oxygen pressure of 10^{-5} mbar [22]. In this pressure regime, oxidation of Si(001) almost stops at an oxide thickness of 4-6 Å which corresponds to just 1-2 ML of oxide [22]. With ambient pressure X-ray photoelectron spectroscopy (APXPS), Si 2p and Ge 3d core levels can be monitored during oxidation for much higher oxygen pressures where the oxide grows to thicknesses of practical interest.

This study seeks to yield insight into the initial stages of SiGe oxidation. The focus is understanding thin regime (< 50 Å) growth mechanisms for epitaxially grown $Si_{1-x}Ge_x$ films via dry thermal oxidation. We compare the results to Si(001) and Ge(001) for reference. These studies are performed using chemical state and time resolved ambient-pressure X-ray photoelectron spectroscopy (APXPS). The dynamics of Si and Ge oxidation states and how these dynamics are

affected by oxygen pressure are analyzed with the purpose of evaluating current theories on SiGe oxidation.

3.2   Experimental Details

As discussed in chapter 1, crystal faces can have different reactivity depending on the number and type of dangling bonds at the surface [23]. Thus, for a direct comparison between oxygen uptake on SiGe, Si, and Ge surfaces the crystal face must be consistent. Due to the effect of lattice strain on carrier mobility, SiGe(001) surfaces are of industrial interest. For these studies, an epitaxial layer of SiGe was deposited on Si(001). For comparison, polished crystalline Si(001) and Ge(001) samples were obtained. Samples were cleaved to sizes that fit in the Ta APXPS sample holders. SiGe(001) and Ge(001) samples were provided by Intel Corporation (Hillsboro, OR). Si(001) was obtained from Addison Engineering (San Jose, CA).

Prior to loading into the APXPS system, the samples were cleaned and the native oxide layers removed. Degreasing agents ACS grade acetone was obtained from Pharmco, and ACS electronic grade isopropyl alcohol (IPA) was obtained from Fischer Chemical. Wet-etch hydrogen peroxide solutions were prepared with ACS grade 30 wt% H_2O_2 solution obtained from Macron, and wet-etch hydrofluoric acid (HF) solutions were prepared with ACS grade 48-51 wt% HF solution obtained from VWR International. All samples were degreased with a 2 minute acetone ultrasonic bath, rinsed with IPA, and blown dry with nitrogen. The Si(001) and SiGe(001) samples were then cleaned with low temperature oxygen plasma in a PE50 Plasma Cleaner for 10 minutes to removed carbon surface impurities. For Ge(001), the O_2 plasma treatment resulted in significant oxide growth which was later difficult to remove. Thus for Ge(001) the O_2 plasma treatment was replaced with a sequential wet-etch which included a 2 minute dip in deionized water (18.2 MΩ cm) followed by a 30 second dip in 10 wt% H_2O_2. The final step for all samples was a hydrofluoric

acid wet-etch ("HF last") intended to passivate surfaces with hydrides removable by annealing. This was done by a 50:1 H_2O:HF (48-51 wt%) wet etch for 10 minutes, 12 minutes, and 10 minutes for SiGe(001), Si(001), and Ge(001) respectively. Surfaces were then blown dry with ultra-high purity nitrogen. Complete surface preparation procedures are summarized in Table 3.1 and 3.2 below.

Table 3.1: Summary of surface preparation procedures for Si(001) and SiGe(001).

	Degrease	Carbon removal	Wet-etch	Post-treatment
Si(001)	2 min acetone ultrasonic, IPA rinse, N_2 blow dry	10 min PE50 oxygen plasma etch	12 minute 50:1 H_2O:HF(49%)	N_2 blow dry
SiGe(001)	2 min acetone ultrasonic, IPA rinse, N_2 blow dry	10 min PE50 oxygen plasma etch	10 minute 50:1 H_2O:HF(49%)	N_2 blow dry

Table 3.2: Summary of surface preparation procedures for Ge(001).

	Degrease	Carbon removal	Wet-etch	Post-treatment
Ge(001)	2 min acetone ultrasonic, IPA rinse, N_2 blow dry	2 minute deionized water (18.2 MΩ cm), 30 second 10% H_2O_2	10 minute 50:1 H_2O:HF(49%)	N_2 blow dry, 300°C UHV anneal

Due to limitations on the stability of hydrogen terminated Si(001) and Ge(001) surfaces in ambient air [24], the samples were immediately loaded into XPS load locks and pumped down to 10^{-6} mbar within 5-8 minutes after wet-etching. Further annealing steps were limited by a 600°C upper temperature limit in the near-ambient pressure (NAP) cell of the APXPS instrument. It has been shown that contamination layers on Si(001) can be removed by annealing up to 1000°C, compared to much lower 300-500°C for Ge(001) [25]. However, GeO might desorb [9] at temperatures as

low as 450°C [26]. To avoid depositing GeO on the cone and elsewhere in the NAP cell, the highest anneal temperature was kept below 375°C. The Ge(001) surface had significantly higher contamination relative to Si(001) due to the tendency of GeH_x to react with hydrocarbons [27]. Thus, a 300°C anneal is included in the post-treatment procedure for Ge(001) to desorb weakly adsorbed contaminants. While these procedures will not produce oxygen and carbon free surfaces [28], the intent of this study is to replicate surfaces similar to what would be encountered using industrial manufacturing processes. Thus, a small amount of contamination is expected.

The surface chemical composition of the SiGe films was confirmed using a PHI 5600 XPS system. This system had a base pressure $< 2 \times 10^{-10}$ mbar. Pass energy for high resolution spectra was set to 23.5 eV. The instrument was calibrated using a sputter cleaned gold film and measuring the Au $4f_{7/2}$ core level (referenced at binding energy 83.98 eV [29] and natural linewidth 0.33 eV [30]). Both Al Kα and Mg Kα X-rays with photon energies of 1486.6 eV and 1253.6 eV, respectively, were used. Monochromatized Al-Kα X-rays were used for primary chemical analysis due its narrow linewidth to maximize resolution. The source to analyzer angle when using the monochromatized Al Kα radiation is 90°. At this photon energy, the Ge $L_3M_{23}M_{23}$ Auger peak overlaps with the O 1s core level peak making accurate O 1s intensity determination difficult. To overcome this, Mg Kα X-rays were used to analyze the O 1s peak. The source to analyzer angle when using Mg Kα X-rays is 54.7°. For compositional analysis instrument specific relative sensitivity factors (RSFs) were used [31].

Ambient pressure XPS measurements were performed using a custom built SPECS APXPS system with PHOIBOS concentric hemispherical analyzer. A monochromatized Al Kα X-ray source (hv = 1486.6 eV) was used with a NAP cell where the emission angle was 0° with respect to the surface normal. The source axis to analyzer axis angle on this instrument is 60°. The binding

energy scale was calibrated using a sputter cleaned silver film and measuring the Ag $3d_{5/2}$ core level (referenced at binding energy 368.27 eV [29], natural linewidth 0.28 eV [30]). High resolution spectra were obtained with a fixed pass energy of 35 eV. These spectra were obtained before and after each set of oxidation experiments (i.e. before introducing and after pumping out oxygen from the NAP cell). The overall experimental resolution in this case was 0.66 eV. Spectra obtained during the oxidation process were collected with a fixed pass energy of 50 eV. This facilitated a single spectrum scan in approximately 80 seconds. For these conditions, the overall experimental resolution was 0.81 eV. Spectra were charge corrected using the aliphatic C 1s binding energy at 284.8 eV [31].

High resolution Si 2p and/or Ge 3d with Ge $2p_{3/2}$, O 1s, and C 1s spectra were collected in UHV before and after annealing to observe surface changes with temperature. Once an acceptably clean surface was achieved, oxygen was introduced into the NAP cell using a manual leak valve and the pressure was kept constant (to the extent possible) during the experiment. SiGe(001) oxidation experiments were run at pressures from 0.1 to 10 mbar and temperatures from 100 to 300°C. These experiments were performed to the appropriate experimental conditions to observe early oxidation mechanisms for oxide growth below 50 Å. The spectral signal to noise ratio, speed at which the instrument can repeat scans with sufficient resolution, and total time of experiment were taken into consideration. To have reasonable count rates the maximum oxygen pressure was 1 mbar for these experiments. Based on individual high resolution spectra collection time and total time of experiment (on the order of hours not days), 300°C was selected as the oxidation temperature. Higher temperatures necessitated rapid scan times, achievable only by unacceptably low signal to noise ratios.

Due to similar photoelectron kinetic energy, and thus similar sampling depth, the Si 2p and Ge 3d core levels were used for Si and Ge oxidation comparisons. Spectra were analyzed using a Shirley background subtraction and each spectrum were deconvoluted into five doublets. These included elemental silicon 2p (Si^0), three intermediate oxidation states (Si^{+1}, Si^{+2}, Si^{+3}), and fully oxidized Si (Si^{+4}), and elemental germanium 3d (Ge^0), three intermediate oxidation states (Ge^{+1}, Ge^{+2}, Ge^{+3}), and fully oxidized Ge (Ge^{+4}). Each doublet was fit with a symmetric Gaussian-Lorentzian product GL(m) lineshape, where m = 0 is pure Gaussian and m = 100 is pure Lorentzian. The proportion of Gaussian to Lorentzian can be influenced by factors including, but not limited to, X-ray source and analyzer pass energy. Silicon Si 2p spin orbit splitting was set to 0.61 eV, and spin orbit branching ratio (Si $2p_{1/2}$ / Si $2p_{3/2}$) set constant to 0.5 [32]. Germanium Ge 3d spin orbit splitting was set to 0.58 eV, and spin orbit branching ratio (Ge $3d_{3/2}$ / Ge $3d_{5/2}$) set constant to 0.67 [33]. All oxide doublets were fit as pure Gaussians, as was done by Grunthaner et al. [34]. Silicon oxidation state chemical shifts from Himpsel et al. [15] were used as a starting point for Si 2p spectra fitting. The core level binding energy shifts from Si^0 were reported as 0.95, 1.75, 2.48, and 3.90 eV for Si^{+1} to Si^{+4}, respectively. Germanium oxidation state chemical shifts from Schmeisser et al. [35] were used as a starting point for Ge 3d spectra fitting. The core level binding energy shifts from Ge^0 were reported as 0.8, 1.8, 2.6, and 3.4 to 4.2 eV for Ge^{+1} to Ge^{+4}, respectively. During fitting procedures the 4+ oxidation state chemical shifts were not fixed, as they are expected to increase as the oxide grows for both SiO_2 [36] and GeO_2 [37]. Full width at half maximum (FWHM) of oxides were constrained to increase monotonically from elemental peak to fully oxidized peak, in accordance with increase in vibrational degrees of freedom with coordinated oxides [34]. For ease of visual comparison of Si 2p and Ge 3d suboxide relative

intensities in high resolution spectra, a Shirley background has been subtracted and Si $2p_{1/2}$ and Ge $3d_{3/2}$ contributions to the five peak spectral deconvolutions omitted.

The National Institute of Standards software Simulation of Electron Spectra for Surface Analysis (SESSA) has been used for quantification of the data. Spectrometer settings (photoelectron emission angle, acceptance angle, etc.) for SESSA models were matched to experimental settings. A value for the atomic density of each modeled layer is determined by the software. For elemental solids and for over 2500 inorganic compounds, this atomic density is queried from a database. The atomic density of a compound is estimated on the basis of the densities for each elemental constituent; these estimated densities may have uncertainties of more than 100% [38]. For this analysis, the atomic densities for pure Si (n_{Si}) and pure Ge (n_{Ge}) were set to 4.991×10^{22} and 4.415×10^{22} atoms cm^{-3}, respectively. These are derived from elemental mass densities 2.3277 and 5.3256 g cm^{-3} [39]. The atomic densities for amorphous SiO_2 (n_{SiO_2}) and amorphous GeO_2 (n_{GeO_2}) were set to 2.25×10^{22} atoms cm^{-3} [40] and 2.12×10^{22} atoms cm^{-3}, where n_{GeO_2} was derived from glassy GeO_2 mass density 3.677 g cm^{-3} [41].

3.3   Chemical Composition Determination and RSF Calibration

As discussed in Chapter 2, the intensity of a core level photoelectron peak is influenced by multiple kinetic energy dependent spectrometer terms that vary from instrument to instrument. Moreover, the differential photoelectron cross-section and attenuation length vary from material to material. When quantifying the relative intensities of peaks from two elements the ratio of these two quantities remains nearly constant. In quantitative chemical analysis, intensity ratios are used wherein these kinetic energy dependent terms can be grouped into instrument specific relative sensitivity factors (RSFs). For well-established and studied instruments like the PHI 5600, documented RSFs can be used directly for chemical analysis [31]. Using Al Kα X-rays with a

source to analyzer angle of 90° the RSFs for Ge $2p_{3/2}$, Ge 3d, Si 2p, C 1s, and O 1s core level transitions are 3.100, 0.408, 0.283, 0.296 and 0.711, respectively [31]. Comparing the RSFs for Ge $2p_{3/2}$ and Ge 3d which have a wide separation in kinetic energy, there is a large correction required to yield a 1:1 atomic ratio for an atomically clean surface.

High resolution scans of Ge $2p_{3/2}$, Ge 3d, Si 2p, C 1s, and O 1s core levels were collected at a fixed pass energy of 23.5 eV with the PHI 5600 instrument. Deconvolution of C 1s spectra involved fitting with as few Gaussian peaks as possible, which were near the expected binding energy for aliphatic carbon. This process of C 1s fitting was done only to ensure proper binding energy scale calibration; atomic percent calculations can be done by determining the whole peak intensity including high binding energy shoulders. To determine the fitting parameters for the Ge $L_3M_{23}M_{23}$ Auger peak Mg Kα X-rays were used to shift the Ge $L_3M_{23}M_{23}$ from the O 1s peak. The best fit for the Ge $L_3M_{23}M_{23}$ was obtained with Shirley background subtraction, pure Gaussian GL(0), binding energy of 300.7 eV, and FWHM of 3.5 eV. While the FWHM is expected to change with pass energy, for this analysis the fit was constrained to 3.5±0.2 eV. It should be noted that this subtraction method is only an estimation and introduces some uncertainty in the O 1s intensity.

Spectra deconvolution procedure for Si 2p and Ge 3d followed steps described above. Since the samples are expected to be clean, components for the higher oxidation states (3+, 4+) are included only to verify their absence. A detailed analysis of chemical shift will be discussed in section 4.4. Best fit for elemental Si^0 from Si 2p was achieved with GL(40), best fit for elemental Ge^0 from Ge 3d with GL(60), and for Ge^0 from Ge $2p_{3/2}$ with GL(80). An increasing Lorentzian contribution to the lineshape suggests core hole lifetime effects are increasingly dominant, or that the experimental resolution is increasingly close to photoemission natural linewidth [42]. For three replicate experiments, the Si 2p and Ge 3d elemental intensities were divided by their RSFs to

obtain a mean atomic density in the substrate. As previously stated, the kinetic energies of photoelectrons from these two elements is quite similar and thus are considered to have nearly identical sampling depths. SESSA estimated that the IMFPs (λ) are 3.08 nm for Si 2p from pure Si and 2.99 nm for Ge 3d from pure Ge. Assuming roughly similar λ for transport in the alloy of 3 nm, the sampling depth can be approximated as $\lambda\cos\theta$ [43] or about 2.1 nm at emission angle $\theta = 45°$ which is well into the bulk. At these experimental conditions, the $Si_{1-x}Ge_x(001)$ alloy mean germanium fraction was determined to be x = 0.40 ± 0.02. To check for the possibility of attenuation by a contamination overlayer affecting atomic density calculations, samples were Ar^+ ion sputtered in-situ with an Ar pressure $\sim 10^{-7}$ mbar, an acceleration voltage of 3 kV, and a current density of 0.15 mA cm^{-2} for 2 minutes. The post sputtered $Si_{1-x}Ge_x(001)$ alloy mean germanium fraction was determined to be x = 0.37 ± 0.02. Ge will be preferentially sputtered from the alloy as the sputtering yield of Ge is about 1.7 times that of Si [44], so this decrease in mean germanium fraction is not surprising. Taking the sputter yields to be 1.3 and 2.2 for Si and Ge [44], respectively and assuming the sputtering yield of the components is independent of their bulk composition, the surface composition is inversely proportional to the sputtering yields [45]

$$\frac{C_{s,Si}}{C_{s,Ge}} = \frac{S_{Ge}}{S_{Si}} \frac{C_{b,Si}}{C_{b,Ge}} \qquad (1)$$

where $C_{b,Si}$ is the bulk concentration of Si, $C_{b,Ge}$ is the bulk concentration of Ge, S_{Si} is the sputtering yield of Si, S_{Ge} is the sputtering yield of Ge, $C_{s,Si}$ is the surface concentration of Si, and $C_{s,Ge}$ is the surface concentration of Ge. Using this idealized expression, the steady-state surface Ge concentration is calculated to be x = 0.34, which is close to the post sputter XPS quantified Ge content suggesting minimal attenuation by the contamination overlayer.

With the chemical composition of the alloy determined with confidence, the PHI 5600 instrument RSFs were used to calibrate SPECS APXPS RSFs based on known atomic density

ratios. Comparing the asymmetry parameters between Si 2p and Ge 3d core levels, the difference is quite small (~0.7%) suggesting source to analyzer angle will not significantly affect their relative intensities. Recall from chapter 2 Figure 2.4 that Ge 3d photoelectron intensity from Ge(001) exhibits a complex dependence on emission angle. Si 2p photoelectron intensity from Si(001) exhibits a similar complex dependence on emission angle [36]. Caused by diffraction in the substrate, differences in Si 2p and Ge 3d relative intensity with emission angle could cause apparent changes in atomic percent. Emission angles of 0° and 45° appear to avoid such diffraction complexity [43], [36]. Thus, the SPECS Ge 3d RSF can be adjusted relative to Si 2p to match the expected Ge:Si ratio independent of emission angle. Ideally for a given instrument the Ge 3d and Ge $2p_{3/2}$ peak intensities along with appropriate RSFs would yield a 1:1 atomic ratio. However due to the large difference in asymmetry parameter between Ge 3d and Ge $2p_{3/2}$ core levels (~24% difference, compared with ~0.7% difference for Ge 3d and Si 2p), direction of the incident photons relative to photoelectron emission can cause deviations from ideality. To minimize this error, the source to analyzer angle was matched between the two instruments. Ge $2p_{3/2}$:Ge 3d atomic ratio obtained using the PHI 5600 instrument with Al Kα dual anode (α = 54.7°) with appropriate RSFs [31] was used to calibrate SPECS Al Kα mono (α = 60°) Ge $2p_{3/2}$ RSF relative to Ge 3d RSF. The O 1s and C 1s RSFs for the SPECS instrument were adjusted relative to Ge 3d (which has already been calibrated) to match their respective PHI 5600 ratios. This approach assumes the analyzer correction for these transitions relative to Ge 3d is identical between the instruments. While this is likely not exactly true, it is an approximation that should yield close values. The SPECS calibrated RSFs can be found in Table 3.3 below.

Table 3.3: Calibrated relative sensitivity factors (RSFs) for SPECS instrument compared to PHI 5600 values from literature.

Instrument	Ge 2p$_{3/2}$	Ge 3d	Si 2p	C 1s	O 1s
PHI 5600	3.100	0.408	0.283	0.296	0.711
SPECS	3.440	0.378	0.283	0.274	0.659

With a total of 10 experiments using the SPECS instrument the $Si_{1-x}Ge_x$ germanium content of the alloy in UHV at room temperature was determined to be x = 0.39 ± 0.01. It should be noted that the SPECS RSFs have been calibrated under the assumption that the Ge:Si atomic ratio calculated using Ge 3d and Si 2p elemental peak intensities and PHI 5600 RSFs for Al Kα monochromatized X-rays is accurate.

3.4   Characterization of "Time Zero" $Si_{0.60}Ge_{0.40}$(001), Si(001), and Ge(001) Surfaces

To fully understand oxide growth, $Si_{0.60}Ge_{0.40}$(001), Si(001), and Ge(001) surfaces before exposure to oxygen must be characterized. High resolution scans of Si 2p, Ge 3d, Ge 2p$_{3/2}$, and C 1s core levels at a fixed pass energy of 35 eV were taken in the APXPS NAP cell. Figure 3.3 shows the Si 2p core level spectra from $Si_{0.60}Ge_{0.40}$(001) and Si(001) surfaces after surface preparation procedures and annealing to 300°C in UHV. Elemental Si 2p from an atomically clean Si(001) surface is expected to have a symmetric lineshape, however the spectra in Figure 3.3 have an asymmetric high binding energy shoulder for both $Si_{0.60}Ge_{0.40}$(001) and Si(001). This asymmetry is caused by the presence of SiO_x suboxides with chemical shifts from the Si^0 binding energy [15]. Using high resolution XPS, Grunthaner et al. showed that the Si/ SiO2 interface was spectroscopically different after different surface preparations [46]. More specifically, they noted that the interfacial layer width thickness and chemistry are determined by the process. In Figure 3.3 the spectral shapes after surface preparation described previously and after annealing are nearly identical between the surfaces, suggesting similar interfacial Si suboxide chemistry. Averaged over

all measurements, the Si 2p$_{3/2}$ core level from Si$_{0.60}$Ge$_{0.40}$(001) and Si(001) both occur at 99.6 ± 0.1 eV. While in Figure 3.1 the Si 2p$_{3/2}$ core level from Si$_{0.60}$Ge$_{0.40}$(001) is approximately 0.06 eV higher, this small shift is within experimental error for the Si 2p$_{3/2}$ binding energy. From literature there is a distribution of binding energies for Si 2p from pure Si(001) ranging from 99.4 eV [47] to 99.8 eV [48]. For Si 2p from Si$_{1-x}$Ge$_x$(001) the values range from 99.4 eV [24] to 99.9 eV [1] where the binding energy relative to pure Si is hypothesized to be dependent, in part, on the fraction of Ge in the alloy [49], [50].
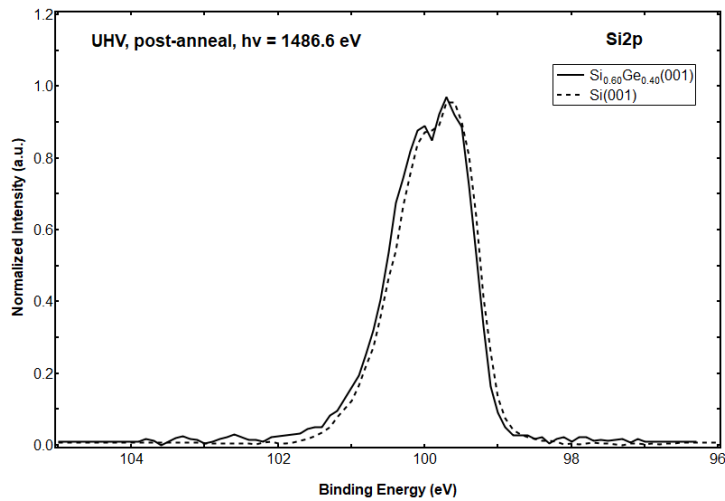
Figure 3.1: High resolution XPS spectra of the Si 2p core level from Si$_{0.60}$Ge$_{0.40}$(001) and Si(001) after surface preparation procedures and annealing to 300°C in UHV. In this spectra, the Si 2p$_{3/2}$ binding energy from Si$_{0.60}$Ge$_{0.40}$(001) is centered at 99.67 eV, while for Si(001) the binding energy is shifted 0.06 eV lower in energy at 99.61 eV.

Lucovsky and Agarwal suggest that increasing the Ge concentration in the alloy results in an increase in the binding energy for Si 2p, where the maximum shift in binding energy was +0.4 eV for alloy Ge concentrations up to 80% or higher [49], [50]. No alloy binding energy shift is observed Figure 3.1. Lucovsky and Agarwal also suggest the Si 2p shift to higher binding energy is accompanied by a commensurate Ge 3d shift to lower binding energy [49], [50]. Figure 3.2

shows the Ge 3d core level spectra from $Si_{0.60}Ge_{0.40}(001)$ and Ge(001) surfaces after surface preparation procedures and annealing to 300°C in UHV.
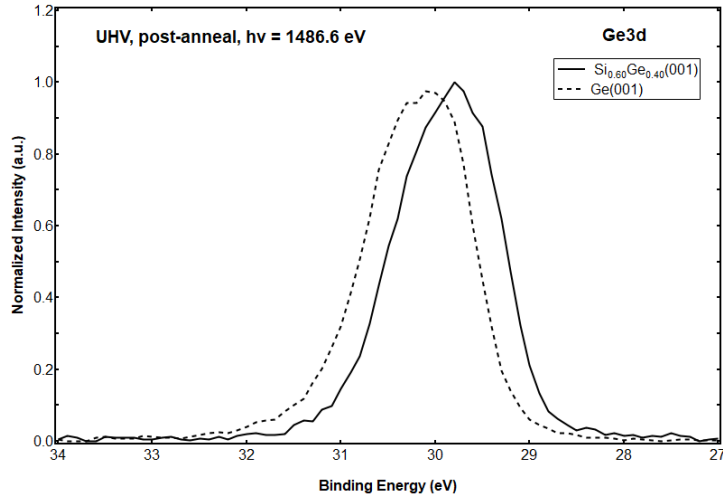
Figure 3.2: High resolution XPS spectra of the Ge 3d core level from $Si_{0.60}Ge_{0.40}(001)$ and Ge(001) after surface preparation procedures and annealing to 300°C in UHV. In this spectra, the Ge $3d_{5/2}$ binding energy from $Si_{0.60}Ge_{0.40}(001)$ is centered at 29.6 eV, while for Ge(001) the binding energy is shifted 0.3 eV higher in energy at 29.9 eV.

Averaged over all measurements, the Ge $3d_{5/2}$ core level from $Si_{0.60}Ge_{0.40}(001)$ occurs at 29.5 ± 0.1 eV while for Ge(001) it is shifted 0.4 eV higher at 29.9 eV. From literature there is a distribution of binding energies for Ge 3d from pure Ge(001) ranging from 29.3 eV [51] to 29.8 eV [33]. For Ge 3d from $Si_{1-x}Ge_x(001)$ the values range from 29.4 eV [51] to 29.9 eV [10] where the binding energy shift was correlated to the relative germanium concentration in the alloy. In agreement with literature, a shift to lower binding energy is observed for Ge 3d from $Si_{0.60}Ge_{0.40}(001)$ relative to pure Ge(001). However, no alloy shift observed in the Si 2p core level in Figure 3.1. The Ge(001) Ge 3d binding energy of 29.9 eV is on the high side of values reported in literature. It is suspected that band bending due to the presence of Ge(001) surface suboxides is the cause for the difference in $Si_{0.60}Ge_{0.40}(001)$ and Ge(001) Ge 3d core level binding energy, not alloy effects. Elemental Ge

3d from atomically clean Ge(001) is also expected to have a symmetric lineshape, however the spectra in Figure 3.2 have an asymmetric high binding energy shoulder for both $Si_{0.60}Ge_{0.40}(001)$ and Ge(001). This asymmetry is caused by the presence of GeO_x suboxides with chemical shifts from the Ge^0 binding energy [35]. The spectral shapes are again nearly identical between the surfaces, suggesting similar interfacial Ge suboxide chemistry.

After preparation of each surface according to the procedures described in Tables 3.1 and 3.2, it was desirable to quantify the contamination coverage on each surface to compare the effectiveness of each treatment. Figure 3.3 shows the expected binding energy region of the C 1s core level from adventitious carbon contamination on $Si_{0.60}Ge_{0.40}(001)$, Si(001), and Ge(001) surfaces after surface preparation procedures and annealing to 300°C in UHV.
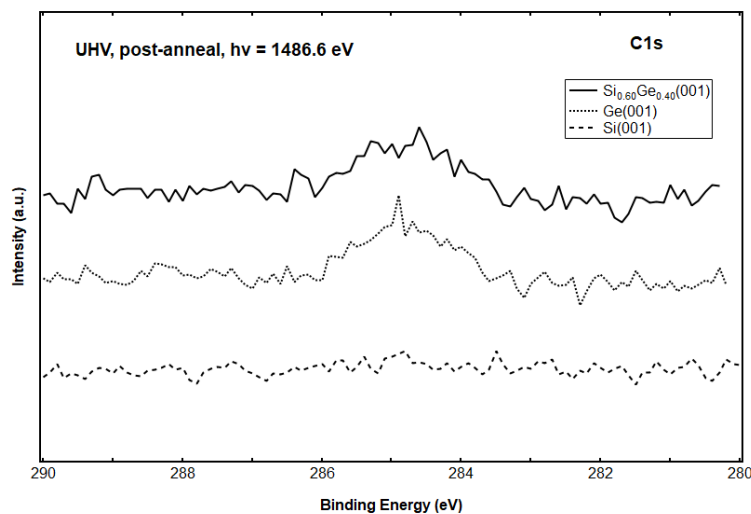
Figure 3.3: High resolution XPS spectra of the C 1s core level from adventitious carbon contamination on $Si_{0.60}Ge_{0.40}(001)$, Ge(001), and Si(001) surfaces after surface preparation procedures and annealing to 300°C in UHV. Spectra have been offset for visual comparison.

From Figure 3.3 it is apparent that surface preparation procedure was most effective for Si(001). Due to instability of GeH_x bonds relative to SiH_x bonds, surfaces containing Ge quickly take up carbon from the air. This is reflected in the C 1s peak at 284.8 eV corresponding to aliphatic carbon

in the spectra from $Si_{0.60}Ge_{0.40}(001)$ and Ge(001). It is somewhat surprising that the two surfaces have very similar C 1s intensities, considering a much higher GeH_x bond density at the Ge(001) surface and thus more places for carbon to absorb. This may suggest the reactivity of Ge at the $Si_{0.60}Ge_{0.40}(001)$ surface destabilizes SiH_x bonds as well.

Contamination coverage at time zero was quantified using a non-attenuating overlayer at fractional monolayer coverage model [52], adapted for the alloy by considering the photoelectron intensity from both Si and Ge in the substrate. Differential cross-sections were calculated using Si 2p, Ge 3d, O 1s, and C 1s total cross section and asymmetry parameters obtained from Goldberg et al. [53]. Attenuation lengths (L) for Si 2p and Ge 3d photoelectrons from $Si_{0.60}Ge_{0.40}(001)$ were adjusted from SESSA λ values using steps described by Cumpson et al. [54]. The values are 2.53 and 2.64 nm for Si 2p and Ge 3d photoelectrons, respectively. These can be compared with the L of Si 2p from pure Si (2.76 nm) and Ge 3d from pure Ge (2.47 nm), also obtained from SESSA using the atomic densities mentioned in section 3.2. Mean surface density of SiGe(001) is calculated to be 6.78×10^{14} atoms cm^{-2} [10]. Pre and post anneal C 1s and O 1s contamination at fractional monolayer coverages corresponding to the data shown in Figures 3.1, 3.2, and 3.3 can be found in Table 3.4 below.

Table 3.4: Quantified contamination calculated using non-attenuating overlayer at fractional monolayer (ML) coverage model. Si(001), Ge(001), and $Si_{0.60}Ge_{0.40}(001)$ surfaces coverages are compared before and after 300°C anneal in UHV.

Surface	Pre-Anneal (ML)		Post-Anneal (ML)	
	C 1s	O 1s	C 1s	O 1s
Si(001)	0.55	0.39	0.40	0.29
Ge(001)	>>1	1.2	1.4	0.47

Si$_{0.60}$Ge$_{0.40}$(001)	0.74	0.39	1.1	0.35

The data in Table 3.4. support conclusions from literature that GeH$_x$ bonds are unstable in air and will quickly chemisorb a monolayer of organic material [27]. This is indicated by C 1s monolayer coverages of 1 or higher for Si$_{0.60}$Ge$_{0.40}$(001) and Ge(001). It is believed that this one ML is chemisorbed to the surface with additional layers physisorbed that should be easily removed by annealing. For Ge(001) the carbon coverage has values over 1 ML prior to anneal and are reduced to ≈1 ML after. For Si$_{0.60}$Ge$_{0.40}$(001) annealing increases the carbon coverage slightly, suggesting some carbon may have been implanted during layer epitaxy which then diffuses to the surface upon annealing. In the literature, Ge(001) surface have been Cl-terminated to increase stability in air [55] and annealed to high temperature (~500°C) [26] to decompose and desorb surface contamination. However, GeCl$_2$ can desorb at temperatures as low as 150°C [56] and GeO would desorb during oxide thermal decomposition. To prevent depositing GeCl$_2$ or GeO in the NAP cell, these methods were avoided. Clean Si$_{0.60}$Ge$_{0.40}$(001) surfaces have been prepared via in-situ atomic hydrogen bake above 330°C [24] and subsequent anneal to 550°C or H$_2$ bake at 800°C [57]. Due to strain relaxation concerns and temperature limitations on the instrument, neither was attempted. The difference in C 1s coverage between Si(001) and Si$_{0.60}$Ge$_{0.40}$(001) is significant and should be taken into consideration if depressed oxidation rates are observed for Si$_{0.60}$Ge$_{0.40}$(001). The 25% difference in the O 1s coverage between Ge(001) and Si$_{0.60}$Ge$_{0.40}$(001) is not apparent in the Ge 3d core level spectra in Figure 3.2. Figure 3.4 shows the Ge 2p$_{3/2}$ core level spectra from Si$_{0.60}$Ge$_{0.40}$(001) and Ge(001) surfaces after surface preparation procedures and annealing to 300°C in UHV.
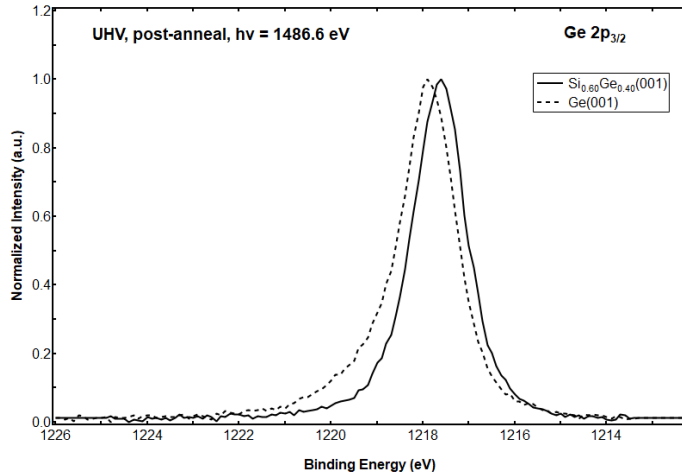
Figure 3.4: High resolution XPS spectra of the Ge $2p_{3/2}$ core level from $Si_{0.60}Ge_{0.40}(001)$ and $Ge(001)$ after surface preparation procedures and annealing to 300°C in UHV. In this spectra, the Ge $2p_{3/2}$ binding energy from $Si_{0.60}Ge_{0.40}(001)$ is centered at 1217.6 eV, while for $Ge(001)$ the binding energy is shifted 0.3 eV higher in energy at 1217.9 eV.

The Ge $2p_{3/2}$ spectra from $Ge(001)$ has an asymmetric tail suggesting higher oxidation states are present at the interface when compared to $Si_{0.60}Ge_{0.40}(001)$. As with the Ge 3d spectra, $Ge(001)$ is shifted to 0.3 eV high binding energy due to band bending. While a difference in interfacial suboxides is apparent between the two surfaces, the chemical shift of the high binding energy components are significantly lower than the $\Delta\varepsilon = 3.4$ to 4.2 eV range for GeO_2 [35]. This fine difference in interfacial suboxides is not expected to significantly impact oxide growth.

3.5   Observing Pressure Dependence of SiGe(001) Oxide Time Evolution

High resolution scans at with a pass energy of 35 eV were obtained in UHV after ~170 min at $T_{ox} = 300$°C and with $P_{O2} = 1$ mbar and 0.01 mbar. Si 2p and Ge 3d core-levels were used to monitor the oxidation of $Si_{0.60}Ge_{0.40}(001)$ alloy as the peaks have similar kinetic energy, which minimizes complications due to differences in sampling depth and analyzer transmission. Figures 3.5(a) and 3.5(b) show $P_{O2} = 1$ mbar height normalized data of the Si 2p and Ge 3d core levels,

respectively, which are fit with a deconvolution that includes five doublets corresponding to elemental (Si^0, Ge^0) and four oxidation states (1+, 2+, 3+, 4+). A Shirley background has been subtracted and Si $2p_{1/2}$ and Ge $3d_{3/2}$ contributions to the five peak spectral deconvolutions are omitted for figure clarity. The Si 2p spectra in Figure 3.5(a) is defined by two major peaks corresponding to elemental Si^0 at binding energy 99.3 eV (FWHM = 0.80 eV) and fully oxidized Si^{4+} (SiO_2) at 103.2 eV (FWHM = 1.4 eV). The chemical shift $\Delta\varepsilon$ = 3.8 eV for the well-developed oxide, while shifts as low as 3.5 eV were observed for the early stages of oxidation. This is likely due to a smaller valence band offset and extra screening by the substrate [12]. Peaks corresponding to expected suboxides Si^{1+} (Si_2O), Si^{2+} (SiO), and Si^{3+} (Si_2O_3) were included in fitting procedure with best fit obtained for $\Delta\varepsilon$ = 1.0, 1.8 and 2.6 eV, respectively. These chemical shifts are in agreement with literature [58]. For our studies, no Si^{2+} oxidation state was observed. Prior studies suggest that Si^{2+} is expected during the oxidation of $Si_{1-x}Ge_x$(001) surfaces [19]. As such, we believe that our experimental conditions may lead to a low concentration of Si^{2+}. The spectra shown in the inset for Figure 3.5(a) is the Si 2p "time zero" scan, taken after annealing to 300°C and prior to introducing oxygen into the NAP cell. Only the Si^0 and Si^{+1} oxidation states are observed, which corresponds to small amounts of absorbed contamination after surface preparation.
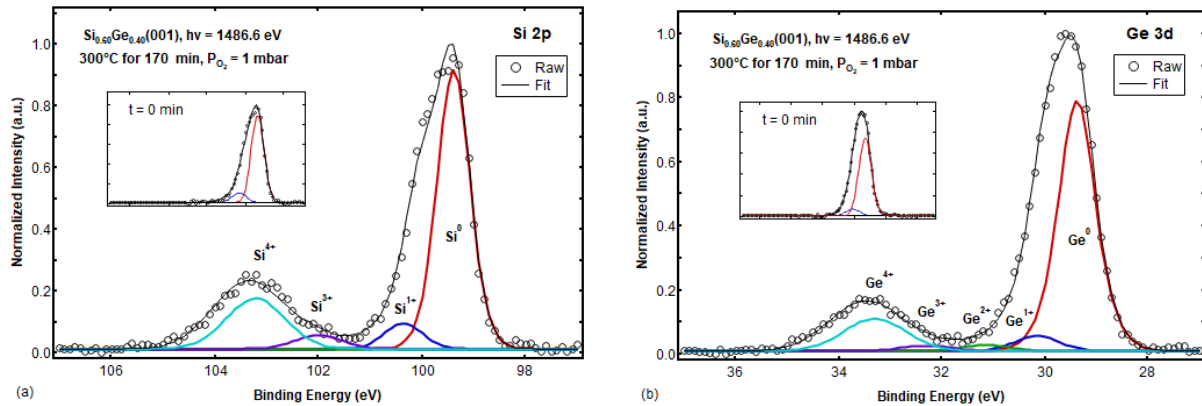
Figure 3.5: High resolution XPS spectra of the (a) Si 2p and (b) Ge 3d core levels from $Si_{0.60}Ge_{0.40}(001)$ after ~170 minutes of oxidation at 1 mbar, 300°C. Inset were was collected just prior to introducing oxygen into the chamber. Spectra were fit using five doublets corresponding to elemental and four oxidation states. A Shirley background has been subtracted and Si $2p_{1/2}$ and Ge $3d_{3/2}$ contributions to the five peak spectral deconvolutions are omitted.

The Ge 3d spectra is Figure 3.5(b) is also defined by two major peaks, which corresponding to elemental Ge^0 at binding energy 29.4 eV (FWHM = 0.95 eV) and fully oxidized Ge^{4+} (GeO_2) at 33.3 eV (FWHM = 1.7 eV) . The chemical shift $\Delta\varepsilon = 3.9$ eV was determined for the well-developed oxide, while shifts as low as 3.7 eV were observed for the early stages of oxidation. Matsui et al. explained this increase in GeO_2 chemical shift with oxide thickness through analogy to the Si/SiO_2 system, via final state effects and charge trapping in the oxide [37]. Peaks corresponding to expected suboxides Ge^{1+} (Ge_2O), Ge^{2+} (GeO), and Ge^{3+} (Ge_2O_3) were included in the fitting procedure with best fits obtained with $\Delta\varepsilon = 0.8$, 1.8 and 2.9 eV, respectively. While the chemical shifts for Ge^{1+} and Ge^{2+} are in agreement with literature, the values are high for Ge^{3+} and Ge^{4+} [59]. Zhang et al. noted increased chemical shifts in pure Ge due to charging during the XPS experiment [59]. While surface strained states have been fit as elemental high binding energy shoulders [32], no strain shift in oxide binding energy has been reported. Consequently, the high

chemical shifts for Ge^{3+} and Ge^{4+} are attributed to charging in the mixed oxide. The inset time zero spectra in Figure 3.5(b) indicates the presence of both Ge^{0} and the Ge^{1+} oxidation state, which is due to absorbed contamination. Comparing Figure 3.5(a) and 3.5(b), the Si^{1+} and Ge^{1+} oxidation states are prevalent at the $Si_{0.60}Ge_{0.40}(001)$ interface after surface preparation. Moreover, the 1+ oxidation state intensity to elemental intensity ratios are approximately the same suggesting the contamination is evenly distributed on the surface. Most models of the Si(001) surface suggests a larger proportion of interfacial Si^{2+} oxidation state [15], [32]. However, both the Si(001) and Ge(001) surfaces can reconstruct to a lower energy dimer surface [60]. This reconstruction leaves only two dangling binds per dimer or a 1+ oxidation state dominant surface. Ohdomari et al. also proposed a pseudo-model of a rough Si(001) surface where pyramid like protrusions with (111) facets lead to a predominance of the 1+ oxidation state [61]. One of these surface reconfigurations may be responsible for the 1+ oxidation state predominance at the $Si_{0.60}Ge_{0.40}(001)$ interface.

Figures 3.6(a) and 3.6(b) show Si 2p and Ge 3d spectra obtained after 170 min of oxidation at 300°C and with $P_{O2} = 0.01$ mbar. The spectra are height normalized and are fit with the same deconvolution and subtraction procedure as for Figure 3.5. Constraints on chemical shifts and FWHM of oxides developed from $P_{O2} = 1$ mbar were applied to fitting $P_{O2} = 0.01$ mbar spectra which yielded chi square values close to unity. Comparing Figure 3.6(a) with Figure 3.5(a), we find that the relative intensities of the five deconvolution peaks are similar indicating decreasing oxygen pressure by two orders of magnitude has a weak effect on oxidation of silicon in $Si_{0.60}Ge_{0.40}(001)$ alloy.
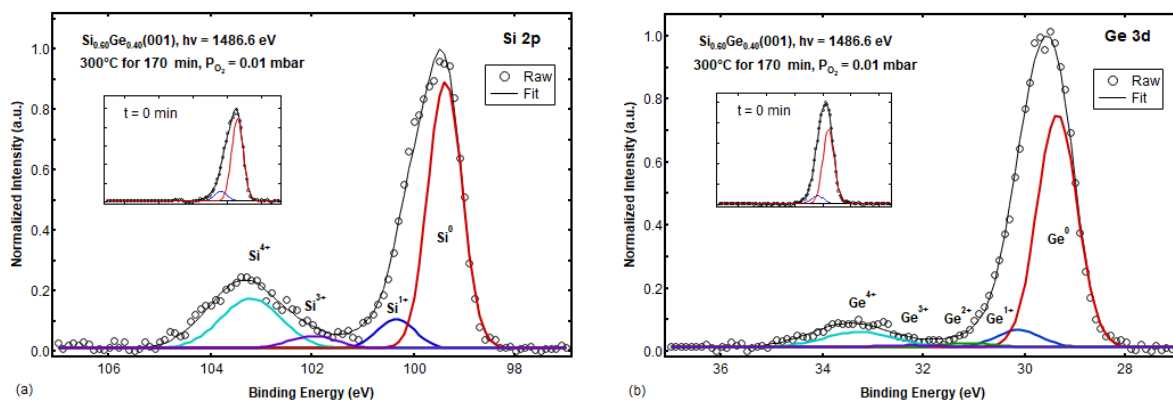
Figure 3.6: High resolution XPS spectra of the (a) Si 2p and (b) Ge 3d core levels from $Si_{0.60}Ge_{0.40}(001)$ after ~170 minutes of oxidation at 0.01 mbar, 300°C. Inset were collected just prior to introducing oxygen into the chamber. Spectra were fit using five doublets corresponding to elemental and four oxidation states. A Shirley background has been subtracted and Si $2p_{1/2}$ and Ge $3d_{3/2}$ contributions to the five peak spectral deconvolutions are omitted.

Comparing Figure 3.6(b) to Figure 3.5(b) indicates that the decreasing oxygen pressure has a strong effect on oxidation of Ge in $Si_{0.60}Ge_{0.40}(001)$ alloy. The difference is particularly pronounced in the Ge^{4+} to Ge^0 relative intensity ratio, which suggests that the formation of GeO_2 is strongly inhibited by decreasing oxygen pressure from 1 mbar to 0.01 mbar. Again, inset time zero spectra in Figure 3.6(a) and 3.6(b) suggest the presence of small amounts of absorbed contamination, which are indicated by the components with +1 oxidation state. Spectra fitting parameters were verified with four replicate experiments each for P_{O2} = 1 mbar and 0.01 mbar, with two each monitoring Si 2p uptake and Ge 3d uptake.

To evaluate the contamination coverage during oxidation, we estimated the fractional monolayer coverages for P_{O2} = 1 mbar and P_{O2} = 0.01 mbar experiments. The analysis procedure was identical to the surface contamination coverage calculation performed in section 4.4. Post-anneal coverages are estimated to be 1.0 ML C and 0.41 ML O for the P_{O2} = 1 mbar experiment

from which the spectra in Figure 3.5 were obtained, and 1.1 ML C and 0.35 ML O for the P_{O2} = 0.01 mbar experiment from which the spectra in Figure 3.6 were obtained. These contamination coverages suggest that the observed decrease in GeO$_2$ formation at P_{O2} = 0.01 mbar is not due to differences in surface cleanliness. Averaged over all P_{O2} = 1 mbar measurements, the contamination overlayer at fractional monolayer coverage is estimated to be 1.1 ± 0.10 ML C and 0.47 ± 0.08 ML O. For P_{O2} = 0.01 mbar, the average contamination coverage is estimated be 0.94 ± 0.13 ML C and 0.46 ± 0.12 ML O. The error associated with ML coverage serves as an indicator of the repeatability of the Si$_{0.60}$Ge$_{0.40}$(001) surface preparation procedure. The low error suggests our surface preparation procedure is repeatable with no significant difference in time zero contamination coverages between the pressure experiments.

Relative intensity ratios are useful for the analysis of APXPS data [21]. Intensity ratios help reduce uncertainty especially due to differences in instrumental effects and attenuation by ambient gas. These values are kinetic energy dependent and can cancel out for photoelectrons with close kinetic energies (i.e. Si^0 and Si^{4+}). The oxide to elemental intensity ratios ($I_{Si^{x+}}$ / I_{Si^0} and $I_{Ge^{x+}}$ / I_{Ge^0}) can then be used to accurately quantify oxide growth in real-time. For this analysis it is also assumed that Si 2p and Ge 3d photoelectrons are sufficiently close in kinetic energy so that their sampling depths are approximately the same. Sampling depth can be approximated as d = $\lambda\cos\theta$ [43]. By this equation, for a take-off angle of 0° relative to the surface normal, the sampling depth is equal to IMFP (in Si$_{0.60}$Ge$_{0.40}$(001) alloy λ_{Si2p} = 2.93 nm and λ_{Ge3d} = 3.05 nm, where the difference is less than the alloy atomic layer mean separation). To monitor the initial oxygen uptake during which the oxide growth is expected to be rapid, experiments were designed where we repeatedly scanned either the Si 2p or Ge 3d core levels as quickly as possible. For our system, an optimal time of approximately 80 seconds was achieved with a pass energy of 50 eV, a step size

of 0.1 eV, and dwell time of 700 millisecond per step. While sacrificing resolution compared to a 35 eV pass energy, we can still readily resolve the elemental and fully oxidized peaks.

Figure 3.7 shows the I_{Si4+} / I_{Si0} and I_{Ge4+} / I_{Ge0} ratios obtained from the Si 2p and Ge 3d spectra, respectively, versus time for $T_{ox} = 300°C$ and $P_{O2} = 1$ mbar and 0.01 mbar. Comparing the I_{Si4+} / I_{Si0} and I_{Ge4+} / I_{Ge0} ratios for data taken at $P_{O2} = 1$ mbar it is apparent Si is preferentially oxidized compared to Ge at all times. The same trend is true at $P_{O2} = 0.01$ mbar. This behavior is in good agreement with initial observations from Figures 3.5 and 3.6, and can be explained by the thermodynamic instability of GeO_2 relative to SiO_2 causing oxygen to preferentially react with silicon at the surface [62].
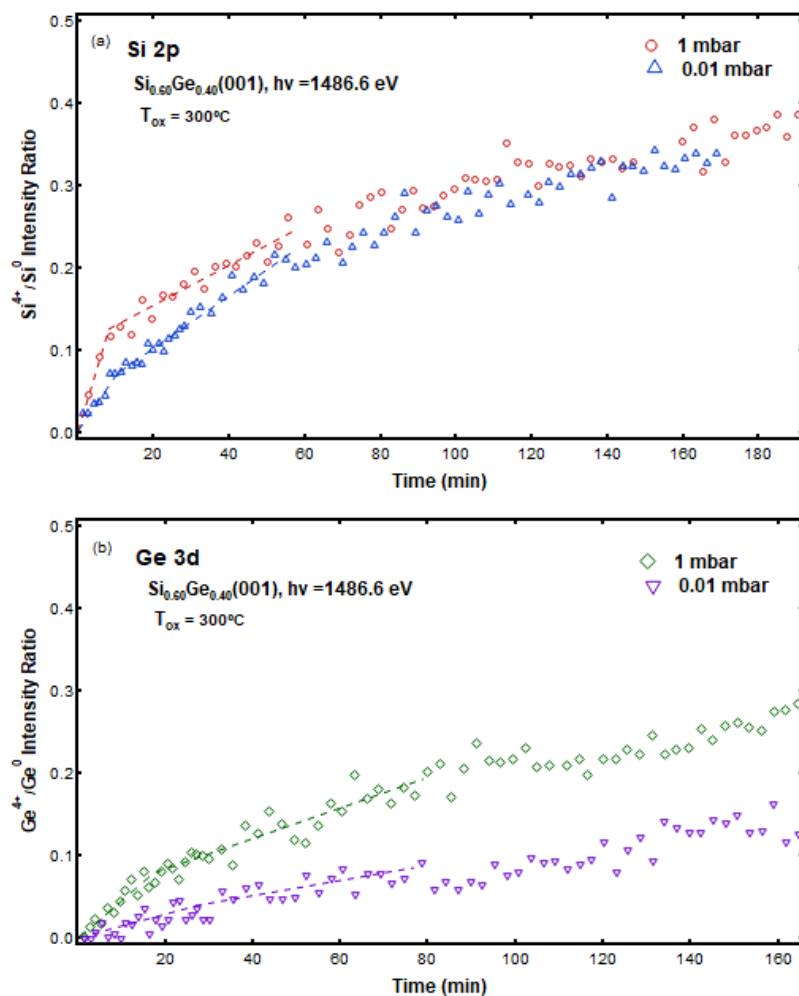
Figure 3.7: Time evolution of the oxide growth rate as measured by (a) the ratio of I_{Si4+} / I_{Si0} intensities and (b) the ratio of I_{Ge4+} / I_{Ge0} intensities at an oxidation temperature of 300°C and oxygen pressures of 0.01 and 1 mbar. Dotted lines overlaid on data points have been included to guide the eye. Early during the oxidation two distinct oxidation rate regimes are observed, rapid and transitionary.

The results in Figure 3.7 suggests that oxidation of Ge is more sensitive to changes in pressure than Si. At long oxidation times (>80 min) the I_{Si4+} / I_{Si0} intensity ratio, and rate of change of the ratio or oxidation rate, is nearly identical for P_{O_2} = 1 mbar and 0.01 mbar suggesting the oxidation of Si in $Si_{0.60}Ge_{0.40}(001)$ alloy is weakly dependent on pressure. However, Ge shows a strong dependence of I_{Ge4+} / I_{Ge0} on oxygen pressure. This suggests that while oxidation of Ge in $Si_{0.60}Ge_{0.40}(001)$ alloy is strongly dependent on pressure, the limiting mechanism at long oxidation times is identical at P_{O_2} = 1 mbar and 0.01 mbar. In fact at long oxidation times it appears the oxidation rate of Si and Ge is nearly identical, and that differences in intensity ratio at any given time are be attributable to processes early in oxidation. These findings support the hypothesis by Song et al. [14] that Si prefers to react with oxygen at the expense of the replacement reaction until some critical pressure, after which the oxidation rates between silicon and germanium should diverge. Evaluating short oxidation times (< 80 min), we find that the oxidation processes become more complex due to differences in the reacting element and gas pressure. Figures 3.7(a) and 3.7(b) suggest three oxide growth rate regimes: a rapid rate regime very early in oxidation, a slow rate quasi-saturated regime at long oxidation times, and a transition regime with a rate intermediate. The rapid and transitionary regimes have been marked by dotted lines in Figure 3.7 to guide the eye. It is generally agreed that the oxidation reaction is limiting in the very thin oxide (< 25 Å) regime, due to either breaking of Si-Ge bonds [17] or O_2 dissociation [16]. From Figure 3.7 it is clear that in the rapid regime (< 20 min), the oxidation rate of Si is higher than for Ge at both P_{O_2} = 1 mbar and 0.01 mbar. Moreover for both Si and Ge, the rapid regime oxidation rate is higher at P_{O_2} = 1 mbar and 0.01 mbar. This change in oxidation rate with pressure in the rapid regime (very thin oxide) should not happen if breaking of Si-Ge bonds is rate limiting. Chang et al. [9] proposed oxidation of Ge could be suppressed

by minimization of O_2 chemical potential. Thus oxidation of Ge should decrease with decreasing oxygen partial pressure [14]. The results in figure 3.7(b) for the early regime Ge oxidation supports this hypothesis. The data in Figure 3.7(a) suggests that early regime Si oxidation may also be suppressed by decreasing oxygen partial pressure, but to a lesser degree than Ge. Mastail et al. published a comparative DFT study on the oxidation of Si(001), Ge(001), and SiGe(001) 2x1 reconstructed surfaces [63]. They suggest that Si and Ge have distinctly different initial stage oxidation pathways, with the oxygen molecule adapting to the Si surface topology via predominantly dissociative configurations and the Ge surface adapting to the oxygen species to allow peroxy-bridge configurations. The Ge lattice deformation costs energy, resulting in higher energy structures [63] and preferential oxidation of Si. Importantly, they hypothesize that oxygen atoms seem to avoid the close neighborhood of Ge atoms and prefer to incorporate into the Si-Si bond. This may explain Ge rapid regime oxidation rate dependence on pressure, as decreasing pressure reduces the likelihood that oxygen will be available to react via the less energetically favorable pathway (with a Ge neighbor). As the Si oxidation mechanism is dissociative, a lowered oxygen chemical potential at the interface via lower oxygen pressure would slow kinetics. Oxygen pressure would affect the Si and Ge pathways differently. As diffusion of oxygen in the oxide is not rate limiting in the rapid regime, it may be that at both 1 mbar and 0.01 mbar an excess of oxygen is available at the surface to react by the most favorable pathway (with Si) leading to reaction with Ge, but as pressure decreases the unfavorable reaction with Ge becomes much less likely.

From Figure 3.7, it appears that a transition to a different limiting step occurs for both Si and Ge after the initial rapid oxidation regime. Deal-Grove suggests that diffusion of oxygen in the SiO_2 is oxidation reaction rate-limiting for thick oxides (> 250 Å) [64]. The same has been proven to be true for SiGe alloys [12]. For our results these transitions begin too early during the oxidation process. That is, the grown oxide is still very thin, and the transition is unrelated to a diffusion limited mechanism. It is clear from Figure 3.7(a) that the oxidation rate at times greater than 70 minutes, in the slow regime, is nearly identical for Si at both pressures. Considering Figure 3.7(b), the slow regime oxidation rate of Ge also

appears to be independent of pressure. In fact the oxidation rates of Si and Ge in the slow regime appear to be similar. This behavior suggest that in the transition regime, where the oxide is still relatively thin, the limiting mechanism possibly begins to shift from dissociation of oxygen to breaking of substrate Si-Ge bonds at some critical oxide thickness.

To investigate the nature of interfacial suboxide states and how they change with time, suboxide intensity ratios $I_{Si^{x+}}$ / I_{Si^0} and $I_{Ge^{x+}}$ / I_{Ge^0} were plotted with $I_{Si^{4+}}$ / I_{Si^0} and $I_{Ge^{4+}}$ / I_{Ge^0} ratios to monitor their change in time. The quality of the alloy/oxide interface plays an important role in device processing, as gate quality dielectric have few imperfections in their chemical structure to minimize interface traps [65]. SiO_2/Si(001) suboxide interfaces can be made as thin as 0.6 ML with dry oxygen processing at 900°C [10]. Similarly abrupt suboxide distributions have been observed at the SiO_2/SiGe(001) interface for ozone/atomic oxygen assisted oxidation at 530°C [10]. However, in general it has been observed that the alloy will tend to have a higher suboxide concentration and thus thicker interface when compared to pure Si in part due to surface roughening by preferential Si oxidation [19]. It is expected that factors such as surface preparation can significantly influence the density of suboxide states [46]. For the Si/SiO_2 system, Himpsel et al. found that that variations in pressure (10^{-5} to 10^1 mbar) and temperature (700 to 1100°C) do not affect the distribution of oxidation states significantly for oxides up to 30 Å thick [15]. They found the transition layer to be about two layers of Si atoms thick, which corresponds to 3 Å of pure Si or to 6 Å of SiO_2 [15]. Figure 3.8 shows the time evolution of Si 2p and Ge 3d oxidation states on $Si_{0.60}Ge_{0.40}$(001) at (a,b) P_{O2} = 1 mbar and (c,d) P_{O2} = 0.01 mbar with T_{ox} = 300°C.
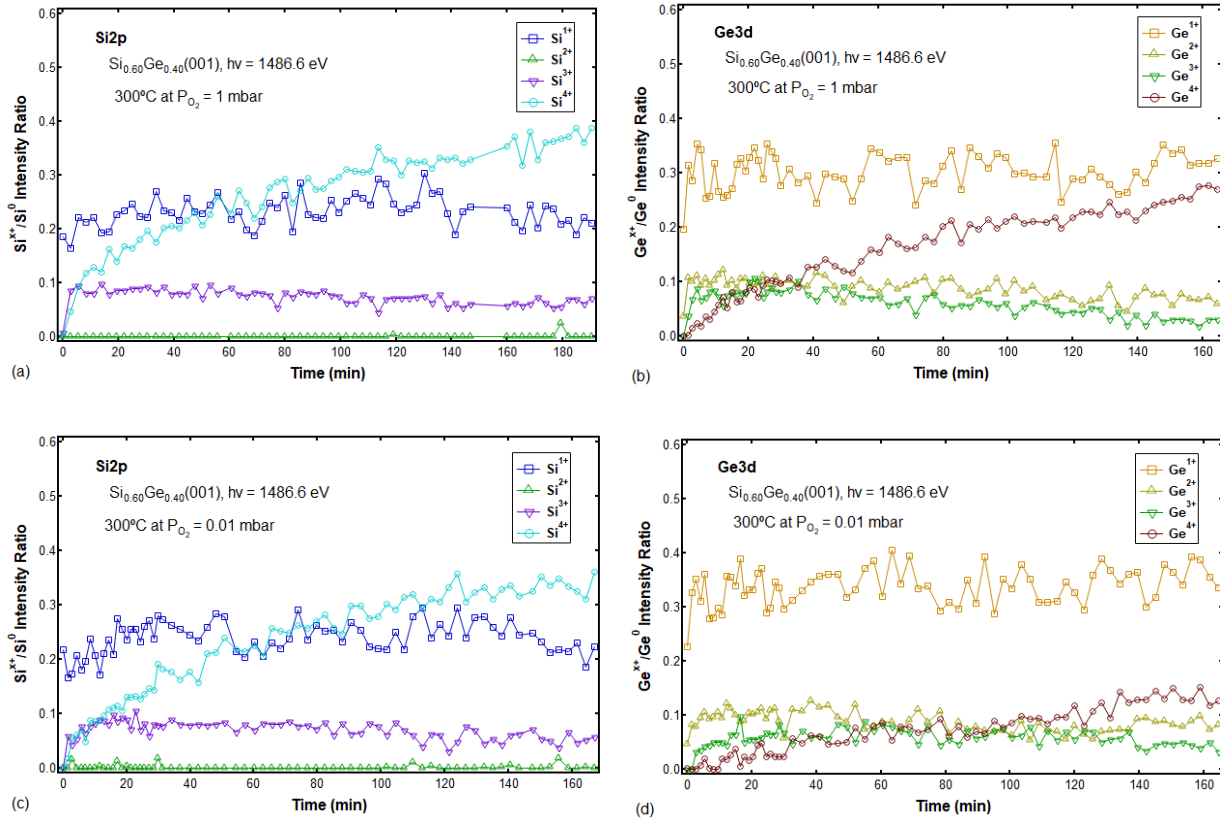
Figure 3.8: Time evolution of oxide growth rates on $Si_{0.60}Ge_{0.40}(001)$ alloy as measured by the intensity ratios $I_{Si^{x+}}/I_{Si0}$ and $I_{Ge^{x+}}/I_{Ge0}$ at 300° with oxygen pressure 1 mbar (a, b) and oxygen pressure 0.01 mbar (b, c).

For $Si_{0.60}Ge_{0.40}(001)$ dry oxidation at 300°C and P_{O2} = 1 and 0.01 mbar, the rapid regime formation of the Si^{4+} oxidation state appears to be associated with rapid Si^{3+} formation and possibly Ge^{3+} as well. For Ge, rapid growth of the Ge^{4+} oxidation state is accompanied by rapid growth of Ge^{2+} and Ge^{3+} oxidation states. The breakover point, when the rapid regime Si^{4+} formation rate begins to slow from its very high rate within the first 10 minutes of oxidation, is observed to be correlated to a breakover in rate of formation of Si^{3+} and Ge^{3+}. For both Si and Ge, the formation rate of the fully oxidized 4+ state is directly connected to the formation rate of its 3+ oxidation state. A decrease in pressure strongly affects formation of Ge^{3+} and Ge^{4+}, with the affect much weaker for

Si. The magnitude of the Si^{4+} and Si^{3+} intensity ratios at the time of breakover is observed to be pressure dependent with the breakover occurring at a lower Si^{4+} intensity ratio at 0.01 mbar compared to 1 mbar. The growth rate of Ge^{4+} intensity ratio is observed to be correlated to Ge^{3+} formation, with decreasing pressure causing a sharp decline in formation of both while leaving Ge^{2+} formation relatively unaffected. Pressure seems to have little effect on 1+ and 2+ interfacial suboxide states for both Si and Ge, suggesting that the quality of the interface is not changed when reducing oxygen pressure from 1 mbar to 0.01 mbar. These findings are similar to the behavior for the Si/SiO_2 system described by Himpsel et al. [15]. For both Si and Ge, as the oxide grows the intensity of the Si^{3+}, Ge^{3+}, and Ge^{2+} suboxide intensity ratios are observed to decrease. This lends supports that these suboxides are primarily interfacial as their intensity would tend to decrease as associated photoelectrons are attenuated by the growing oxide. While noise associated with deconvolution of the 1+ oxidation state and its proximity to the elemental peak makes determining the trend difficult, it appears that for both Si and Ge the 1+ oxidation state intensity ratio decreases as the oxide becomes thick (high 4+ ratio). In the slow regime, time evolution of the Ge^{3+} and Ge^{4+} ratios are similar to Si^{4+} and Si^{3+}, with no depression of Ge rates relative to Si to indicate a replacement reaction. This supports data from Song et al. [14] who suggest that at 300° a much lower pressure would be required for the replacement reaction to be the preferred mechanism over Si direct reaction with the oxidant. To summarize, it is observed that for $Si_{0.60}Ge_{0.40}(001)$ dry oxidation at 300°C that decreasing oxygen pressure primarily affects formation of the 3+ and 4+ oxidation states in the rapid regime for both Si and Ge. If the 1+ and 2+ suboxide intensity ratios are taken to be related to interface thickness, it is observed that decreasing oxygen pressure does not significantly affect interface thickness or the relative ratios of the suboxides.

3.6   Comparing Si(001), Ge(001), and SiGe(001) Oxide Time Evolution

High resolution spectra obtained with a fixed pass energy of 35 eV were taken in UHV after ~170 min at T_{ox} = 300°C and oxygen pressure of P_{O2} = 1 mbar. The Si 2p core level from Si(001) and Ge 3d core level from Ge(001) were used to observe the chemical state of oxides at the surface for comparison to Figure 3.5. Figure 3.9(a) and 3.9(b) show height normalized Si 2p and Ge 3d core levels, respectively, which are fit with a deconvolution into five doublets corresponding to elemental (Si^0, Ge^0) and four oxidation states (1+, 2+, 3+, 4+). A Shirley background has been subtracted and Si $2p_{1/2}$ and Ge $3d_{3/2}$ contributions to the five peak spectral deconvolution are omitted.
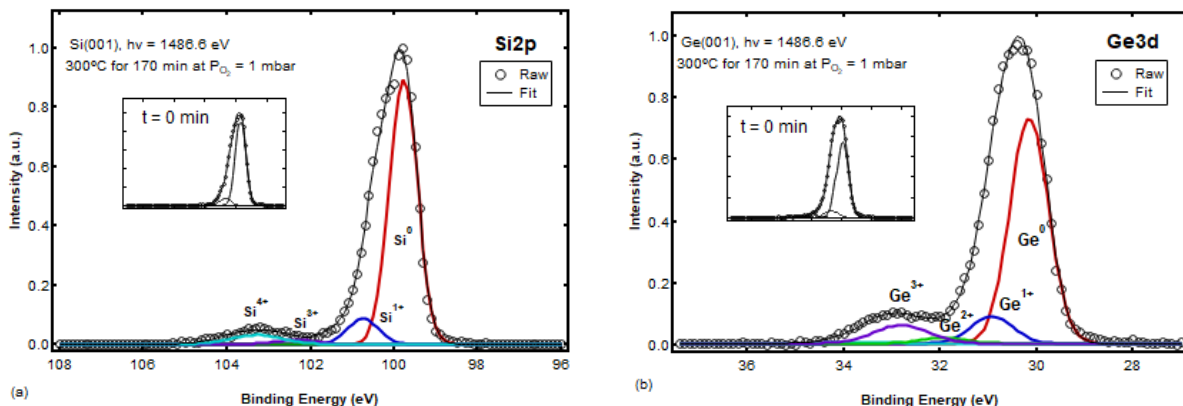
Figure 3.9: High resolution XPS spectra of the (a) Si 2p core level from Si(001) and (b) Ge 3d core level from Ge(001) after ~170 minutes of oxidation at 1 mbar, 300°C. Inset images were collected just prior to introducing oxygen into the chamber. Spectra were fit using five doublets corresponding to elemental and four oxidation states. A Shirley background has been subtracted and Si $2p_{1/2}$ and Ge $3d_{3/2}$ contributions to the five peak spectral deconvolutions are omitted.

The Si 2p spectra in Figure 3.9(a) is defined by two major peaks corresponding to elemental Si^0 at binding energy 99.6 eV (FWHM = 0.79 eV) and fully oxidized Si^{4+} (SiO_2) at 103.1 eV (FWHM = 1.4 eV). The $\Delta\varepsilon$ = 3.5 eV, which as stated in section 3.5 is on the low end of literature values for chemical shifts [66]. This is to be expected as the oxide is undeveloped compared to Figure 3.7(a).

Peaks corresponding to suboxides Si^{1+} (Si_2O), Si^{2+} (SiO), and Si^{3+} (Si_2O_3) were fit with $\Delta\varepsilon = 1.0$, 1.8 and 2.6 eV, respectively. The spectra in Figure 3.9(b) is defined by two major peaks, corresponding to elemental Ge^0 at binding energy 29.9 eV (FWHM = 0.94 eV) and fully oxidized Ge^{4+} (GeO_2) at 33.4 eV (FWHM = 1.5 eV) . The $\Delta\varepsilon = 3.5$ eV, which is significantly lower than chemical shift observed for the alloy oxide in our experiments ($\Delta\varepsilon = 3.9$ eV). Peaks corresponding to expected suboxides Ge^{1+} (Ge_2O), Ge^{2+} (GeO), and Ge^{3+} (Ge_2O_3) were fit with $\Delta\varepsilon = 0.8$, 1.8 and 2.7 eV, respectively. These values for chemical shift agree well with literature [59].

To better understand $Si_{0.60}Ge_{0.40}$(001) dry oxidation uptake mechanism, it was desirable to compare alloy oxidation to both pure Si(001) and Ge(001). Three experiments were performed for Si(001) and Ge(001) each at $T_{ox} = 300°C$ and $P_{O2} = 1$ mbar in order to directly compare to the $Si_{0.60}Ge_{0.40}$(001) data. Figure 3.10 shows time resolved high resolution Si 2p and Ge 3d XPS data collected during the rapid oxidation regime for $Si_{0.60}Ge_{0.40}$(001) oxide growth. Figure 3.10(a) is the Si 2p transition from Si(001); Figure 3.10(b) is the Si 2p transition from $Si_{0.60}Ge_{0.40}$(001). Figure 3.10(c) is the Ge 3d transition from Ge(001); Figure 3.10(d) is the Ge 3d transition from $Si_{0.60}Ge_{0.40}$(001).
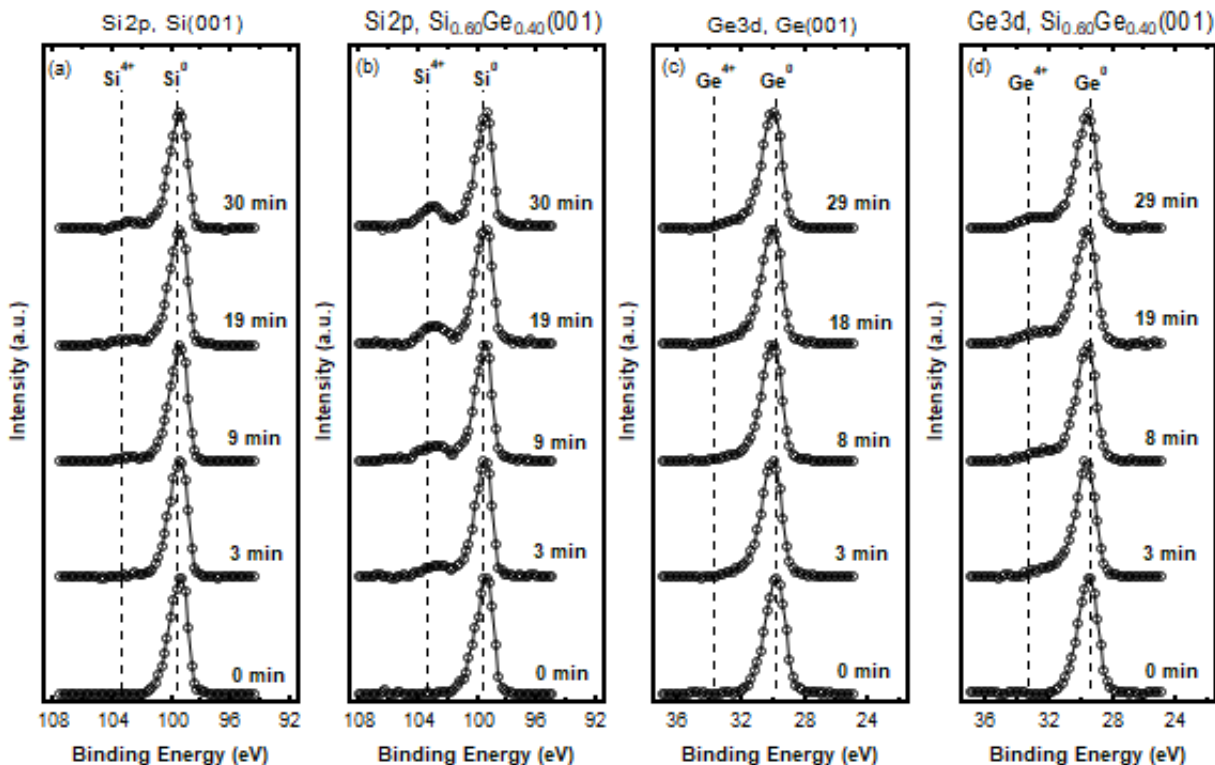
Figure 3.10: Time evolution of oxidation states at 300°C and 1 mbar oxygen pressure by high binding energy shoulder development as observed from (a) Si 2p from Si(001), (b) Si 2p from $Si_{0.60}Ge_{0.40}(001)$, (c) Ge 3d from Ge(001), and (d) Ge 3d from $Si_{0.60}Ge_{0.40}(001)$. Dotted lines mark the expected locations of elemental (Si^0, Ge^0) and fully oxidized (Si^{4+}, Ge^{4+}) peaks.

For reference the expected binding energies of the elemental states (Si^0 and Ge^0) and fully oxidized (Si^{4+} and Ge^{4+}) are indicated by dotted lines. From Figure 3.10 it is clear that the rapid regime growth rate of the 4+ oxidation state of both Si and Ge in the alloy is faster compared to pure Si(001) and Ge(001). For Si 2p this growth rate enhancement is clearly more pronounced, with a fully developed peak at the 4+ oxidation state binding energy after 30 minutes of exposure to 1 mbar dry oxygen ambient. It is expected that pure Si(001) will oxidize more readily than pure Ge(001), and this is reflected in Figure 3.10. From Figure 3.10(c) it appears that no GeO_2 has formed within 30 minutes. Figure 3.11 shows the time evolution of the Ge^{4+} for a full +170

minutes, comparing (a) $Si_{0.60}Ge_{0.40}(001)$ to $Si(001)$ and (b) $Si_{0.60}Ge_{0.40}(001)$ to $Ge(001)$ at 300°C and 1 mbar oxygen pressure. Comparing Figure 3.11 (a) and (b) to Figure 3.10, the large difference in rapid regime oxide growth rate are apparent. For $Si_{0.60}Ge_{0.40}(001)$ the rapid regime oxide growth rate for both Si 2p and Ge 3d is observed to be higher and last longer than for Si(001) and Ge(001).

(a)

(b)
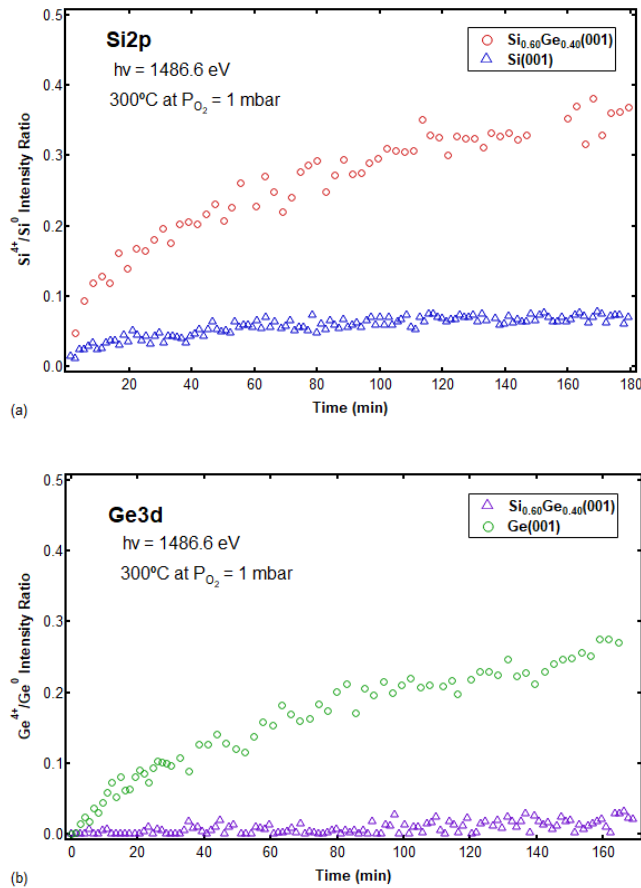
Figure 3.11: Time evolution of the oxide growth rate as measured by (a) the ratio of I_{Si4+} and I_{Si0} intensities from $Si_{0.60}Ge_{0.40}(001)$ and $Si(001)$ and (b) the ratio of I_{Ge4+} and I_{Ge0} intensities from $Si_{0.60}Ge_{0.40}(001)$ and $Ge(001)$ at an oxidation temperature of 300° and oxygen pressure of 1 mbar.

Comparing slow regime oxide growth time evolution, from Figure 3.11(a), it is apparent that growth of SiO_2 on Si(001) appears to reach a saturation point after which the oxide growth rate is very small. GeO_2 formation on Ge(001) is suppressed to such an extent that hardly any forms until nearly 90 minutes into exposure to 1mbar dry oxygen. This is to be expected as SiO_2 will form

more readily than GeO_2 thanks to its higher thermodynamic stability. Oxidation of Ge(001) to GeO_2 been demonstrated to be greatly enhanced at T_{ox} = 300°C [51]. For our experimental conditions, no such oxide growth enhancement is observed. Oxide growth rate on $Si_{0.60}Ge_{0.40}(001)$ in the slow regime shows no signs of saturation within the timescale measured.

Figure 3.12 shows the same $Si_{0.60}Ge_{0.40}(001)$ I_{4+} / I_0 intensity ratio as Figure 3.11, with suboxide intensity ratios added. Comparing Figure 3.12 to Figure 3.10 (a) and (b), differences and similarities in suboxide time evolution by surface are clear. At 300°C and P_{O2} = 1 mbar, the 1+ oxidation state intensity, relative to elemental intensity, is observed to be slightly higher for Si 2p from Si(001) when compared to $Si_{0.60}Ge_{0.40}(001)$ while the ratio for Ge 3d is little changed. For both $Si_{0.60}Ge_{0.40}(001)$ and Si(001), the 2+ oxidation state is observed to have little to no intensity.
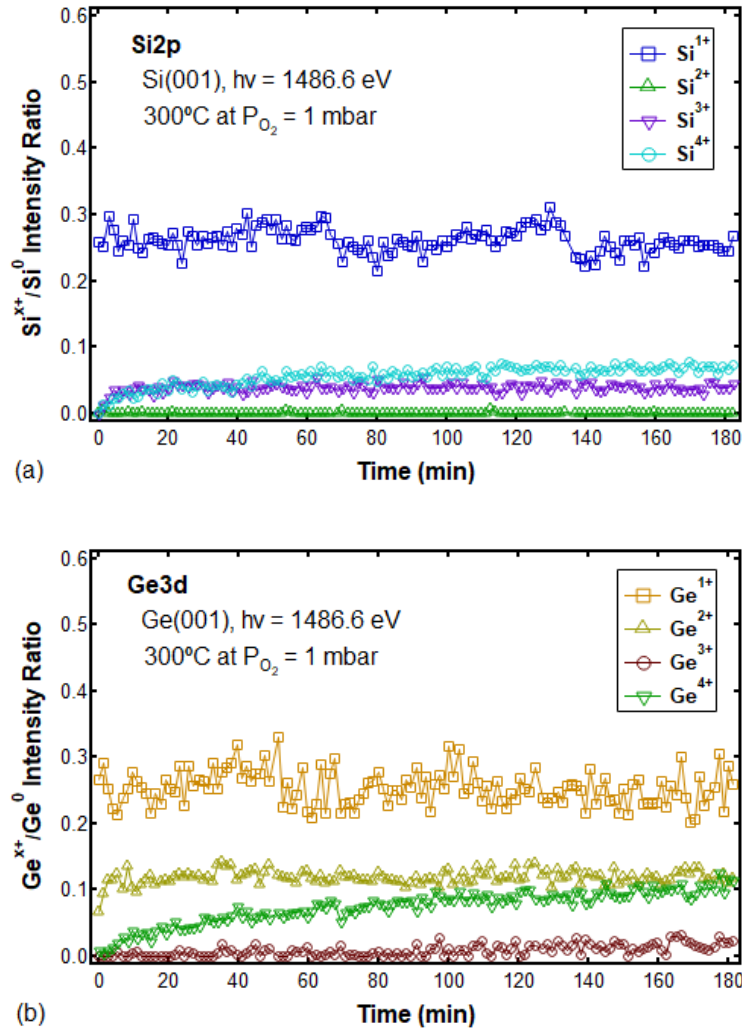
Figure 3.12: Time evolution of oxide growth rates on (a) Si(001) and (b) Ge(001) as measured by the intensity ratios I_{Six+} and I_{Si0} and I_{Gex+} and I_{Ge0} at 300° with oxygen pressure 1 mbar.

The data in Figure 3.12 further support the observation from Figure 3.8 that growth of the Si^{4+} oxidation state in the rapid regime is correlated to growth of the Si^{3+} oxidation state. Breakover in rate in the rapid regime occurs at maximum intensity of the I_{Si3+} / I_{Si0} ratio, identical behavior to Si 2p oxidation in the $Si_{0.60}Ge_{0.40}(001)$. For Si(001), this breakover occurs at a much lower ratio. Comparing Figures 3.12(b) and 3.8(d), the time evolution of Ge^{3+}, Ge^{2+}, and Ge^{1+} oxidation states is quite similar. Obviously the growth of Ge^{4+} is inhibited on Ge(001) relative to the alloy, but this does not appear to be correlated to a lack of formation of Ge^{3+}. It is believed that rapid regime

formation of the 4+ oxidation state relies on formation of 3+, but that continued formation of 4+ comes at the expense of further 3+ formation as the two are competing processes. Evidence of this can be observed in the saturation and eventual decrease (at large time) of the 3+ oxidation state intensity ratio in Figure 3.9 and 3.12(a), but steady increase in Figure 3.12(b) where formation of the 4+ oxidation state is severely inhibited. If the intensity ratios of the interfacial suboxides (1+, 2+) are taken to be representative of the thickness of the interfacial region, i.e. higher intensities ratios taken to mean a thicker interface, comparison of Figures 3.8 and 3.12 reveals that the interfacial thickness is likely quite similar for $Si_{0.60}Ge_{0.40}(001)$, $Si(001)$, and $Ge(001)$ oxidized in dry oxygen at 300°C. Moreover, the interfacial Si or Ge appear to have a very similar pattern in formation of 1+ or 2+. In other words, the preference of Si to form the 1+ oxidation state is consistent between $Si_{0.60}Ge_{0.40}(001)$ and pure $Si(001)$ and the tendency of Ge to form both 1+ and 2+ oxidation states is consistent between $Si_{0.60}Ge_{0.40}(001)$ and pure $Ge(001)$.

3.7   Conclusions

Oxide to elemental intensity ratios $I_{Si^{x+}} / I_{Si^0}$ and $I_{Ge^{x+}} / I_{Ge^0}$ versus time for $T_{ox} = 300°C$ and $P_{O2} = 1$ mbar and 0.01 mbar have been used to quantify oxide growth on $Si_{0.60}Ge_{0.40}(001)$ in real-time. Si is preferentially oxidized compared to Ge at all times. Oxidation proceeds via three oxide growth rate regimes: a rapid rate regime very early in oxidation, a slow rate quasi-saturated regime at long oxidation times, and a transition regime with a rate intermediate. For both Si and Ge, the rapid regime oxidation rate is higher at $P_{O_2} = 1$ mbar than 0.01 mbar. At low pressure, rapid regime oxidation of Ge is suppressed strongly compared to Si suggesting distinctly different initial stage oxidation pathways. It is hypothesized that oxygen atoms prefer to incorporate into the Si-Si bond by a dissociative configuration [63]. Lowered oxygen chemical potential at the interface via lower oxygen pressure slow dissociation reaction kinetics, but also significantly reduce the probability of the less favored peroxy-bridge Ge reaction [63]. A transition to a different limiting step occurs for both Si and Ge after some critical oxide thickness.

Oxidation rates of Si and Ge in the slow regime appear to be very nearly the same at both pressures suggesting the limiting mechanism in this regime is the breaking of substrate Si-Ge bonds. For both Si and Ge, the formation rate of the 4+ oxidation state is directly connected to the formation rate of its 3+ oxidation state. A decrease in pressure strongly affects formation of Ge^{3+} and Ge^{4+}, with the affect much weaker for Si. Pressure seems to have little effect on 1+ and 2+ interfacial suboxide states for both Si and Ge, suggesting that the quality of the interface is not changed when reducing oxygen pressure from 1 mbar to 0.01 mbar.

Rapid regime growth rate of the 4+ oxidation state for both Si and Ge in $Si_{0.60}Ge_{0.40}(001)$ is faster compared to pure Si(001) and Ge(001). For an interfacial reaction that is limited by oxygen dissociation, this growth rate enhancement can be explained by a possible synergy between adsorption and incorporation mechanisms between Si and Ge. By the Si mechanism, oxygen atoms tend to dissociate and agglomerate on the surface, whereas Ge spreads molecular oxygen on the surface by inter-dimer bridging configurations [63]. Slow regime growth rate of the 4+ oxidation state for both Si and Ge in $Si_{0.60}Ge_{0.40}(001)$ is faster compared to pure Si(001) and Ge(001). Rate enhancement compared to Si(001) can be explained by the weakness of Si-Ge bonds compared to Si-Si bonds. The oxidation rate of Ge(001) in the slow regime remains limited by dissociation of oxygen.

3.8   References

[1]   M. K. Bera *et al.*, "Rapid thermal oxidation of Ge-rich $Si_{1-x}Ge_x$ heterolayers," *J. Vac. Sci. Technol. A Vacuum, Surfaces, Film.*, vol. 24, no. 1, pp. 84–90, 2006.

[2]   J. S. Dunn *et al.*, "Foundation of rf CMOS and SiGe BiCMOS technologies," *IBM J. Res. Dev.*, vol. 47, no. 2.3, pp. 101–138, 2003.

[3]   W. D. J. Callister, *Materials Science and Engineering: An Introduction*, 7th ed. New York, NY, NY: John Wiley & Sons, Inc., 2007.

[4]   F. Schäffler, "High-mobility Si and Ge structures," *Semicond. Sci. Technol.*, vol. 12, no. 12, pp. 1515–1549, 1999.

[5]   F. Rozé *et al.*, "Oxidation kinetics of Si and SiGe by dry rapid thermal oxidation, in-situ steam generation oxidation and dry furnace oxidation," *J. Appl. Phys.*, vol. 121, no. 24, 2017.

[6]   E. Long, A. Azarov, F. Kløw, A. Galeckas, A. Yu Kuznetsov, and S. Diplas, "Ge redistribution in

SiO$_2$/SiGe structures under thermal oxidation: Dynamics and predictions," *J. Appl. Phys.*, vol. 111, no. 2, p. 024308, Jan. 2012.

[7]   T. Tezuka, N. Sugiyama, T. Mizuno, M. Suzuki, and S. I. Takagi, "A novel fabrication technique of ultrathin and relaxed SiGe buffer layers with high Ge fraction for sub-100 nm strained silicon-on-insulator MOSFETs," *Japanese J. Appl. Physics, Part 1 Regul. Pap. Short Notes Rev. Pap.*, vol. 40, no. 4 B, pp. 2866–2874, 2001.

[8]   M. A. Rabie, Y. M. Haddara, and J. Carette, "A kinetic model for the oxidation of silicon germanium alloys," *J. Appl. Phys.*, vol. 98, no. 7, pp. 074904–074913, Oct. 2005.

[9]   C.-T. Chang and A. Toriumi, "Preferential oxidation of Si in SiGe for shaping Ge-rich SiGe gate stacks," in *2015 IEEE International Electron Devices Meeting (IEDM)*, 2015, p. 21.5.1-21.5.4.

[10]   J. M. Madsen, Z. Cui, and C. G. Takoudis, "Low temperature oxidation of SiGe in ozone: Ultrathin oxides," *J. Appl. Phys.*, vol. 87, no. 4, pp. 2046–2051, Feb. 2000.

[11]   D. C. Paine, C. Caragianis, and a. F. Schwartzman, "Oxidation of Si$_{1-x}$Ge$_x$ alloys at atmospheric and elevated pressure," *J. Appl. Phys.*, vol. 70, no. 9, pp. 5076–5084, 1991.

[12]   F. K. LeGoues, R. Rosenberg, T. Nguyen, F. Himpsel, and B. S. Meyerson, "Oxidation studies of SiGe," *J. Appl. Phys.*, vol. 65, no. 4, pp. 1724–1728, 1989.

[13]   F. K. LeGoues, R. Rosenberg, and B. S. Meyerson, "Kinetics and mechanism of oxidation of SiGe: Dry versus wet oxidation," *Appl. Phys. Lett.*, vol. 54, no. 7, pp. 644–646, 1989.

[14]   W. Song and A. Toriumi, "Study of SiGe oxidation kinetics for preferential SiO$_2$ formation under a low O$_2$ pressure condition," *J. Appl. Phys.*, vol. 122, no. 18, pp. 185301–185307, Nov. 2017.

[15]   F. J. Himpsel, F. R. McFeely, A. Taleb-Ibrahimi, J. A. Yarmoff, and G. Hollinger, "Microscopic structure of the SiO$_2$/Si interface," *Phys. Rev. B*, vol. 38, no. 9, pp. 6084–6096, 1988.

[16]   C. Tételin, X. Wallart, J. P. Nys, L. Vescan, and D. J. Gravesteijn, "Kinetics and mechanism of low temperature atomic oxygen-assisted oxidation of SiGe layers," *J. Appl. Phys.*, vol. 83, no. 5, pp. 2842–2846, 1998.

[17]   M. Spadafora *et al.*, "Oxidation rate enhancement of SiGe epitaxial films oxidized in dry ambient," *Appl. Phys. Lett.*, vol. 83, no. 18, pp. 3713–3715, 2003.

[18]   O. W. Holland, C. W. White, and D. Fathy, "Novel oxidation process in Ge$^+$ implanted Si and its effect on oxidation kinetics," *Appl. Phys. Lett.*, vol. 51, no. 7, pp. 520–522, 1987.

[19]   S. J. Kilpatrick, R. J. Jaccodine, and P. E. Thompson, "Experimental study of the oxidation of silicon germanium alloys," *J. Appl. Phys.*, vol. 93, no. 8, pp. 4896–4901, 2003.

[20]   L. Fauquier *et al.*, "Benefits of XPS nanocharacterization for process development and industrial control of thin SiGe channel layers in advanced CMOS technologies," *Mater. Sci. Semicond. Process.*, vol. 70, pp. 105–110, Nov. 2017.

[21]   M. Rossi *et al.*, "In situ observation of wet oxidation kinetics on Si(100) via ambient pressure x-ray photoemission spectroscopy," *J. Appl. Phys.*, vol. 103, no. 4, p. 044104, Feb. 2008.

[22]   Y. Enta *et al.*, "Real-time observation of the dry oxidation of the Si(100) surface with ambient pressure X-ray photoelectron spectroscopy," *Appl. Phys. Lett.*, vol. 92, no. 1, p.012110, 2008.

[23]   K. W. Kolasinski, *Surface Science: Foundations of Catalysis and Nanoscience*, 3rd ed. New York, NY: John Wiley & Sons, Inc., 2012.

[24]   S. W. Park *et al.*, "Combined wet and dry cleaning of SiGe(001)," *J. Vac. Sci. Technol. A Vacuum, Surfaces, Film.*, vol. 33, no. 4, p. 041403, 2015.

[25]   K. Prabhakaran and T. Ogino, "Oxidation of Ge(100) and Ge(111) surfaces: an UPS and XPS study," *Surf. Sci.*, vol. 325, no. 3, pp. 263–271, Mar. 1995.

[26]   K. Prabhakaran and T. Ogino, "Oxidation of Ge(100) and Ge(111) surfaces: an UPS and XPS study," *Surf. Sci.*, vol. 325, no. 3, pp. 263–271, 1995.

[27]   S. Rivillon, Y. J. Chabal, F. Amy, and A. Kahn, "Hydrogen passivation of germanium (100) surface using wet chemical preparation," *Appl. Phys. Lett.*, vol. 87, no. 25, pp. 1–3, 2005.

[28]   S. Sun, Y. Sun, Z. Liu, D. I. Lee, S. Peterson, and P. Pianetta, "Surface termination and roughness of Ge(100) cleaned by HF and HCl solutions," *Appl. Phys. Lett.*, vol. 88, no. 2, pp. 1–3, 2006.

[29]   M. T. Anthony, "Spectrometer Calibration," in *Practical Surface Analysis by Auger and X-ray Photoelectron Spectroscopy*, D. Briggs and M. P. Seah, Eds. New York, NY: John Wiley & Sons, Inc., 1983, pp. 429–435.

[30]   P. H. Citrin, P. Eisenberger, and D. R. Hamann, "Phonon broadening of x-ray photoemission linewidths," *Phys. Rev. Lett.*, vol. 33, no. 16, pp. 965–969, 1974.

[31]   J. F. Moulder, W. F. Stickle, P. E. Sobol, and K. D. Bomben, *Handbook of X-Ray Photoelectron Spectroscopy*. Eden Prairie, MN: Perkin-Elmer Corporation, 1992.

[32]   J. H. Oh *et al.*, "Chemical structure of the ultrathin SiO2/Si(100) interface: An angle-resolved Si 2p photoemission study," *Phys. Rev. B*, vol. 63, no. 20, p. 205310, 2001.

[33]   A. Ohta, T. Fujioka, H. Murakami, S. Higashi, and S. Miyazaki, "X-ray photoelectron spectroscopy study of interfacial reactions between metal and ultrathin Ge oxide," *Jpn. J. Appl. Phys.*, vol. 50, no. 10, pp. 3–8, 2011.

[34]   P. J. Grunthaner, M. H. Hecht, F. J. Grunthaner, and N. M. Johnson, "The localization and crystallographic dependence of Si suboxide species at the SiO_2/Si interface," *J. Appl. Phys.*, vol. 61, no. 2, pp. 629–638, 1987.

[35]   D. Schmeisser *et al.*, "Surface oxidation states of germanium," *Surf. Sci.*, vol. 172, no. 2, pp. 455–465, Jul. 1986.

[36]   J. M. Hill, D. G. Royce, C. S. Fadley, L. F. Wagner, and F. J. Grunthaner, "Properties of oxidized silicon as determined by angular-dependent X-ray photoelectron spectroscopy," *Chem. Phys. Lett.*, vol. 44, no. 2, pp. 225–231, Dec. 1976.

[37]   M. Matsui, H. Murakami, T. Fujioka, A. Ohta, S. Higashi, and S. Miyazaki, "Characterization of chemical bonding features at metal/GeO_2 Interfaces by X-ray photoelectron spectroscopy," *Microelectron. Eng.*, vol. 88, no. 7, pp. 1549–1552, 2011.

[38]   W. Smekal, W. S. M. Werner, and C. J. Powell, "Simulation of electron spectra for surface analysis (SESSA): a novel software tool for quantitative Auger-electron spectroscopy and X-ray photoelectron spectroscopy," pp. 1059–1067, 2005.

[39] J. P. Dismukes, L. Ekstrom, and R. J. Paff, "Lattice Parameter and Density in Germanium-Silicon Alloys," *J. Phys. Chem.*, vol. 68, no. 10, pp. 3021–3027, 1964.

[40] H. Z. Massoud, "Thermal Oxidation of Silicon in Dry Oxygen Growth-Rate Enhancement in the Thin Regime," *J. Electrochem. Soc.*, vol. 132, no. 11, pp. 2685–2693, 1985.

[41] N. M. Ravindra, R. A. Weeks, and D. L. Kinser, "Optical properties of GeO_2," *Phys. Rev. B*, vol. 36, no. 11, pp. 6132–6134, 1987.

[42] G. Beamson and D. Briggs, "High resolution monochromated x-ray photoelectron spectroscopy of organic polymers: A comparison between solid state data for organic polymers and gas phase data for small molecules," *Mol. Phys.*, vol. 76, no. 4, pp. 919–936, 1992.

[43] A. B. Christie, "X-ray photoelectron spectroscopy," in *Methods of Surface Analysis*, J. M. Walls, Ed. Cambridge, UK: Cambridge University Press, 1989, pp. 127–168.

[44] J. C. Riviere, "Instrumentation," in *Practical Surface Analysis by Auger and X-ray Photoelectron Spectroscopy*, D. Briggs and M. P. Seah, Eds. New York, NY: John Wiley & Sons, Inc., 1983, pp. 17–85.

[45] S. Hofmann, "Depth Profiling," in *Practical Surface Analysis by Auger and X-ray Photoelectron Spectroscopy*, D. Briggs and M. P. Seah, Eds. John Wiley & Sons, Inc., 1983, pp. 141–179.

[46] F. J. Grunthaner and J. Maserjian, "Experimental Observations of the Chemistry of the SiO_2/Si Interface," *IEEE Trans. Nucl. Sci.*, vol. 24, no. 6, pp. 2108–2112, Dec. 1977.

[47] D. Mori *et al.*, "Comparative study of GeO_2/Ge and SiO_2/Si structures on anomalous charging of oxide films upon water adsorption revealed by ambient-pressure X-ray photoelectron spectroscopy," *J. Appl. Phys.*, vol. 120, no. 9, p. 095306, Sep. 2016.

[48] J. M. C. Thornton and R. H. Williams, "A photoemission study of passivated silicon surfaces produced by etching in solutions of HF," *Semicond. Sci. Technol.*, vol. 4, no. 10, pp. 847–851, 1989.

[49] G. Lucovsky, S. S. Chao, J. E. Tyler, and G. De Maggio, "An XPS study of sputtered a-Si,Ge alloys," *J. Vac. Sci. Technol.*, vol. 21, no. 3, pp. 838–844, 1982.

[50] A. Agarwal, J. K. Patterson, J. E. Greene, and A. Rockett, "Ultraviolet ozone induced oxidation of epitaxial $Si_{1-x}Ge_x$(111)," *Appl. Phys. Lett.*, vol. 63, no. 4, pp. 518–520, 1993.

[51] A. Molle, M. N. K. Bhuiyan, G. Tallarida, and M. Fanciulli, "In situ chemical and structural investigations of the oxidation of Ge(001) substrates by atomic oxygen," *Appl. Phys. Lett.*, vol. 89, no. 8, pp. 083504–083506, Aug. 2006.

[52] C. S. Fadley, "Basic Concepts of X-ray Photoelectron Spectroscopy," in *Electron Spectroscopy: Theory, Techniques, and Applications*, vol. 2, C. R. Brundle and A. D. Baker, Eds. New York, NY: Academic Press, 1978, pp. 1–155.

[53] S. M. Goldberg, C. S. Fadley, and S. Kono, "Photoionization cross-sections for atomic orbitals with random and fixed spatial orientation," *J. Electron Spectros. Relat. Phenomena*, vol. 21, no. 4, pp. 285–363, 1981.

[54] P. J. Cumpson and M. P. Seah, "Elastic Scattering Corrections in AES and XPS. II. Estimating

Attenuation Lengths and Conditions Required for their Valid Use in Overlayer/Substrate Experiments," *Surf. Interface Anal.*, vol. 25, no. 6, pp. 430–446, Jun. 1997.

[55] Z. H. Lu, "Air-stable Cl-terminated Ge(111)," *Appl. Phys. Lett.*, vol. 520, no. October 2018, p. 520, 1995.

[56] K. Ikeda, S. Imai, and M. Matsumura, "Atomic layer etching of germanium," *Applied Surface Science*, vol. 112, pp. 118–121, 1997.

[57] M. S. Carroll, J. C. Sturm, and M. Yang, "Low-Temperature Preparation of Oxygen- and Carbon-Free Silicon and Silicon-Germanium Surfaces for Silicon and Silicon-Germanium Epitaxial Growth by Rapid Thermal Chemical Vapor Deposition," *J. Electrochem. Soc.*, vol. 147, no. 12, pp. 4652–4659, 2000.

[58] Z. H. Lu, M. J. Graham, D. T. Jiang, and K. H. Tan, "SiO_2/Si(100) interface studied by Al Kα x-ray and synchrotron radiation photoelectron spectroscopy," *Appl. Phys. Lett.*, vol. 63, no. 21, pp. 2941–2943, 1993.

[59] W. F. Zhang, T. Nishimula, K. Nagashio, K. Kita, and A. Toriumi, "Conduction band offset at GeO_2/Ge interface determined by internal photoemission and charge-corrected x-ray photoelectron spectroscopies," *Appl. Phys. Lett.*, vol. 102, no. 10, pp. 2–6, 2013.

[60] P. W. Loscutoff and S. F. Bent, "REACTIVITY OF THE GERMANIUM SURFACE: Chemical Passivation and Functionalization," *Annu. Rev. Phys. Chem.*, vol. 57, no. 1, pp. 467–495, 2006.

[61] I. Ohdomari, H. Akatsu, Y. Yamakoshi, and K. Kishimoto, "Study of the interfacial structure between Si (100) and thermally grown SiO_2 using a ball-and-spoke model," *J. Appl. Phys.*, vol. 62, no. 9, p. 3751, 1987.

[62] T. David *et al.*, "Kinetics and Energetics of Ge Condensation in SiGe Oxidation," *J. Phys. Chem. C*, vol. 119, no. 43, pp. 24606–24613, 2015.

[63] C. Mastail *et al.*, "Oxidation of Germanium and Silicon surfaces (100): A comparative study through DFT methodology," *IOP Conf. Ser. Mater. Sci. Eng.*, vol. 41, no. 1, pp. 0–10, 2012.

[64] B. E. Deal and A. S. Grove, "General relationship for the thermal oxidation of silicon," *J. Appl. Phys.*, vol. 36, no. 12, pp. 3770–3778, 1965.

[65] B. K. Boksteen, J. Schmitz, and R. J. E. Hueting, "Interface Trap Density Estimation in FinFETs Using the gm/ID Method in the Subthreshold Regime," *IEEE Trans. Electron Devices*, vol. 63, no. 5, pp. 1814–1820, 2016.

[66] G. Hollinger and F. J. Himpsel, "Oxygen chemisorption and oxide formation on Si (111) and Si (100) surfaces," vol. 640, no. 111, 2010.

Chapter 4: Characterization of Oxide Growth on Silicon-Germanium Alloys with Simulated Electron Spectra

4.1   Introduction to Simulation of Electron Spectra for Surface Analysis (SESSA)

A large amount of data is needed to interpret an Auger-electron or photoelectron spectrum quantitatively. The required data include basic physical information on the solid in question (density, composition, atomic number of the constituent atoms, structure, etc.), information on the process of creating the emitted electrons (photoelectric effect and Auger-electron emission) as well as the various parameters governing the interaction of the emitted electrons with the solid on their way out of the sample [1]. Physical properties of the solid itself aside, the number of required parameters describing photoelectron emission and transport alone is large: the total inelastic mean free path, the differential elastic-scattering cross section, the total elastic-scattering cross section (or, alternatively the transport cross section if the transport approximation is used), the photoionization cross section, the photoionization asymmetry parameter, the electron-impact ionization cross section, the fluorescence yield, and the Auger-electron backscattering factors [1]. With the importance of accurate determination of electron trajectories in a solid for XPS and AES, a complete database of electron scattering cross sections and electron inelastic mean free paths was necessary to standardize quantification. In 2005, the National Institute of Standards and Technology (NIST) released Standard Reference Database 100 which uses an expert system to query other NIST databases (i.e. cross-section Database 64, IMFP Database 71, etc.) to obtain all of the physical data required to perform quantitative interpretation of an electron spectrum for a specimen with a given composition. Moreover, fully traceable references are provided for each quantity.

The NIST Database for Simulation of Electron Spectra for Surface Analysis (SESSA) combines the extensive dataset of Database 100 with a simulation module that provides an estimate of peak intensities as well as the energy and angular distribution of the emitted electron flux using the partial intensity approach (PIA) [1]. This method uses a Monte Carlo technique to evaluate the ensemble of trajectories from the distribution of scattering angles and energy losses in individual collisions, then counts for each trajectory the number of inelastic collisions it has experienced [2]. This collision counting algorithm is much more efficient than classical algorithms that track the photoelectron kinetic energy explicitly [2]. The algorithm is made even more efficient by modeling only the photoelectrons that actually make it to the "detector" by invoking symmetry properties of the kinetic equation, or reciprocity relationships for linear transfer [2]. This is known as the trajectory reversal technique. Using statistical weights, the algorithm associates each trajectory with a distribution of n_i fold scattered particles and therefore each trajectory contributes to all energies in the spectrum. The PIA, statistical weights, and trajectory reversal together generate the spectra output by SESSA software. A comparisons of the simulated peak intensities for electrons that escape without being inelastically scattered, or the zero-order partial intensity, exhibit close agreement with experimental results [1]. The main limitations of the simulation algorithm are that surface and intrinsic excitations [3] are neglected and that the excitation depth distribution function (DDF) is assumed to be constant inside the specimen. Furthermore, the assumption of an atomically flat surface restricts the applicability of SESSA to cases where the surface morphology is not expected to influence the spectral intensities [1]. Regarding the database, the most significant lack of data are the empirical peak shapes of photoelectron and Auger-electron transitions [1]. Simulation of peak shapes is particularly difficult due to the fact that the shape of the energy distribution for inelastic

scattering in solids is complex and a comprehensive database for this quantity is currently not available within SESSA nor anywhere else in convenient form [1]. In the most current version of SESSA, the lineshape of an XPS peak is approximated to be Lorentizian with a FWHM of 1.4 eV [1].

In spite of these limitations, SESSA is a powerful resource for the simulation of the zero-order partial intensities used in XPS quantitative chemical analysis. There is currently no universal model to calculate the thickness of a mixed $Si_{1-x}Ge_x$ oxide; this is made difficult by uncertainty regarding how much Ge is incorporated into the oxide as it grows. A key strength of SESSA is that the use of simulated relative intensities generated by varying parameters describing an overlayer (composition, morphology, density, thickness) can be performed to match experimentally observed relative intensities which can provide detailed information [30]. For example, a mixed $Si_{1-x}Ge_x$ oxide can be characterized by simulating relative intensities for varying oxide Ge content and thickness and comparing these relative intensity ratios to experimental data.

4.2   SESSA Experimental Details

In SESSA, the user defines a substrate material upon which layers can be modeled. For the substrate and each successive layer the user specifies chemical composition, thickness, and morphology. SESSA default layer morphologies are planar, roughness, islands, spheres, and layered spheres. Planar assumes an ideally flat surface; roughness allows specification of a relative surface area, which is a measure of the distribution of surface tilt angles that are associated with surfaces roughness [1]. The increase in signal intensity due to increased surface area is accounted for with this RSA parameter [4]. Simple nanostructures are built in, including

islands for modeling terraces and spheres for modeling nanoparticles. The layered spheres

morphology allows one to simulate a spherical particle consisting of an inner core with an

arbitrary number of overlayers [4]. More complex geometries can be modeled using the

PENGEOM package, which is a general purpose geometry package that allows one to define

quasi-arbitrary geometries using quadratic surfaces [4]. For example, Chudzicki et al. [4] used

SESSA and the PENGEOM package to simulate self-assembled monolayers of alkanethiols on

gold nanoparticles. Cleary the potential applications of SESSA are extensive, but as with any

modeling software an understanding of the input parameters and how the calculations are

performed is critical. Furthermore, the simulation outputs must be analyzed using sound

knowledge of photoemission processes and physical models of surface transport properties of the

emitted electrons.

Modeling of oxide growth on a flat substrate is relatively straightforward. Figure 4.1

shows the SESSA graphical user interface to specify the data input for a basic model of a mixed

oxide $(Si,Ge)O_2$ on $Si_{0.60}Ge_{0.40}$.
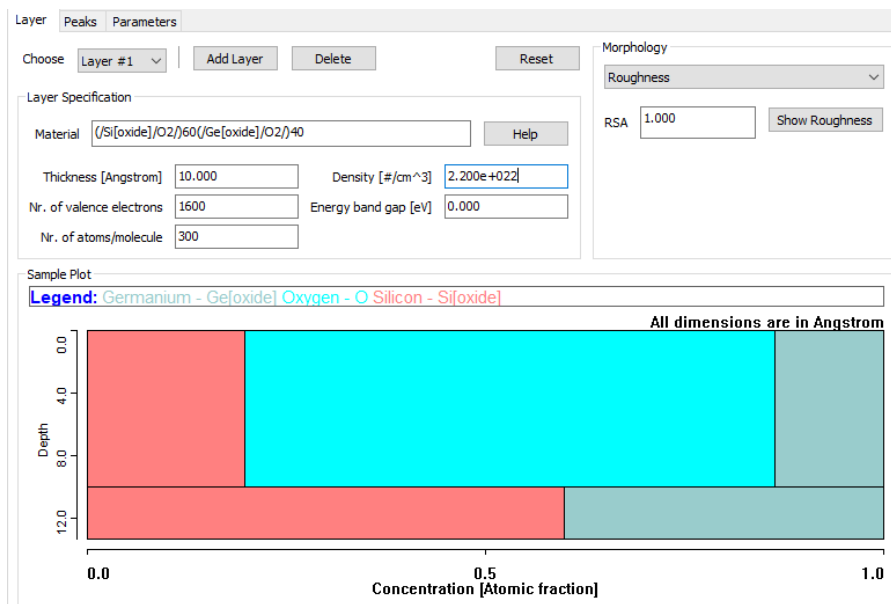
Figure 4.1: SESSA V2.0 graphical user interface for specifying layer chemical composition, thickness, and morphology. An arbitrary number of layers can be added to correspond to as complex of a layering pattern as necessary. The program distinguishes between photoelectrons from Si(Ge) in the substrate and Si(Ge) in the oxide by bracketed notation [oxide] next to the corresponding element.

When chemical composition for a layer is entered into SESSA, a value for the atomic density of each modeled layer is determined by the software. For elemental solids and for over 2500 inorganic compounds, this quantity is read from a database. For all other materials, the density of a compound is estimated on the basis of the densities for each elemental constituent; these estimated densities may have uncertainties of more than 100% [30]. For this analysis, the atomic densities for pure Si (n_{Si}), pure Ge (n_{Ge}), and pure $Si_{0.60}Ge_{0.40}$ (n_{SiGe}) were input manually as 4.991×10^{22}, 4.415×10^{22}, and 4.775×10^{22} atoms cm^{-3} respectively. These are derived from mass densities 2.3277, 5.3256, and 3.6405 g cm^{-3} [32]. Densities of $Si_{1-x}Ge_x$ oxide layers of varying Ge fraction were determined by linear interpolation between that of amorphous SiO_2 ($n_{SiO_2} = 2.25 \times 10^{22}$ atoms cm^{-3} [33]) and amorphous GeO_2 ($n_{GeO_2} = 2.12 \times 10^{22}$ atoms cm^{-3}, calculated from mass density 3.677 g cm^{-3} [34]). For the perfectly mixed oxide with Ge fraction $x = 0.40$, this results in an oxide density of 2.20×10^{22} atoms cm^{-3}, which is within error of 2.1×10^{22} atoms cm^{-3} determined by Liu et al. [5] for a mixed oxide with Ge fraction $x = 0.36$. Due to the large number of variables that can influence the simulated spectra, the surface is modeled as ideal and changes made only if necessary to achieve good agreement between simulated spectra and experimental data. To begin, the interface between the alloy and oxide is modeled as atomically smooth (RSA = 1.00) with no surface contamination. In addition, the initial model assumes a constant Ge concentration in both the alloy and the oxide. While this is almost certainly not true, some mean Ge fraction should approximate the concentration gradient with

reasonable accuracy. With the user interface in Figure 4.1, the oxide composition and thickness can be varied from simulation to simulation generating relative intensities with each iteration. However, the simulated spectra intensities will poorly represent experimental data without inputting spectrometer configuration settings to account for differences in sensitivity.

Source type and spectrometer configuration parameters must be included in the SESSA model to accurately simulate experimental spectra. The X-ray sources available in SESSA are limited but include the two most common X-ray sources used for XPS, i.e. Al Kα and Mg Kα. Radiation settings including photon energy and fraction of polarized light are automatically populated. As source to analyzer angle and emission angle can vary from instrument to instrument, and in the case of emission angle from experiment to experiment, configuring spectrometer geometry to match experimental conditions is important as they can influence the photoemission process. Figure 4.2 shows the geometry customization options available in SESSA, where multiple configurations can be saved to match experiments on the same sample with varying sources and emission angles.
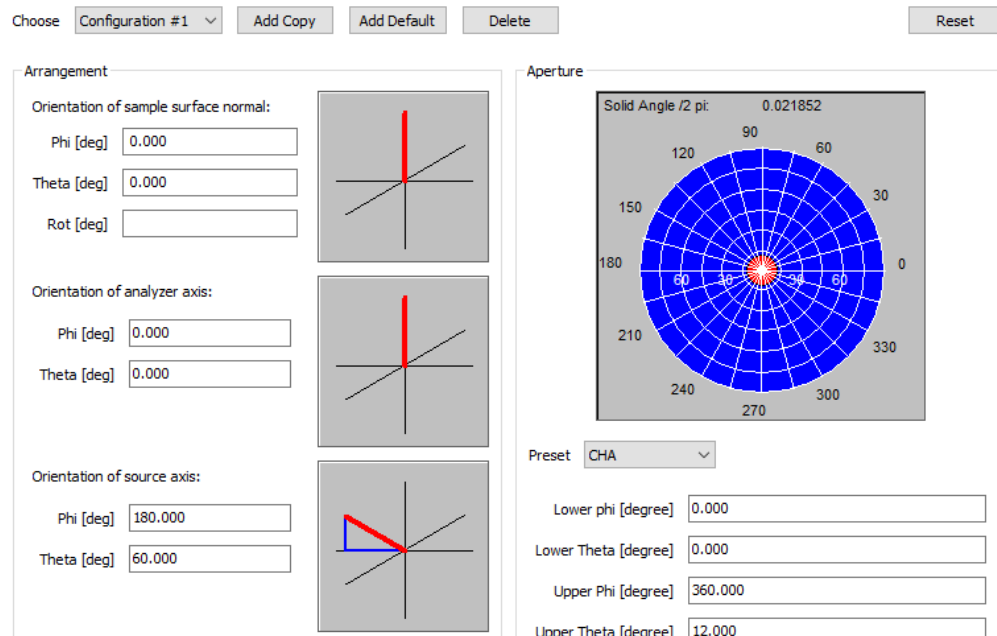
Figure 4.2: SESSA V2.0 graphical user interface for specifying spectrometer configuration including geometrical arrangement and solid angle of acceptance.

Using "orientation of sample surface normal" and "orientation of analyzer axis", the emission angle can be matched to experimental conditions. The angles themselves are arbitrary; only their angle relative to one another is significant. For the SPECS APXPS near-ambient pressure (NAP) cell used for this analysis, the emission angle is fixed at $\theta = 0°$ so the analyzer axis is collinear with the sample surface normal. Using "orientation of source axis" the source to analyzer angle can be made to match the experiment as well. Again, only the angle of the source relative to the analyzer is significant. For the SPECS APXPS system, the angle between the Al Kα monochromatized source and the analyzer axis is $\alpha = 60°$. The orientation of the X-ray electric field polarization vector can also be specified. All spectrometer geometry orientations are specified in spherical coordinates with a fixed frame of reference. Lastly, the solid angle of acceptance is specified by either selecting a preset aperture or constructing a custom aperture based on its solid angle of acceptance. The analyzer acceptance angle is specified in spherical

coordinates in a frame of reference in which the z-axis is parallel to the analyzer axis. The SPECS APXPS instrument is equipped with a PHOIBOS concentric hemispherical analyzer (CHA), thus the CHA preset has been selected in Figure 4.2. With sample, source, and configuration parameters set to match experimental conditions, SESSA can be used to simulate XPS spectra.

In the SESSA simulation graphical user interface, a few parameters can be inputted which change the partial intensity calculations used in the simulation. The convergence factor, which defaults to 1×10^{-2}, determines the total number of trajectories used in the algorithm. If the fractional change of the sum of all considered partial intensities is below the convergence factor, generation of trajectories is terminated [1]. Changing this number automatically changes the number of trajectories if auto populate is selected; a lower convergence factor increases the number of trajectories and increases computational cost. Two electron transport approximations can be selected. The transport approximation replaces the exact differential cross section with the transport cross section [3]. This choice implies that elastic scattering is assumed to be isotropic and that the distance between successive elastic deflections is taken to be equal to the transport mean free path [1]. The straight line approximation (SLA) means SESSA assumes that the paths of the electrons in the solid are straight lines, or elastic scattering of the signal electrons is neglected [1]. This approximation is justified by the radiative field principle in the case of smooth source distribution [3]. For this analysis, the SLA is used for transport approximation. Figure 4.3 shows SESSA simulated spectra generated using layer specifications from Figure 4.1 and spectrometer geometry parameters from Figure 4.2.
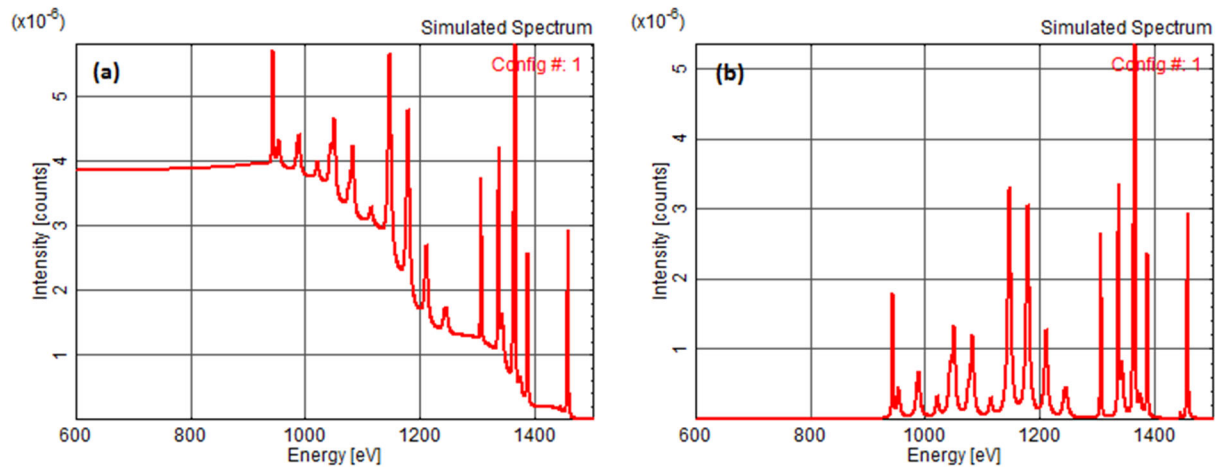
Figure 4.3: SESSA V2.0 model simulation plots of photoelectron intensity versus kinetic energy generated using sample layer specifications from Figure 4.1 and spectrometer geometry parameters from Figure 4.2. Both (a) and (b) have been generated with a convergence factor of 1×10^{-2} and SLA, however (b) includes no collisions and thus only zero-order partial intensities.

Figure 4.3(a) was simulated with collisions that are modeled and thus has an inelastic scattering background to include higher order partial intensities. Figure 4.3(b) has only zero-order partial intensities that are modeled where collisions have been excluded from the simulation. In both plots, the zero-order partial intensities are identical. It is important to note here that SESSA data for partial intensities is believed to be realistic, but partial energy distribution data is much less reliable [1]. The probability for an energy loss in an individual excitation is represented by the differential inelastic inverse mean free path (DIIMFP); reliable spectral shapes require realistic data on DIIMFP which is currently not available for Auger electron transitions [1]. This is particularly problematic for compounds with Ge as it has a large Auger signal that extends from 300-600 eV. Consequently, in this analysis only zero-order intensities and intensity ratios will be compared to experimental zero-order intensities and intensity ratios. Direct comparison of the

spectra would require importing empirical data for Ge Auger spectral lineshapes which is beyond the scope of this analysis.

4.3 Estimation of $Si_{0.60}Ge_{0.40}$ Oxide Composition and Thickness from Simulated Electron Spectra

The thickness of $Si_{1-x}Ge_x$ oxides (d_{ox}) have been estimated from XPS using Si 2p photoelectrons by the following equation [6]

$$d_{ox} = \lambda_{ox} \cos \theta \ln[R_{exp}/R_0 + 1] \qquad (1)$$

where λ_{ox} is the Si 2p photoelectron mean free path in the oxide, R_{exp} is the experimental Si 2p intensity ratio of oxidized silicon and unoxidized silicon I_{ox} / I_{Si}, and R_0 is the ratio of $I_{ox,\infty}$ / $I_{Si,\infty}$ which is determined by measuring thick thermal oxides and H-terminated Si(001) surfaces [6]. This method assumes that the ratio R_0 for thick thermal oxide on H-terminated Si(001) is equal to the R_0 for thick thermal SiO_2 oxide on $Si_{1-x}Ge_x$(001), a ratio that would change based on the Ge content in the alloy. From Chapter 3 we saw that at T_{ox} = 300°C and with oxygen pressure equal to 1 or 0.01 mbar, both Si and Ge are oxidized at the $Si_{0.60}Ge_{0.40}$(001) surface. This occurs in both the rapid and slow regimes. Thus Ge is being incorporated into the oxide and contributing to the oxide thickness; equation 1 is not suited for this scenario. Due to the lack of available models to calculate $Si_{1-x}Ge_x$ alloy oxide thickness using XPS data, SESSA software was used to model a $Si_{0.60}Ge_{0.40}$ semi-infinite surface with varying thicknesses and compositions of oxide. SESSA contains all the necessary physical quantities to simulate XPS spectra, so simulated relative intensities can be compared with experimental relative intensities to estimate the oxide thickness and composition. SESSA allows the simulation of O 1s to elemental ratios (I_{O1s} / I_{Si0} and I_{O1s} / I_{Ge0}) to determine the oxide thickness. These ratios will increase as the oxide

thickness increases assuming the alloy concentration is constant. For our studies, high resolution O 1s spectra were obtained at the end of each experiment, thus I_{O1s} / I_{Si0} and I_{O1s} / I_{Ge0} intensity ratios can be used estimate final oxide thickness by comparison with SESSA simulations. SESSA intensity ratios can also be useful for the determination of oxide composition by using the I_{Si4+} / I_{Ge4+} intensity ratio. This ratio can provide an estimate to indicate how much of each element is incorporated into the oxide. The oxide to its associated elemental intensity ratio I_{Si4+} / I_{Si0} and I_{Ge4+} / I_{Ge0} can also be used for further analysis. These intensity ratios should serve as a measure of the accuracy of the model as a whole, including both alloy composition and oxide composition considerations. However, as the oxide grows the buried elemental photoelectrons must contend with a higher probability of scattering by the oxide which could affect these ratios.

Data collected and analyzed in Chapter 3 was used to check for significant changes in the oxide composition with time. This data was used to plot the change in stoichiometric oxide intensity ratio I_{Si4+} / I_{Ge4+} with time. Figure 4.4 shows ratios from (a) three replicate experiments at 1 mbar and (b) four replicate experiments at 0.01 mbar. Figure 4.4(a) Exp B tracked the Si 2p and Exp C tracked the Ge 3d; Figure 4.4(b) Exp D and Exp F tracked the Si 2p, Exp E and Exp G tracked the Ge 3d. For these oxidation experiments only one core-level is scanned repeatedly during the early stages of oxidation so no ratios can be calculated for the first 30 minutes. In Figure 4.4(a) Exp B early oxidation ratios were made with Si 2p data from Exp B and Ge 3d data from Exp C. Figure 4.4(b) Exp D (Exp F) early oxidation ratios were made with Si 2p data from Exp D (Exp F) and Ge 3d data from Exp E (Exp G). It has been shown in Chapter 2 that these oxidation experiments are reproducible, thus these ratios represent changes that occur during the oxidation of the $Si_{0.60}Ge_{0.40}(001)$ surface.
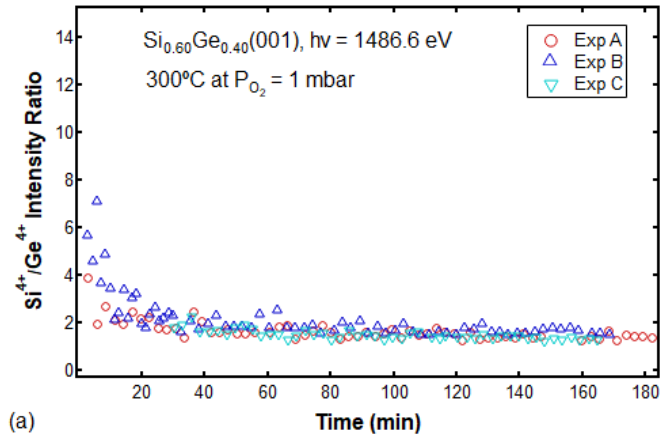
(a)
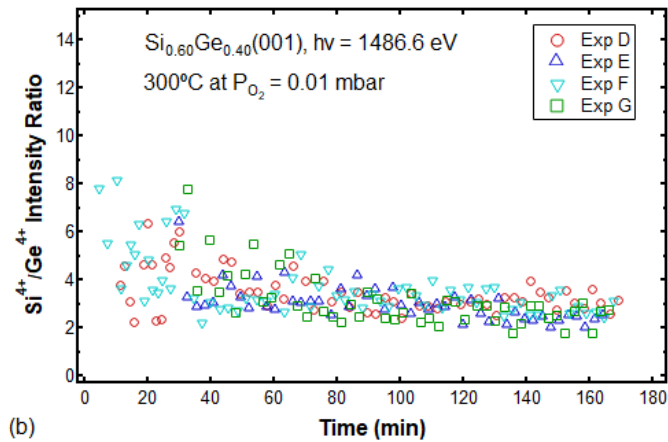
(b)

Figure 4.4: Time evolution of the oxide intensity ratio I_{Si4+} / I_{Ge4+} for oxidation temperature $T_{ox} = 300°C$ and (a) three replicate experiments (A, B, C) at 1 mbar oxygen pressure, (b) four replicate experiments (D, E, F, G) at 0.01 mbar oxygen pressure.

From Figure 4.4 it is apparent that the transient oxide growth behavior in the rapid regime when the alloy is first exposed to oxygen is significantly different from what appears to be quasi-steady state slow regime oxide growth. Significantly more Si is incorporated into the oxide than Ge in the rapid regime, as indicated by high ratios in Figures 4.4(a) and 4.4(b). From the transition regime into the slow regime, the oxidation of Ge begins to catch up until the ratio is

nearly constant. The Ge content in this transient regime could be modeled in SESSA as many layers with a gradient Ge fraction. However, without an accurate method of determining the oxide thickness and compositional profile from intensity ratios a priori the selection of the Ge fraction and thickness of each modeled layer in the transient regime would be arbitrary. For this analysis it will be assumed that the oxide composition is constant at the quasi-saturated values in Figure 4.4. From Figure 4.4 (a) and (b), the ratio reaches quasi-steady state at $I_{Si4+} / I_{Ge4+} = 1.55 \pm 0.19$ and 3.01 ± 0.61, respectively. As expected, less Ge is incorporated into the oxide at 0.01 mbar than at 1 mbar [7]. Using the I_{Si4+} / I_{Ge4+} ratios the composition of the oxide can be determined.

High resolution Si 2p and Ge 3d spectra after 170 min oxidation in $T_{ox} = 300°C$ and oxygen pressures of 1 mbar and 0.01 mbar (e.g. Figures 3.5 and 3.6) were used to determine experimental intensity ratios associated with final (or near final) oxide thickness. These ratios can be found in Table 4.1.

Table 4.1: Experimental intensity ratios determined from high resolution spectra collected after 170 minutes of oxidation at $T_{ox} = 300°C$ and oxygen pressures of 1 mbar and 0.01 mbar. Data from replicates at each pressure are given.

Experiment	I_{Si4+} / I_{Si0}	I_{Ge4+} / I_{Ge0}	I_{O1s} / I_{Si0}	I_{O1s} / I_{Ge0}
1 mbar (A)	0.35	0.26	2.85	2.80
1 mbar (B)	0.38	0.21	3.05	3.04
1 mbar (C)	0.31	0.21	2.77	2.66
Average	0.35±0.05	0.23±0.03	2.89±0.14	2.83±0.19
0.01 mbar (D)	0.32	0.12	2.05	1.99
0.01 mbar (E)	0.34	0.12	1.99	1.92

0.01 mbar (F)	0.26	0.09	1.53	1.51
0.01 mbar (G)	0.24	0.11	2.09	2.04
Average	0.29±0.05	0.11±0.01	1.92±0.26	1.87±0.24

The data in Table 4.1 indicates that for each pressure the results are quite reproducible for the experimental conditions studied. Some variance was observed due to noise in the XPS spectra and errors associated with the fitting procedures. Two trends are particularly noticeable in the data: the I_{Ge4+} / I_{Ge0} ratio is lower for lower oxygen pressures (a trend already verified by Figure 3.9) indicating a reduction in Ge oxidation. Furthermore, the oxide is likely thinner for lower oxygen pressures as indicated by the lower I_{O1s} / I_{Si0} and I_{O1s} / I_{Ge0} ratios. These trends suggest that rate of Ge incorporation is correlated to oxygen partial pressure and the thickness of the oxide (i.e. oxides with a lower Ge content are thinner). Although the O 1s peak overlaps with the Ge $L_2M_{23}M_{23}$ Auger when using Al Kα X-rays there is a significant difference in the I_{O1s} / I_{Si0} and I_{O1s} / I_{Ge0} ratios for the different oxygen partial pressures. SESSA does not currently model suboxides thus the interface between alloy and oxide was assumed to be abrupt and the oxide perfectly stoichiometric. The Si^{4+} and Ge^{4+} oxidation states are obtained from a deconvolution of the experimental data. These results can be quantified separate from suboxide states which allows for direct comparison to simulated ratios from SESSA. Seah and Spencer determined that calculation of oxide thickness including all oxidation states yields physical thicknesses on average 0.118 nm larger than the method accounting only for Si^{4+} [8]. All of the oxidation states are correlated to the concentration of oxygen atoms, which contribute to the O 1s intensity. Due to the FWHM of the O 1s peak and the small change in the O 1s binding energy for the suboxides of Si and Ge we are not able to deconvolute these components from the spectra. Thus,

the experimental O 1s intensity cannot be directly compared to simulated O 1s intensity without a correction. In our analysis, the suboxide contributions to the O 1s intensity were estimated from Si 2p and Ge 3d suboxide intensity using instrument RSFs and assuming all suboxides are +1 oxidation state. This assumption was used due to the relatively small proportion of +2 state in the spectra (Figures 3.5 and 3.6). Using I_{O1s} / I_{Si0} and I_{O1s} / I_{Ge0} values in Table 4.1, we used a trial and error method in SESSA to calculate intensity ratios that can be compared to experimental values. A perfectly mixed oxide (Ge fraction x = 0.40) was first modeled using thicknesses between 2-50 Å. Next, the Ge content was decreased to account for preferential oxidation of Si. For simplicity, the Ge content in the oxide is modeled to be constant and no Ge rich layer (GRL) was modeled between oxide and bulk $Si_{0.60}Ge_{0.40}$. Since the oxide for our experimental conditions is expected to be thin, any GRL is expected to be negligible compared to the sampling depth of photoelectrons from the substrate. The SESSA analysis is given in Table 4.2.

Table 4.2: Simulated intensity ratios obtained from SESSA modeling of an oxide layer on $Si_{1-x}Ge_x$ alloy. Best fit to 1 mbar experimental data with alloy composition $Si_{0.60}Ge_{0.40}$ was obtained with a 33 Å thick $Si_{0.71}Ge_{0.29}O_2$ oxide layer. Best fit to 0.01 mbar experimental data obtained with 28 Å thick $Si_{0.83}Ge_{0.17}O_2$ oxide layer. Values in parenthesis were obtained by adjusting model Ge content in the bulk alloy to x = 0.35 while keeping oxide thickness (d_{ox}) and composition constant.

SESSA model	I_{Si4+} / I_{Ge4+}	I_{Si4+} / I_{Si0}	I_{Ge4+} / I_{Ge0}	I_{O1s} / I_{Si0}	I_{O1s} / I_{Ge0}
$Si_{0.71}Ge_{0.29}O_2$, d_{ox} = 33 Å	1.4 (1.4)	0.35 (0.31)	0.19 (0.22)	3.4 (3.0)	2.7 (3.0)
$Si_{0.83}Ge_{0.17}O_2$, d_{ox} = 28 Å	2.9 (2.8)	0.27 (0.25)	0.078 (0.089)	2.2 (2.1)	1.8 (2.1)

From Table 4.1, the I_{O1s} / I_{Si0} and I_{O1s} / I_{Ge0} experimental intensity ratios are quite close to one another for experiments performed at a given oxygen partial pressure. SESSA data indicates that an alloy surface with Ge content x= 0.35 has an I_{Si0} / I_{Ge0} elemental intensity ratio approximately equal to 1. Alloy atomic percent calculations were performed with high resolution XPS data obtained using a PHI5600 system with a base pressure $< 2x10^{-10}$ mbar. Pass energy for high resolution spectra was set to 23.5 eV. The binding energy scale was calibrated as described in Chapter 3. RSFs were obtained from Moulder et al. [9]. From this analysis we determined the $Si_{1-x}Ge_x$ alloy Ge fraction x = 0.40. These high resolution spectra were taken of the surface before oxidation. For simplicity, when using SESSA we have assumed that the alloy and oxide atomic concentrations are not changing with time. While this assumption should be valid at such low temperatures, the formation of GRL would result in an increase in the apparent Ge concentration in the XPS sampling depth. Assuming the $Si_{1-x}Ge_x$ alloy Ge content of the clean surface is x = 0.40, the SESSA intensity ratios will vary with oxide thickness in a predictable manner. Our analysis was performed by modeling $Si_{0.71}Ge_{0.29}O_2$ (T_{ox} = 300°C, P_{O2} = 1 mbar) and $Si_{0.83}Ge_{0.17}O_2$ (T_{ox} = 300°C, P_{O2} = 0.01 mbar) oxide growth on $Si_{0.60}Ge_{0.40}$. A non-linear regression model was used to obtain an expression for Si 2p simulated intensity ratio R_{sim} = I_{Si4+} / I_{Si0} as a function of mixed oxide thickness for each pressure, derived from equation 1:

$$R_{sim} = R_0\left(e^{d_{ox}/\lambda_{ox}cos\theta} - 1\right) \qquad (2)$$

Where λ_{ox} is the Si 2p photoelectron mean free path in the mixed oxide, d_{ox} is the mixed oxide thickness, R_0 is the ratio of $I_{ox,inf}$ / $I_{SiGe,inf}$ (or the ratio of Si 2p intensity from a well-developed mixed oxide to Si 2p intensity from a semi-infinite $Si_{0.60}Ge_{0.40}$ substrate), and θ is the emission angle. Minimization of normalized error yielded best fits with R_0 = 0.23 and λ_{ox} = 35.4 Å for 1

mbar data and $R_0 = 0.27$ and $\lambda_{ox} = 35.6$ Å for 0.01 mbar data. These IMFP values are near

SESSA values for Si $2p_{3/2}$ in a mixed oxide. Using equation 1 along with appropriate R_0 and λ_{ox}

values, experimental time resolved I_{Si4+} / I_{Si0} intensity ratios were correlated to mixed oxide

thickness and plotted. The results can be found in Figure 4.5.
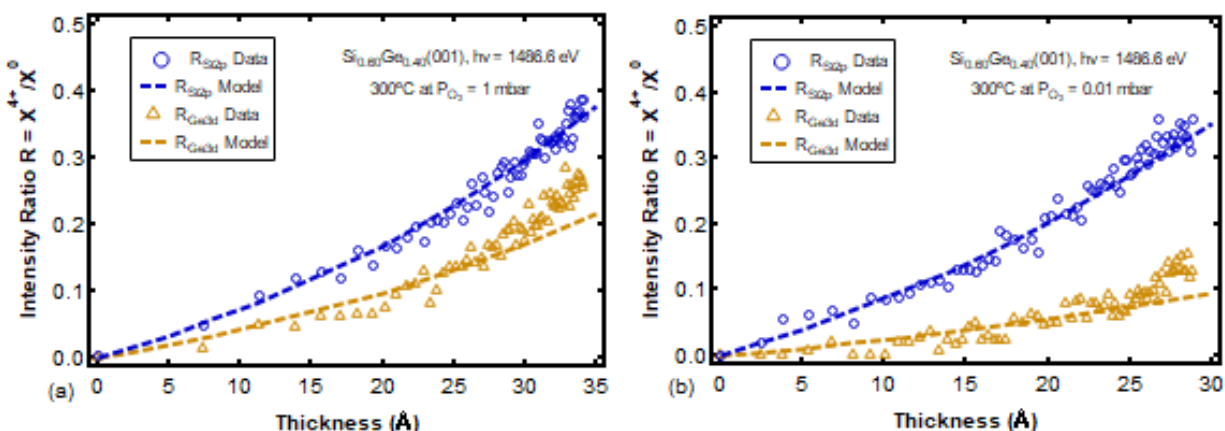
Figure 4.5: SESSA was used to model a $Si_{0.60}Ge_{0.40}(001)$ surface with varying thicknesses and Ge content

(x) of the oxide. Modeled I_{Si4+} / I_{Si0} and I_{Ge4+} / I_{Ge0} intensity ratios and I_{O1s} / I_{Si0} and I_{O1s} / I_{Ge0} intensity

ratios were used to estimate oxide composition and thickness. Dashed lines in (a) correspond to ratios

generated from model with x = 0.29 germanium fraction in the oxide. Dashed lines in (b) correspond to

ratios generated from model with x = 0.17 germanium fraction in the oxide. Experimental I_{Si4+} / I_{Si0}

intensity ratios (circles) and I_{Ge4+} / I_{Ge0} intensity ratios (triangles) at 300°C (a) 1 mbar and (b) 0.01 mbar

appear to follow the modeled intensities well.

The dashed lines in Figure 4.5 represent SESSA model predictions of I_{Si4+} / I_{Si0} and I_{Ge4+} / I_{Ge0}

intensity ratios for growing oxides on $Si_{0.60}Ge_{0.40}$ alloy for two compositions: (a) $Si_{0.71}Ge_{0.29}O_2$ at

300°C and 1 mbar and (b) $Si_{0.83}Ge_{0.17}O_2$ at 300°C and 0.01 mbar. The quality of the SESSA

model can be assessed by the extent to which the dashed lines in Figure 4.5 track the

experimental data. For both Figures 4.5 (a) and (b), the experimental intensity ratios track

SESSA model predictions well for oxides thinner than about 26 Å. Above this oxide thickness, the I_{Ge4+} / I_{Ge0} data diverges from SESSA model predictions. Recall the data from Table 4.2, which suggests that the fully oxidized high resolution intensity ratios I_{O1s} / I_{Si0} and I_{O1s} / I_{Ge0} can be better modeled by decreasing the model alloy Ge content. However, from Figure 4.5 it is apparent that for oxides thicker than 26 Å the rate of change of I_{Ge4+} / I_{Ge0} intensity ratio with oxide thickness iincreases leading to higher than expected values. Decreasing SESSA model $Si_{1-x}Ge_x$ alloy Ge fraction to x= 0.35 yields a better fit for oxides greater than 26 Å, but at the expense of poor fit for thinner oxides.

Recall that in SESSA the depth distribution function (DDF) is assumed to be constant within an emitting source (or modeled layer), which is determined by the compositional depth profile of the specimen. The DDF represents the probability that an electron leaving the solid at a certain emission angle was generated at a certain depth and reached the surface without energy loss [10]. Thus SESSA assumes that the DDF will not change based on where in a layer it is emitted. In usual overlayer models, like those introduced in Chapter 2, XPS signal intensity analysis is based on the following assumptions: (i) the deposited layer has a uniform structure and an interface of negligible thickness, (ii) the attenuation mechanism does not depend on the overlayer thickness, and (iii) the photoelectron intensity is attenuated exponentially in the direction of the analyzer [11]. From studies on the interfacial suboxides in Chapter 3, it is clear that for oxides grown on $Si_{0.60}Ge_{0.40}(001)$ at 300°C and P_{O2} = 1 or 0.01 mbar the interfacial region is not of negligible thickness particularly early in oxidation when the oxide is thin. Werner et al. determined as an oxide grows thicker and exceeds the total mean free path of the photoelectrons travelling through it, more and more of these photoelectrons will have an enhanced path length owing to elastic scattering [12]. The slope of the DDF of such a layer

corresponds to the IMFP. Thus, the attenuation mechanism is expected to change based on overlayer thickness. To make things even more difficult, it has been shown that photoelectrons emerging from solids may not be exponentially related to their depth of origin [10]. The apparent Ge^0 concentration in the sampling depth should rise with growing oxide as GRL forms, and thicker oxides suppress oxidation of Ge as oxygen chemical potential at the interface decreases [13]. In other words, exactly the opposite behavior observed in the I_{Ge4+} / I_{Ge0} ratios in Figure 4.5. Elastic scattering of Ge^0 photoelectrons for oxides thicker than 26 Å may be the cause of deviation from the SESSA model, possibly due to a non-uniform depth distribution function. By equation 2, the I_{Ge4+} / I_{Ge0} intensity ratio behavior observed in Figure 4.5 can be simulated by decreasing λ_{ox} supporting the hypothesis that the attenuation mechanism is changing with overlayer thickness. However, the SESSA model relies on multiple assumptions so care should be taken when attempting to pinpoint a singular cause for deviation from the model.

The purpose of Figures 4.5(a) and 4.5(b) were to estimate the accuracy with which SESSA could predict experimental intensity ratios. These figures indicate that the R_0 and λ_{ox} values determined from the SESSA R_{sim} regression analysis predicts the experimental ratios reasonably well, particularly for Si 2p photoelectrons. To determine oxide growth rates, experimental time resolved I_{Si4+} / I_{Si0} ratios, along with SESSA determined R_0 and λ_{ox} values at each pressure, were used in equation 1 to calculate oxide thickness. The results can be found in Figure 4.6.
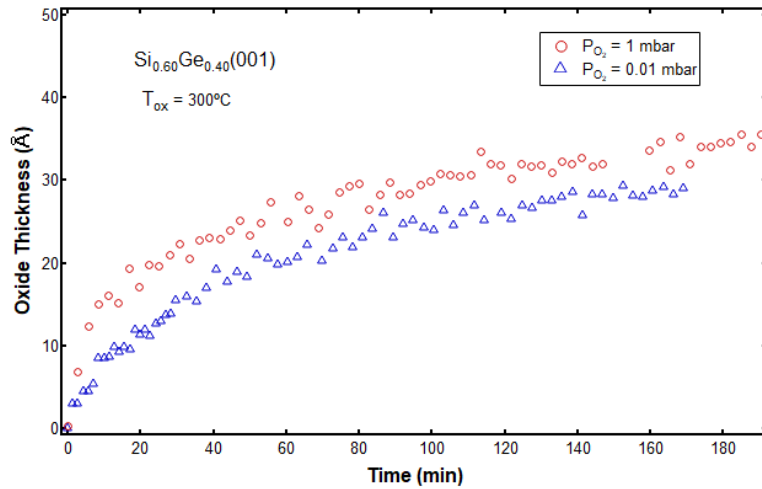
Figure 4.6: $Si_{0.60}Ge_{0.40}$(001) oxide growth with time at 300°C and oxygen pressure of 1 mbar (circles) and 0.01 mbar (triangles). Experimental time resolved I_{Si4+} / I_{Si0} intensity ratios were compared to SESSA model to estimate oxide thickness.

From Figure 4.6, growth rates in the rapid regime and slow regime can be determined at each pressure and compared. At T_{ox} = 300°C and P_{O2} = 1 mbar the $Si_{0.60}Ge_{0.40}$(001) rapid regime oxide growth, defined by large positive slope in the first ~10 minutes of oxidation, is 96 Å/h. For T_{ox} = 300°C and P_{O2} = 0.01 mbar, the rapid regime rate was 65 Å/h. The difference in rapid regime rates with pressure is significant, with rate at 1 mbar about 1.5 times the rate at 0.01 mbar. This initial comparatively slower rate at 0.01 mbar results in ~5 Å less total oxide growth after 170 minutes of oxidation. It is hypothesized that dissociation of oxygen is rate limiting in the rapid regime, with lower oxygen pressures leading to lower rate for both Si and Ge due to the lower chemical potential of molecular oxygen at the interface [14]. It has been shown that Ge is much more sensitive to changes in pressure, suggesting a stronger dependence on oxygen chemical potential. In the slow regime oxide growth rate, defined generally by rate at times greater than 70 minutes, the values were 3.3 Å/h at P_{O2} = 1 mbar and 3.9 Å/h at P_{O2} = 0.01 mbar. The higher slow regime growth rate

at lower pressure is supported by similar findings for dry oxidation of Si(001), which was attributed to a lower saturation oxide thickness at lower pressures that results in a reduction of the diffusion barrier [15]. However, diffusion of oxidant in the oxide is not expected to be rate limiting until the oxide is much thicker [16], around 250 Å as predicted by the Deal-Grove model [17]. In our experiments the transition regime begins too early in oxidation, when the oxide is less than ~20 Å, to be shifting to a diffusion limited mechanism. Due to noise in the XPS spectra and errors associated with the fitting procedures, the difference in slow regime rates at P_{O2} = 1 mbar versus 0.01 mbar is not believed to be significant. Comparing our $Si_{0.60}Ge_{0.40}(001)$ slow regime oxidation rates at P_{O2} = 1 mbar and 0.01 mbar to APXPS data for real time oxidation of Si(001), the alloy slow regime rates are significantly higher at comparable experimental conditions [15]. It is believed this catalytic effect is due to the weakness of the Si-Ge bond compared to the Si-Si bond [18].

4.4   Conclusion

In conclusion, NIST Simulated Electron Spectra for Surface Analysis (SESSA) was used to estimate oxide composition and thickness after approximately 170 minutes of $SI_{0.60}Ge_{0.40}(001)$ dry thermal oxidation at 300°C with P_{o2} = 1 mbar and 0.01 mbar. Through trial and error, mixed oxides $(Si,Ge)O_2$ were modeled and simulated I_{Si4+} / I_{Si0}, I_{Ge4+} / I_{Ge0}, I_{Si4+} / I_{Si0}, and I_{Ge4+} / I_{Ge0} intensity ratios as they vary with oxide thickness were compared to experimental ratios. At 1 mbar oxygen pressure, best model to experimental data was achieved with oxide Ge fraction x = 0.29 and final oxide thickness of 33 Å. At 0.01 mbar, best model was achieved with oxide Ge fraction x = 0.16 and final oxide thickness of 28 Å. Non-linear regression of simulated I_{Si4+} / I_{Si0} intensity ratio as it varies with oxide thickness assuming constant oxide composition was used to determine R_0 and λ_{ox} for use in equation 1 to estimate oxide thickness at any time. Results indicate at 1 mbar

a rapid regime oxide growth rate of 96 Å/h, and at 0.01 mbar an oxide growth rate of 65 Å/h. Slow

regime growth rate is 3.3 Å/h and 3.9 Å/h for 1 mbar and 0.01 mbar oxygen pressure, respectively.

These values can be compared with rapid regime rate of 64 Å/h and slow regime rate of 2.1 Å/h

for dry thermal oxidation of Si(001) at 300°C and P_{o2} = 1 Torr (1.33 mbar) from Enta et al. [15].

The data suggests a growth rate enhancement in both the rapid and slow regimes for

$Si_{0.60}Ge_{0.40}$(001) relative to Si(001). In the rapid regime, this could be attributed to a synergistic

oxygen dissociation effect between Si and Ge which have different dissociative pathways [19]. In

the slow regime, this is likely due to the weakness of the Si-Ge bond relative to the Si-Si bond

causing more Si and Ge atoms to participate in the oxidation reaction thus increasing reaction rate.

The primary determining factor in oxide composition and thickness is rate in the rapid regime,

with decreasing oxygen pressure resulting in lower rapid regime rate, lower Ge fraction, and a

slightly thinner oxide.

4.5   References

[1]   W. S. M. Werner, W. Smekal, and C. J. Powell, "NIST Database for the Simulation of Electron Spectra for Surface Analysis (SESSA) - User's Guide," *NIST Database Simul. Electron Spectra Surf. Anal. - User's Guid.*, 2011.

[2]   W. S. M. Werner, "Simulation of electron spectra for surface analysis using the partial-intensity approach (PIA)," *Surf. Interface Anal.*, vol. 37, no. 11, pp. 846–860, Nov. 2005.

[3]   W. S. M. Werner, "Electron transport in solids for quantitative surface analysis," *Surf. Interface Anal.*, vol. 31, no. 3, pp. 141–176, 2001.

[4]   M. Chudzicki, W. S. M. Werner, A. G. Shard, Y.-C. Wang, D. G. Castner, and C. J. Powell, "Evaluating the Internal Structure of Core–Shell Nanoparticles Using X-ray Photoelectron Intensities and Simulated Spectra," *J. Phys. Chem. C*, vol. 119, no. 31, pp. 17687–17696, Aug. 2015.

[5]   W. S. Liu *et al.*, "Wet oxidation of GeSi at 700°C," *J. Appl. Phys.*, vol. 71, no. 8, pp. 4015–4018, 1992.

[6]   J. M. Madsen, Z. Cui, and C. G. Takoudis, "Low temperature oxidation of SiGe in ozone: Ultrathin oxides," *J. Appl. Phys.*, vol. 87, no. 4, pp. 2046–2051, 2000.

[7]   W. Song and A. Toriumi, "Study of SiGe oxidation kinetics for preferential SiO2 formation under a low O2 pressure condition," *J. Appl. Phys.*, vol. 122, no. 18, pp.

185301–185307, Nov. 2017.

[8]   M. P. Seah and S. J. Spencer, "Ultrathin SiO2 on Si II . Issues in quantification of the oxide thickness," pp. 640–652, 2002.

[9]   J. F. Moulder, W. F. Stickle, P. E. Sobol, and K. D. Bomben, *Handbook of X-Ray Photoelectron Spectroscopy*. Eden Prairie, MN: Perkin-Elmer Corporation, 1992.

[10]   A. Jablonski and C. J. Powell, "Formalism and parameters for quantitative surface analysis by Auger electron spectroscopy and x-ray photoelectron spectroscopy," *Surf. Interface Anal.*, vol. 20, no. 9, pp. 771–786, 1993.

[11]   A. Jablonski, "Comparison of the attenuation lengths and the inelastic mean-free path for photoelectrons in silver," *J. Vac. Sci. Technol. A Vacuum, Surfaces, Film.*, vol. 8, no. 1, p. 106, 1990.

[12]   W. S. M. Werner, W. H. Gries, and H. Störi, "Analytical expression describing the attenuation of Auger electrons and photoelectrons in solids," *Surf. Interface Anal.*, vol. 17, no. 10, pp. 693–704, 1991.

[13]   H. K. Liou, P. Mei, U. Gennser, and E. S. Yang, "Effects of Ge concentration on SiGe oxidation behavior," *Appl. Phys. Lett.*, vol. 59, no. 10, pp. 1200–1202, 1991.

[14]   C. T. Chang and A. Toriumi, "Preferential oxidation of Si in SiGe for shaping Ge-rich SiGe gate stacks," *Tech. Dig. - Int. Electron Devices Meet. IEDM*, p. 21.5.1-21.5.4, 2015.

[15]   Y. Enta *et al.*, "Real-time observation of the dry oxidation of the Si(100) surface with ambient pressure x-ray photoelectron spectroscopy," *Appl. Phys. Lett.*, vol. 92, no. 1, p. 012110, 2008.

[16]   F. K. LeGoues, R. Rosenberg, T. Nguyen, F. Himpsel, and B. S. Meyerson, "Oxidation studies of SiGe," *J. Appl. Phys.*, vol. 65, no. 4, pp. 1724–1728, 1989.

[17]   B. E. Deal and A. S. Grove, "General relationship for the thermal oxidation of silicon," *J. Appl. Phys.*, vol. 36, no. 12, pp. 3770–3778, 1965.

[18]   M. A. Rabie, Y. M. Haddara, and J. Carette, "A kinetic model for the oxidation of silicon germanium alloys," *J. Appl. Phys.*, vol. 98, no. 7, pp. 074904–074913, Oct. 2005.

[19]   C. Mastail *et al.*, "Oxidation of Germanium and Silicon surfaces (100): A comparative study through DFT methodology," *IOP Conf. Ser. Mater. Sci. Eng.*, vol. 41, no. 1, pp. 0–10, 2012.

Chapter 5: Summary and Future Research Directions

5.1   Summary of Conclusions

Dry thermal oxidation of $Si_{0.60}Ge_{0.40}(001)$ alloy at 300°C and two oxygen pressures, 1 and 0.01 mbar, has been characterized using chemical state resolved ambient pressure X-ray photoelectron spectroscopy. Si(001) and Ge(001) oxidized at 300°C and 1 mbar oxygen pressure were also analyzed as references. Experimental intensities ratios were compared to NIST Simulated Electron Spectra for Surface Analysis (SESSA) intensity ratios to determine oxide composition and thickness.

The $Si_{0.60}Ge_{0.40}(001)$ oxidation rate is observed to show three rate regimes: rapid regime within the first 10-15 minutes of oxidation when the oxide is thin, a transitionary regime, and a quasi-saturated slow regime when the oxide is relatively thick. The rapid regime oxidation rates of Si and Ge are observed to be pressure dependent, with both rates decreasing with decreasing oxygen pressure. Ge oxidation appears to be more sensitive to decreases in oxygen pressure, resulting in significant suppression of GeO_2 formation compared to SiO_2 as pressure is decreased from 1 to 0.01 mbar. These results suggest a difference in the influence of oxygen pressure on the interfacial reaction of molecular oxygen with Si and Ge. It is hypothesized that dissociation of oxygen is rate limiting for oxidation of $Si_{0.60}Ge_{0.40}(001)$ in the rapid regime, with differences in adsorption and incorporation mechanisms between Si and Ge resulting in different sensitivities to oxygen pressure. Slow regime oxidation rate is observed to be similar for Si and Ge, and either weakly dependent on pressure or pressure independent. A slight increase in slow regime rate is noted at 0.01 mbar when compared to 1 mbar, however the difference is likely within error of linear fits to data. It is apparent that the limiting mechanism is the slow regime is

distinctly different from the rapid regime suggesting that as the oxide grows, the mechanism shifts from the interfacial reaction to some other limiting step.

5.2   Future Research Directions

The main goal in understanding Ge concentration in the alloy and the oxide, as well as accurately determining oxide thickness, it to compare experimental observations with universal kinetic models of oxide growth on $Si_{1-x}Ge_x$ alloy. Rabie et al. [1] proposed a model which predicts oxide thickness, Si profile in the underlying $Si_{1-x}Ge_x$ layer, and GeO_2 fraction in the oxide. The model accounts for five fluxes: (i) F_1, flux of oxidant moving through the oxidizing gas towards the top surface; (ii) F_2, flux of oxidant molecules diffusing through the oxide layer towards the oxidizing interface; (iii) F_3, flux of oxidant molecules reacting with Si to form $SiO2$; (iv) F_4, flux of oxidant molecules reacting with Ge to form GeO_2; and (v) F_5, flux of Si atoms replacing Ge in the oxide. Fluxes F_1 and F_2 are described in the conventional Deal-Grove model [2]:

$$F_1 = h(C^* - C_0) \qquad F_2 = -D_{eff}(dC/dz) \qquad (1)$$

where z is coordinate direction along the sample surface normal, h is the gas phase transport coefficient, C^* is the equilibrium concentration of oxidant in the oxide, C_0 is the concentration of the oxidant at the outer surface of the oxide at any given time, D_{eff} is the effective diffusion coefficient of oxidant in the oxide, and dC/dz is the oxidant concentration gradient in the oxide. Rabie et al. [1] accounted for alloy effects on C^* and D_{eff} by accounting for the fraction of Ge at the surface of the alloy, θ:

$$C^* = \theta C^*_{Ge} + (1 - \theta)C^*_{Si} \qquad\qquad D_{eff} = \theta D_{oxGe} + (1 - \theta)D_{oxSi} \qquad (2)$$

Where parameters with a Si subscript are for the case of pure SiO_2 and Ge for the case of pure GeO_2. D_{oxSi} and D_{oxGe} are expected to be approximately the same [1], showing Arrhenius dependence on temperature and type of oxidant (affects pre-exponential factor). C^* for dry oxygen has been shown to be consistently higher for Ge than for Si [1], but as the gas phase transport coefficient is expected to be large compared to diffusivity [2]. Thus, flux F_2 is assumed to be the rate limiting step in the transport of oxidant to the interface at experimental conditions of interest.

At all pressures observed, the oxidation rate in the quasi-saturated regime is higher for $Si_{0.60}Ge_{0.40}(001)$ than for pure $Si(001)$ and $Ge(001)$. This behavior does not follow the D_{eff} expression in equation set 2 as if D_{oxSi} and D_{oxGe} are the same and the interfacial Ge fraction is x = 0.50 as predicted by minimization of free energy, D_{eff} would be equal to D_{oxSi} and D_{oxGe}. This would suggest that the limiting mechanism in the quasi-saturated regime is the interfacial reaction. However, the data also suggest for $Si_{0.60}Ge_{0.40}(001)$ a possible rate increase with lower oxygen pressure in quasi-saturated regime at constant temperature. According to Ionvino et al [3], the equilibrium concentration of oxygen in SiO_2 is expected to increase with pressure and decrease with temperature. Therefore, a rate increase at lower pressure could be due to a lower barrier to effective diffusion. This has been hypothesized to be true for SiO_2 [4], but the evidence is weak for our $Si_{0.60}Ge_{0.40}(001)$ experiments. The rate difference with pressure is too small to say with confidence that a significant difference exists.

Rabie et al. [1] describe the interfacial oxidation reaction fluxes F_3 and F_4 as

$$F_3 = k'_{Si} C_{Si} a_{i,Si} C_i \qquad\qquad F_4 = k'_{Ge} C_{Ge} (1 - a_{i,Si}) C_i \qquad\qquad (3)$$

where $a_{i,Si}$ is the Si activity at the interface, C_i is the concentration of oxidant molecules at the oxidizing interface, k'_{Si} and k'_{Ge} are the Si and Ge oxidation rate constants, and C_{Si} and C_{Ge} are the atomic densities of Si and Ge. If $Si_{1-x}Ge_x$ is assumed to be an ideal solid solution, the silicon activity is equal to the Si fraction in the alloy [5]. Hellberg et al. [5] hypothesized that the interfacial reaction rate constants k'_{Si} and k'_{Ge} are primarily affected by the type of oxidant and the crystalline structure of the alloy which are constant in our experiments. The concentration of oxidant molecules at the oxidizing interface C_i is dependent on oxidant pressure, but for a given experiment P_{O_2} will be the same for F_3 and F_4. The effective coefficient of Si-Ge interdiffusion, D_{SiGe}, can influence the relative interfacial concentrations C_{Si} and C_{Ge}. As Si is preferentially oxidized it is depleted in the near interface region causing a net flux of Si to the interface. This will lead to steady-state C_{Si} and C_{Ge} as a function of D_{SiGe}, which is expected to be dependent on $Si_{1-x}Ge_x$ crystallinity and composition [5]. This steady-state interfacial atomic density is expected be satisfied in the slow regime. In this regime, C_{Si} and C_{Ge} are constant so they can be included in new reaction rate constants $k_{Si} = k'_{Si} C_{Si}$ and $k_{Ge} = k'_{Ge} C_{Ge}$. Referring back to Figure 3.7, the oxidation rate in the slow regime appears to be independent C_i suggesting a pseudo zero-order reaction with rate constants that will change based on the type of oxidant, crystalline structure of the alloy, and interdiffusion coefficient D_{SiGe}. Moreover, at our experimental conditions k_{Si} and k_{Ge} are similar reflected in similar oxidation rates in the slow regime in agreement with values reported by Rabie et al. [1].

We have shown that in the rapid regime decreasing oxygen partial pressure affects the oxidation rate of Si (F_3) and Ge (F_4) differently, with GeO_2 formation being suppressed relative to SiO_2. From discussion of the terms in fluxes F_3 and F_4, none of the terms can account for the observed difference that oxygen partial pressure has on the oxidation rate of Si and Ge. The

interfacial atomic densities C_{Si} and C_{Ge} are likely not constant in this regime, as preferential oxidation of Si is rapid. Moreover, at the onset of oxidation, C_i is likely comparable in magnitude to C_{Si} and C_{Ge} but would drop rapidly as the oxidant molecules are consumed in the oxidation reaction and an oxide diffusion barrier grows. This would suggest that early in oxidation the interfacial reactions are second-order, depending on alloy Ge fraction and oxygen partial pressure. C_i would eventually become very small compared to C_{Si} and C_{Ge}, possibly resulting in a pseudo first-order reaction. In our experiments, we observe early in oxidation that F_3 and F_4 decrease with decreasing P_{O_2} from 1.0 to 0.01 mbar. This behavior is predicted by equations in set 3, as C_i is expected to decrease with decreasing partial pressure. If k'_{Si} and k'_{Ge} are independent of oxidant pressure as proposed by Hellberg et al. [5], the differences in the observed rapid regime interfacial Si and Ge reaction rates in Figure 3.7 must be explained by differences in C_{Si} and C_{Ge} at the interface only or a new term which could account for differences in oxygen adsorption and incorporation between Si and Ge.

More data on the effect of pressure on the oxidation rates of Si and Ge in the rapid and slow regimes should be obtained to (i) check if the slow regime oxidation rate is indeed independent of oxygen partial pressure and (ii) to accurately define how oxygen partial pressure influences rapid regime oxidation rates. Performing rapid regime uptake experiments at a synchrotron beamline, which can rapidly repeat scans (as short as 18 seconds) thanks to a very high signal to noise ratio, could allow a clearer picture of the uptake rates between Si and Ge. Moreover, the chamber pressure at these facilities can be computer controlled allowing many pressure data sets. With high resolution uptake data at many pressures, perhaps an expression can be developed to describe rapid regime oxygen uptake dependence on pressure for $Si_{0.60}Ge_{0.40}(001)$ alloy. Additionally, experiments at a synchrotron beamline could be performed

to tune photon energy to maximize surface sensitivity. With high signal to noise ratios small changes in the 4+ oxidation state peak intensity could be observed, lending confidence to statements regarding the pressure dependence of $Si_{0.60}Ge_{0.40}(001)$ oxidation rate in the quasi-saturated regime.

Rabie et al. [1] describes the concentration of Si at the interface by the following expression

$$D_{SiGe} \frac{d(yC_{Si})}{dz}\bigg|_{interface} = F_3 + F_5 - F_4 \qquad (4)$$

where F_5 is the replacement reaction where Si replaces Ge in GeO_2. At our experimental conditions, no evidence of a replacement reaction was observed as this reaction should function to depress the reaction rate of Ge relative to Si. Rabie et al. [1] hypothesized that this reaction should be limited by the breaking of bonds in $(Si,Ge)O_2$ already formed and as a result depends on temperature only. Song et al. [6] demonstrated that at constant pressure by increasing the temperature the mechanism shifts to favor F_5 at the expense of F_4 resulting in complete preferential oxidation of Si. According to this paper, at $T_{ox} = 300°C$ a pressure of $P_{O2} = 10^{-11}$ mbar would be required for complete preferential oxidation of Si. However, from our experimental data we see significant suppression of GeO_2 formation with a decrease in oxygen pressure of only two orders of magnitude. Future experiments are already planned to oxidize $Si_{0.60}Ge_{0.40}(001)$ at $T_{ox} = 300°C$ and $P_{O2} = 10^{-4}$ mbar in attempt to find the critical pressure at which the replacement reaction will dominate.

These studies parsing out kinetic information will rely on the ability to determine using APXPS experimental data the concentration of Ge in the oxide and alloy, as well as the thickness of the oxide. For now, this requires validation of SESSA's ability to determine this information

146

by comparison to experimental intensity ratios. The estimated oxide thicknesses of 33 Å at P_{O2} = 1 mbar and 28 Å at P_{O2} = 0.01 mbar can be verified with ellipsometry as the samples are diced from a polished wafer. High-resolution transmission electron microscopy (HRTEM) can be used to as a second source of data for these measurements. In this manner, I_{O1s} / I_{Si0} and I_{O1s} / I_{Ge0} experimental and simulated intensity ratios can be correlated to an experimental oxide thickness. As the experimental O 1s intensity has had the $GeL_3M_{23}M_{23}$ Auger contribution subtracted, verifying the oxide thickness would yield insight into the accuracy of (or inaccuracy of) the correction method. With an expected suboxide interface of 1-2 ML (3-6 Å), experimental measurements should yield larger oxide thicknesses than predicted by SESSA. The difference in thickness should account for the fact that SESSA I_{O1s} / I_{Si0} and I_{O1s} / I_{Ge0} ratios have assumed the oxide consists of only the 4+ oxidation state, which will have a high oxygen density per unit thickness when compared to the suboxide region. Therefore, the ratios should match experimental ratios at some thickness thinner than the actual thickness. Provided the magnitude of the difference is within a reasonable range, it can be attributed to suboxide contributions to the O 1s intensity.

For simplicity in modeling of the $Si_{0.60}Ge_{0.40}$(001) oxide in SESSA, it was assumed that the Ge fraction in the oxide is constant. This assumption was based on Figure 4.4, which indicates that after an initial transient regime the concentration in the alloy reaches a quasi-steady state which persists throughout a good portion of oxide growth. However, it would nevertheless be interesting to observe whether the top most layers of oxide are enriched in Si compared to layers closer to the interface as Figure 4.4 suggests. Oxide composition profiles could be obtained using angle resolved XPS (ARXPS) and sputter depth profiling techniques. A compositional profile of the oxide could be obtained by transferring the sample to the UHV cell

(NAP cell is fixed at $\theta = 0°$) and collecting spectra at varying angles at high emission angle to maximize surface sensitivity. In this manner atomic percent can be calculated at different sampling depths to obtain a compositional profile. There is some uncertainly involved in this, as it has been shown that Si 2p and Ge 3d photoemission intensities can have a complex dependence on emission angle. Moreover, with Al Kα X-ray excitation the IMFP of Si 2p and Ge 3d photoelectrons is around 3 nm so glancing angles relative to surface normal would have to be used to sample predominantly from the oxide. The oxidized sample could be transferred to the PHI instrument to use lower energy Mg-Kα dual anode X-ray source (hν = 1253.6 eV), but transfer would expose the sample to carbon contamination. Sputter depth profiling of the oxide is also made difficult by the thin oxide. The sputter rate would have to be carefully controlled to sputter away only a few monolayers of oxide at a time. Even then, surface sensitivity would have to be maximized (high emission angle) to observe the small changes in atomic percent. Complicating this method is the expected higher sputter yield of Ge in the oxide, which could cause an apparent enrichment of Si in the oxide caused by preferential sputtering of Ge. With the sources of uncertainty considered for each method, angle resolved XPS would likely yield the most reliable results as changes in Ge 3d and Si 2p intensity with emission angle is documented in literature.

In Chapter 3 Figure 3.6, it was shown that diffusion in $Si_{0.60}Ge_{0.40}(001)$ alloy appears to be active even at low anneal temperatures with Ge segregating to the surface. In future research it would be interesting to characterize the extent of this segregation and how it affects the composition of the alloy. Minimization of free energy in a solid solution would suggest that Ge should segregate to the surface [7] until an energy minimum at a Ge content of 50% [8]. It would be useful to determine then if all $Si_{1-x}Ge_x$ alloys have 50% Ge content at the interface after

annealing, and if the thickness of the segregation region is dependent on Ge content in the alloy and temperature. Vacancy nearest neighbor research suggests a large increase in interdiffusion at Ge content of 50% and above [9], suggesting the transition from segregation region to bulk alloy could be quite abrupt thus its thickness could be accurately defined. For $Si_{0.60}Ge_{0.40}(001)$ specifically, it would be quite useful to accurately characterize the segregation region so the alloy can be properly modeled in SESSA. Scanning transmission electron microscopy energy dispersive X-ray spectroscopy (STEM-EDS) could be used to verify the compositional profile in the oxide determined by ARXPS, as well as the thickness of the germanium rich segregation layer.

5.3   Reference

[1]   M. A. Rabie, Y. M. Haddara, and J. Carette, "A kinetic model for the oxidation of silicon germanium alloys," *J. Appl. Phys.*, vol. 98, no. 7, p. 074904, Oct. 2005.

[2]   B. E. Deal and A. S. Grove, "General relationship for the thermal oxidation of silicon," *J. Appl. Phys.*, vol. 36, no. 12, pp. 3770–3778, 1965.

[3]   G. Iovino, S. Agnello, F. M. Gelardi, and R. Boscaino, "Diffusive equilibrium properties of O_2 in amorphous SiO_2 nanoparticles probed via dependence of concentration on size and pressure," *J. Phys. Chem. C*, vol. 118, no. 31, pp. 18044–18050, 2014.

[4]   Y. Enta *et al.*, "Real-time observation of the dry oxidation of the Si(100) surface with ambient pressure x-ray photoelectron spectroscopy," *Appl. Phys. Lett.*, vol. 92, no. 1, p. 012110, 2008.

[5]   P. E. Hellberg, S. L. Zhang, F. M. D'Heurle, and C. S. Petersson, "Oxidation of silicon-germanium alloys. II. A mathematical model," *J. Appl. Phys.*, vol. 82, no. 11, pp. 5779–5787, 1997.

[6]   W. Song and A. Toriumi, "Study of SiGe oxidation kinetics for preferential SiO2 formation under a low O2 pressure condition," *J. Appl. Phys.*, vol. 122, no. 18, pp. 185301–185307, Nov. 2017.

[7]   J. Nyéki, C. Girardeaux, G. Erdélyi, A. Rolland, and J. Bernardini, "Equilibrium surface segregation enthalpy of Ge in concentrated amorphous SiGe alloys," *Appl. Surf. Sci.*, vol. 212–213, pp. 244–248, May 2003.

[8]   T. David *et al.*, "Kinetics and Energetics of Ge Condensation in SiGe Oxidation," *J. Phys. Chem. C*, vol. 119, no. 43, pp. 24606–24613, 2015.

[9]   P. Venezuela, G. M. Dalpian, A. J. R. da Silva, and A. Fazzio, "Vacancy-mediated diffusion in disordered alloys: Ge self-diffusion in Si$_{1-x}$Ge$_x$," *Phys. Rev. B*, vol. 65, no. 19, pp. 193306–193309, May 2002.

Bibliography

[1]   H. C. Torrey and C. A. Whitmer, "Crystal Rectifiers," in *MIT Radiation Lab Series*, First., S. A. Goudsmit, L. B. Linford, J. L. Lawson, and A. M. Stone, Eds. New York: McGraw-Hill Book Company, 1948.

[2]   C. Kittel, *Introduction to Solid State Physics*, 8th ed. Hoboken, New Jersey, New Jersey: John Wiley & Sons, Inc., 2005.

[3]   W. D. J. Callister, *Materials Science and Engineering: An Introduction*, 7th ed. New York, NY, NY: John Wiley & Sons, Inc., 2007.

[4]   W. Shockley, "Circuit element utilizing semiconductive material," US2569347A, 1951.

[5]   P. Valizadeh, *Field effect transistors : A comprehensive overview : From basic concepts to novel technologies*. Hoboken, New Jersey: John Wiley & Sons, Inc., 2016.

[6]   Z. Huda and R. Bulpett, *Materials science and design for engineers*. Enfield, New Hampshire: Trans Tech Publications, 2012.

[7]   T. F. Schubert and E. M. Kim, *Fundamentals of Electronics*. 2015.

[8]   R. Lewis, *Solid-State Devices and Applications*. Kent: Elsevier Science & Technology, 2013.

[9]   C. H. Chenming, *Modern Semiconductor Devices for Integrated Circuits*, 1st ed. Pearson, 2009.

[10]   H. Kroemer, "Theory of a Wide-Gap Emitter for Transistors," *Proc. IRE*, vol. 45, no. 11, pp. 1535–1537, 1957.

[11]   H. Kroemer, "Heterostructure Bipolar Transistors and Integrated Circuits," *Proc. IEEE*, vol. 70, no. 1, pp. 13–25, 1982.

[12]   S. Brojdo, T. J. Riley, and G. T. Wright, "The heterojunction transistor and the space-charge-limited triode," *Br. J. Appl. Phys.*, vol. 16, no. 2, pp. 133–136, 1965.

[13]   D. K. Jadus and D. L. Feucht, "The Realization of a GaAs-Ge Wide Band Gap Emitter Transistor," *IEEE Trans. Electron Devices*, vol. 16, no. 1, pp. 102–107, 1969.

[14]   A. G. Milnes, *Heterojunctions and metal-semiconductor junctions*. New York: Academic Press, 2012.

[15]   F. Schäffler, "High-mobility Si and Ge structures," *Semicond. Sci. Technol.*, vol. 12, no.

12, pp. 1515–1549, 1999.

[16] G. L. Patton, S. S. Iyer, S. L. Delage, S. Tiwari, and J. M. C. Stork, "Silicon-germanium base heterojunction bipolar transistors by molecular beam epitaxy," *IEEE Electron Device Lett.*, vol. 9, no. 4, pp. 165–167, Apr. 1988.

[17] G. L. Patton, J. H. Comfort, B. S. Meyerson, and F. Emmanuel, "SiGe-Base Heterojunction Bipolar Transistors," *IEEE Electron Device Lett.*, vol. 1, no. 4, pp. 171–173, 1990.

[18] J. S. Dunn *et al.*, "Foundation of rf CMOS and SiGe BiCMOS technologies," *IBM J. Res. Dev.*, vol. 47, no. 2.3, pp. 101–138, 2003.

[19] P. Venezuela, G. M. Dalpian, A. J. R. da Silva, and A. Fazzio, "Vacancy-mediated diffusion in disordered alloys: Ge self-diffusion in $Si_{1-x}Ge_x$," *Phys. Rev. B*, vol. 65, no. 19, pp. 193306–193309, May 2002.

[20] A. Strohm, T. Voss, W. Frank, J. Räisänen, and M. Dietrich, "Self-diffusion of ^{71}Ge in Si-Ge," *Phys. B Condens. Matter*, vol. 308–310, pp. 542–545, 2001.

[21] W. G. Oldham and A. G. Milnes, "Interface states in abrupt semiconductor heterojunctions," *Solid. State. Electron.*, vol. 7, no. 2, pp. 153–165, Feb. 1964.

[22] H. Rücker and B. Heinemann, "High-performance SiGe HBTs for next generation BiCMOS technology," *Semicond. Sci. Technol.*, vol. 33, no. 11, pp. 114003–114008, Nov. 2018.

[23] F. Rozé *et al.*, "Oxidation kinetics of Si and SiGe by dry rapid thermal oxidation, in-situ steam generation oxidation and dry furnace oxidation," *J. Appl. Phys.*, vol. 121, no. 24, 2017.

[24] L. Fauquier *et al.*, "Benefits of XPS nanocharacterization for process development and industrial control of thin SiGe channel layers in advanced CMOS technologies," *Mater. Sci. Semicond. Process.*, vol. 70, pp. 105–110, Nov. 2017.

[25] W. Song and A. Toriumi, "Study of SiGe oxidation kinetics for preferential SiO_2 formation under a low O_2 pressure condition," *J. Appl. Phys.*, vol. 122, no. 18, pp. 185301–185307, Nov. 2017.

[26] D. C. Paine, C. Caragianis, and a. F. Schwartzman, "Oxidation of Si1-xGex alloys at atmospheric and elevated pressure," *J. Appl. Phys.*, vol. 70, no. 9, pp. 5076–5084, 1991.

[27] B. K. Boksteen, J. Schmitz, and R. J. E. Hueting, "Interface Trap Density Estimation in FinFETs Using the gm/ID Method in the Subthreshold Regime," *IEEE Trans. Electron Devices*, vol. 63, no. 5, pp. 1814–1820, 2016.

[28] B. E. Deal and A. S. Grove, "General relationship for the thermal oxidation of silicon," *J. Appl. Phys.*, vol. 36, no. 12, pp. 3770–3778, 1965.

[29] H. Z. Massoud, "Thermal Oxidation of Silicon in Dry Oxygen Growth-Rate Enhancement in the Thin Regime," *J. Electrochem. Soc.*, vol. 132, no. 11, pp. 2685–2693, 1985.

[30] W. A. Tiller, "On the Kinetics of the Thermal Oxidation of Silicon," *J. Electrochem. Soc.*, vol. 127, no. 3, p. 619, 1980.

[31] A. G. Revesz and R. J. Evans, "Kinetics and mechanism of thermal oxidation of silicon with special emphasis on impurity effects," *J. Phys. Chem. Solids*, vol. 30, no. 3, pp. 551–564, Mar. 1969.

[32] J. Blanc, "A revised model for the oxidation of Si by oxygen," *Appl. Phys. Lett.*, vol. 33, no. 5, pp. 424–426, 1978.

[33] S. M. Hu, "New oxide growth law and the thermal oxidation of silicon," *Appl. Phys. Lett.*, vol. 42, no. 10, pp. 872–874, 1983.

[34] H. Wong and Y. C. Cheng, "A new growth model of thin silicon oxide in dry oxygen," *J. Appl. Phys.*, vol. 64, no. 2, pp. 893–897, 1988.

[35] T. David *et al.*, "Kinetics and Energetics of Ge Condensation in SiGe Oxidation," *J. Phys. Chem. C*, vol. 119, no. 43, pp. 24606–24613, 2015.

[36] M. A. Rabie, Y. M. Haddara, and J. Carette, "A kinetic model for the oxidation of silicon germanium alloys," *J. Appl. Phys.*, vol. 98, no. 7, pp. 074904–074913, Oct. 2005.

[37] P. Laitinen *et al.*, "Self-Diffusion of ^{31}Si and ^{71}Ge in Relaxed $Si_{0.20}Ge_{0.80}$ Layers," *Phys. Rev. Lett.*, vol. 89, no. 8, p. 085902, 2002.

[38] F. K. LeGoues, R. Rosenberg, and B. S. Meyerson, "Kinetics and mechanism of oxidation of SiGe: Dry versus wet oxidation," *Appl. Phys. Lett.*, vol. 54, no. 7, pp. 644–646, 1989.

[39] M. Spadafora *et al.*, "Oxidation rate enhancement of SiGe epitaxial films oxidized in dry ambient," *Appl. Phys. Lett.*, vol. 83, no. 18, pp. 3713–3715, 2003.

[40] F. K. LeGoues, R. Rosenberg, T. Nguyen, F. Himpsel, and B. S. Meyerson, "Oxidation studies of SiGe," *J. Appl. Phys.*, vol. 65, no. 4, pp. 1724–1728, 1989.

[41] C. Tételin, X. Wallart, J. P. Nys, L. Vescan, and D. J. Gravesteijn, "Kinetics and mechanism of low temperature atomic oxygen-assisted oxidation of SiGe layers," *J. Appl. Phys.*, vol. 83, no. 5, pp. 2842–2846, 1998.

[42] O. W. Holland, C. W. White, and D. Fathy, "Novel oxidation process in Ge^+ implanted Si and its effect on oxidation kinetics," *Appl. Phys. Lett.*, vol. 51, no. 7, pp. 520–522, 1987.

[43] J. H. Oh *et al.*, "Chemical structure of the ultrathin SiO_2/Si(100) interface: An angle-resolved Si 2p photoemission study," *Phys. Rev. B*, vol. 63, no. 20, p. 205310, 2001.

[44] P. J. Grunthaner, M. H. Hecht, F. J. Grunthaner, and N. M. Johnson, "The localization and crystallographic dependence of Si suboxide species at the SiO_2/Si interface," *J. Appl. Phys.*, vol. 61, no. 2, pp. 629–638, 1987.

[45] G. Hollinger and F. J. Himpsel, "Probing the transition layer at the SiO_2-Si interface using core level photoemission," *Appl. Phys. Lett.*, vol. 44, no. 1, pp. 93–95, 1984.

[46] F. J. Grunthaner, P. J. Grunthaner, R. P. Vasquez, B. F. Lewis, J. Maserjian, and A. Madhukar, "High-Resolution X-Ray Photoelectron Spectroscopy as a Probe of Local

Atomic Structure: Application to Amorphous SiO_2 and the Si-SiO$_2$ Interface," *Phys. Rev. Lett.*, vol. 43, no. 22, pp. 1683–1686, Nov. 1979.

[47]   F. J. Himpsel, F. R. McFeely, A. Taleb-Ibrahimi, J. A. Yarmoff, and G. Hollinger, "Microscopic structure of the SiO_2/Si interface," *Phys. Rev. B*, vol. 38, no. 9, pp. 6084–6096, 1988.

[48]   D. Schmeisser *et al.*, "Surface oxidation states of germanium," *Surf. Sci.*, vol. 172, no. 2, pp. 455–465, Jul. 1986.

[49]   A. Molle, M. N. K. Bhuiyan, G. Tallarida, and M. Fanciulli, "In situ chemical and structural investigations of the oxidation of Ge(001) substrates by atomic oxygen," *Appl. Phys. Lett.*, vol. 89, no. 8, pp. 083504–083506, Aug. 2006.

[50]   K. Prabhakaran, F. Maeda, Y. Watanabe, and T. Ogino, "Distinctly different thermal decomposition pathways of ultrathin oxide layer on Ge and Si surfaces," *Appl. Phys. Lett.*, vol. 76, no. 16, pp. 2244–2246, 2000.

[51]   J. M. Madsen, Z. Cui, and C. G. Takoudis, "Low temperature oxidation of SiGe in ozone: Ultrathin oxides," *J. Appl. Phys.*, vol. 87, no. 4, pp. 2046–2051, Feb. 2000.

[52]   Z. H. Lu, M. J. Graham, D. T. Jiang, and K. H. Tan, "SiO_2/Si(100) interface studied by Al Kα x-ray and synchrotron radiation photoelectron spectroscopy," *Appl. Phys. Lett.*, vol. 63, no. 21, pp. 2941–2943, 1993.

[53]   S. J. Kilpatrick, R. J. Jaccodine, and P. E. Thompson, "Experimental study of the oxidation of silicon germanium alloys," *J. Appl. Phys.*, vol. 93, no. 8, pp. 4896–4901, 2003.

[54]   S. J. Kilpatrick, R. J. Jaccodine, and P. E. Thompson, "A diffusional model for the oxidation behavior of $Si_{1-x}Ge_x$ alloys," *J. Appl. Phys.*, vol. 81, no. 12, pp. 8018–8028, 1997.

[55]   M. K. Bera *et al.*, "Rapid thermal oxidation of Ge-rich $Si_{1-x}Ge_x$ heterolayers," *J. Vac. Sci. Technol. A Vacuum, Surfaces, Film.*, vol. 24, no. 1, pp. 84–90, 2006.

[56]   A. Agarwal, J. K. Patterson, J. E. Greene, and A. Rockett, "Ultraviolet ozone induced oxidation of epitaxial $Si_{1-x}Ge_x$(111)," *Appl. Phys. Lett.*, vol. 63, no. 4, pp. 518–520, 1993.

[57]   A. B. Christie, "X-ray photoelectron spectroscopy," in *Methods of Surface Analysis*, J. M. Walls, Ed. Cambridge, UK: Cambridge University Press, 1989, pp. 127–168.

[58]   K. W. Kolasinski, *Surface Science: Foundations of Catalysis and Nanoscience*, 3rd ed. New York, NY: John Wiley & Sons, Inc., 2012.

[59]   Y. F. Chen, C. M. Kwei, and C. J. Tung, "Electron inelastic mean free paths versus attenuation lengths in solids," *J. Phys. D. Appl. Phys.*, vol. 25, no. 2, pp. 262–268, 1992.

[60]   M. P. Seah and W. A. Dench, "Quantitative electron spectroscopy of surfaces: A standard data base for electron inelastic mean free paths in solids," *Surf. Interface Anal.*, vol. 1, no. 1, pp. 2–11, Feb. 1979.

[61] A. Jablonski, "Effects of Auger electron elastic scattering in quantitative AES," *Surf. Sci.*, vol. 188, no. 1–2, pp. 164–180, 1987.

[62] M. P. Seah and S. J. Spencer, "Ultrathin SiO_2 on Si II . Issues in quantification of the oxide thickness," pp. 640–652, 2002.

[63] P. J. Cumpson and M. P. Seah, "Elastic Scattering Corrections in AES and XPS. II. Estimating Attenuation Lengths and Conditions Required for their Valid Use in Overlayer/Substrate Experiments," *Surf. Interface Anal.*, vol. 25, no. 6, pp. 430–446, Jun. 1997.

[64] D. Briggs and J. C. Riviere, "Spectral Interpretation," in *Practical Surface Analysis by Auger and X-ray Photoelectron Spectroscopy*, D. Briggs and M. P. Seah, Eds. New York, NY: John Wiley & Sons, Inc., 1983, pp. 87–139.

[65] C. S. Fadley, "Basic Concepts of X-ray Photoelectron Spectroscopy," in *Electron Spectroscopy: Theory, Techniques, and Applications*, vol. 2, C. R. Brundle and A. D. Baker, Eds. New York, NY: Academic Press, 1978, pp. 1–155.

[66] J. C. Riviere, "Instrumentation," in *Practical Surface Analysis by Auger and X-ray Photoelectron Spectroscopy*, D. Briggs and M. P. Seah, Eds. New York, NY: John Wiley & Sons, Inc., 1983, pp. 17–85.

[67] F. Reniers and C. Tewell, "New improvements in energy and spatial (x, y, z) resolution in AES and XPS applications," *J. Electron Spectros. Relat. Phenomena*, vol. 142, no. 1, pp. 1–25, 2005.

[68] A. R. Head and H. Bluhm, "Ambient Pressure X-Ray Photoelectron Spectroscopy," in *Reference Module in Chemistry, Molecular Sciences and Chemical Engineering*, vol. 27, no. 2, pp. 14–23, 2016.

[69] E. Atanassova and A. Paskaleva, "Influence of the rapid thermal annealing in vacuum on the XPS characteristics of thin SiO_2," *Appl. Surf. Sci.*, vol. 103, no. 4, pp. 359–367, 1996.

[70] L. Trotochaud, A. R. Head, O. Karslioğlu, L. Kyhl, and H. Bluhm, "Ambient pressure photoelectron spectroscopy: Practical considerations and experimental frontiers," *J. Phys. Condens. Matter*, vol. 29, no. 5, p. 053002, 2017.

[71] H. Siegbahn and K. Siegbahn, "ESCA applied to liquids," *J. Electron Spectros. Relat. Phenomena*, vol. 2, no. 3, pp. 319–325, Jan. 1973.

[72] M. A. Kelly, M. L. Shek, P. Pianetta, T. M. Gür, and M. R. Beasley, "In situ x-ray photoelectron spectroscopy for thin film synthesis monitoring," *J. Vac. Sci. Technol. A Vacuum, Surfaces, Film.*, vol. 19, no. 5, pp. 2127–2133, Sep. 2001.

[73] D. F. Ogletree, H. Bluhm, G. Lebedev, C. S. Fadley, Z. Hussain, and M. Salmeron, "A differentially pumped electrostatic lens system for photoemission studies in the millibar range," *Rev. Sci. Instrum.*, vol. 73, no. 11, p. 3872, 2002.

[74] H. Bluhm *et al.*, "Soft X-ray microscopy and spectroscopy at the molecular environmental science beamline at the Advanced Light Source," *J. Electron Spectros. Relat. Phenomena*, vol. 150, no. 2–3, pp. 86–104, Feb. 2006.

[75]   H. Bluhm, "Photoelectron spectroscopy of surfaces under humid conditions," *J. Electron Spectros. Relat. Phenomena*, vol. 177, no. 2–3, pp. 71–84, 2010.

[76]   M. Salmeron and R. Schlögl, "Ambient pressure photoelectron spectroscopy: A new tool for surface science and nanotechnology," *Surf. Sci. Rep.*, vol. 63, no. 4, pp. 169–199, 2008.

[77]   M. T. Anthony, "Spectrometer Calibration," in *Practical Surface Analysis by Auger and X-ray Photoelectron Spectroscopy*, D. Briggs and M. P. Seah, Eds. New York, NY: John Wiley & Sons, Inc., 1983, pp. 429–435.

[78]   M. Schmid, H. P. Steinrück, and J. M. Gottfried, "A new asymmetric Pseudo-Voigt function for more efficient fitting of XPS lines," *Surf. Interface Anal.*, vol. 46, no. 8, pp. 505–511, 2014.

[79]   S. Hüfner, *Photoelectron Spectroscopy - Principles and Applications*, 3rd ed. Berlin Heidelberg: Springer-Verlag, 2010.

[80]   S. M. Goldberg, C. S. Fadley, and S. Kono, "Photoionization cross-sections for atomic orbitals with random and fixed spatial orientation," *J. Electron Spectros. Relat. Phenomena*, vol. 21, no. 4, pp. 285–363, 1981.

[81]   R. F. Reilman, A. Msezane, and S. T. Manson, "Relative intensities in photoelectron spectroscopy of atoms and molecules," *J. Electron Spectros. Relat. Phenomena*, vol. 8, no. 5, pp. 389–394, 1976.

[82]   M. P. Seah, "Quantification of AES and XPS," in *Practical Surface Analysis by Auger and X-ray Photoelectron Spectroscopy*, D. Briggs and M. P. Seah, Eds. New York, NY: John Wiley & Sons, Inc., 1983, pp. 181–216.

[83]   J. F. Moulder, W. F. Stickle, P. E. Sobol, and K. D. Bomben, *Handbook of X-Ray Photoelectron Spectroscopy*. Eden Prairie, MN: Perkin-Elmer Corporation, 1992.

[84]   V. Craciun, I. W. Boyd, B. Hutton, and D. Williams, "Characteristics of dielectric layers grown on Ge by low temperature vacuum ultraviolet-assisted oxidation," *Appl. Phys. Lett.*, vol. 75, no. 9, pp. 1261–1263, 1999.

[85]   M. Rossi *et al.*, "In situ observation of wet oxidation kinetics on Si(100) via ambient pressure x-ray photoemission spectroscopy," *J. Appl. Phys.*, vol. 103, no. 4, 2008.

[86]   C. S. Fadley, "Angle-resolved x-ray photoelectron spectroscopy," *Prog. Surf. Sci.*, vol. 16, no. 3, pp. 275–388, 1984.

[87]   B. Nisol and F. Reniers, "Challenges in the characterization of plasma polymers using XPS," *J. Electron Spectros. Relat. Phenomena*, vol. 200, pp. 311–331, 2015.

[88]   A. V. Naumkin, A. Kraut-Vass, S. Gaarenstroom, and C. J. Powell, "NIST X-ray Photoelectron Spectroscopy Database," 2012.

[89]   U. Gelius, "Binding energies and chemical shifts in ESCA," *Phys. Scr.*, vol. 9, no. 3, pp. 133–147, 1974.

[90] G. Beamson and D. Briggs, "High resolution monochromated x-ray photoelectron spectroscopy of organic polymers: A comparison between solid state data for organic polymers and gas phase data for small molecules," *Mol. Phys.*, vol. 76, no. 4, pp. 919–936, 1992.

[91] W. S. M. Werner, "Electron transport in solids for quantitative surface analysis," *Surf. Interface Anal.*, vol. 31, no. 3, pp. 141–176, 2001.

[92] W. S. M. Werner and P. Schattschneider, "On the energy dissipation process in incoherent electron scattering," *J. Electron Spectros. Relat. Phenomena*, vol. 143, no. 2–3 SPEC. ISS., pp. 65–80, 2005.

[93] N. Fairley, "CasaXPS." Neal Fairley.

[94] B. Singh, A. Diwan, V. Jain, A. Herrera-Gomez, J. Terry, and M. R. Linford, "Uniqueness plots: A simple graphical tool for identifying poor peak fits in X-ray photoelectron spectroscopy," *Appl. Surf. Sci.*, vol. 387, pp. 155–162, 2016.

[95] P. H. Citrin, P. Eisenberger, and D. R. Hamann, "Phonon broadening of x-ray photoemission linewidths," *Phys. Rev. Lett.*, vol. 33, no. 16, pp. 965–969, 1974.

[96] D. E. Starr, Z. Liu, M. Hävecker, A. Knop-Gericke, and H. Bluhm, "Investigation of solid/vapor interfaces using ambient pressure X-ray photoelectron spectroscopy," *Chem. Soc. Rev.*, vol. 42, no. 13, pp. 5833–5857, 2013.

[97] V. V. Kaichev, I. P. Prosvirin, V. I. Bukhtiyarov, H. Unterhalt, G. Rupprechter, and H. J. Freund, "High-pressure studies of CO adsorption on Pd(111) by X-ray photoelectron spectroscopy and sum-frequency generation," *J. Phys. Chem. B*, vol. 107, no. 15, pp. 3522–3527, 2003.

[98] G. Ketteler, D. F. Ogletree, H. Bluhm, H. Liu, E. L. D. Hebenstreit, and M. Salmeron, "In situ spectroscopic study of the oxidation and reduction of Pd(111)," *J. Am. Chem. Soc.*, vol. 127, no. 51, pp. 18269–18273, 2005.

[99] S. Günther, L. Zhou, M. Hävecker, E. Kleimenov, R. Schlögl, and R. Imbihl, "Adsorbate coverages and surface reactivity in methanol oxidation over Cu(110): An in situ photoelectron spectroscopy study," vol. 125, no. 11, p. 114709, 2017.

[100] K. Andersson *et al.*, "Bridging the pressure gap in water and hydroxyl chemistry on metal surfaces: The Cu(110) case," *J. Phys. Chem. C*, vol. 111, no. 39, pp. 14493–14499, 2007.

[101] J. Zhang, X. Liu, R. Blume, A. Zhang, R. Schlögl, and S. S. Dang, "Surface-modified carbon nanotubes catalyze oxidative dehydrogenation of n-butane," *Science*, vol. 322, no. 5898, pp. 73–77, 2008.

[102] A. Caballero, J. P. Holgado, V. M. Gonzalez-Delacruz, S. E. Habas, T. Herranz, and M. Salmeron, "In situ spectroscopic detection of SMSI effect in a Ni/CeO$_2$ system: Hydrogen-induced burial and dig out of metallic nickel," *Chem. Commun.*, vol. 46, no. 7, pp. 1097–1099, 2010.

[103] C. Zhang *et al.*, "Measuring fundamental properties in operating solid oxide electrochemical cells by using in situ X-ray photoelectron spectroscopy," *Nat. Mater.*, vol.

9, no. 11, pp. 944–949, 2010.

[104] R. S. Weatherup *et al.*, "On the mechanisms of Ni-catalysed graphene chemical vapour deposition," *ChemPhysChem*, vol. 13, no. 10, pp. 2544–2549, 2012.

[105] L. L. Patera *et al.*, "In situ observations of the atomistic mechanisms of Ni catalyzed low temperature graphene growth," *ACS Nano*, vol. 7, no. 9, pp. 7901–7912, 2013.

[106] E. Graìšnäs *et al.*, "CO intercalation of graphene on Ir(111) in the millibar regime," *J. Phys. Chem. C*, vol. 117, no. 32, pp. 16438–16447, 2013.

[107] M. Faubel, B. Steiner, and J. P. Toennies, "Photoelectron spectroscopy of liquid water, some alcohols, and pure nonane in free micro jets," *J. Chem. Phys.*, vol. 106, no. 22, pp. 9013–9031, 1997.

[108] M. A. Brown *et al.*, "Electronic structure of sub-10 nm colloidal silica nanoparticles measured by in situ photoelectron spectroscopy at the aqueous-solid interface," *Phys. Chem. Chem. Phys.*, vol. 13, no. 28, pp. 12720–12723, 2011.

[109] E. Long, A. Azarov, F. Klow, A. Galeckas, A. Yu Kuznetsov, and S. Diplas, "Ge redistribution in SiO_2/SiGe structures under thermal oxidation: Dynamics and predictions," *J. Appl. Phys.*, vol. 111, no. 2, 2012.

[110] T. Tezuka, N. Sugiyama, T. Mizuno, M. Suzuki, and S. I. Takagi, "A novel fabrication technique of ultrathin and relaxed SiGe buffer layers with high Ge fraction for sub-100 nm strained silicon-on-insulator MOSFETs," *Japanese J. Appl. Physics, Part 1 Regul. Pap. Short Notes Rev. Pap.*, vol. 40, no. 4 B, pp. 2866–2874, 2001.

[111] C.-T. Chang and A. Toriumi, "Preferential oxidation of Si in SiGe for shaping Ge-rich SiGe gate stacks," in *2015 IEEE International Electron Devices Meeting (IEDM)*, 2015, p. 21.5.1-21.5.4.

[112] M. Rossi *et al.*, "In situ observation of wet oxidation kinetics on Si(100) via ambient pressure x-ray photoemission spectroscopy," *J. Appl. Phys.*, vol. 103, no. 4, p. 044104, Feb. 2008.

[113] Y. Enta *et al.*, "Real-time observation of the dry oxidation of the Si(100) surface with ambient pressure x-ray photoelectron spectroscopy," *Appl. Phys. Lett.*, vol. 92, no. 1, p. 012110, 2008.

[114] S. W. Park *et al.*, "Combined wet and dry cleaning of SiGe(001)," *J. Vac. Sci. Technol. A Vacuum, Surfaces, Film.*, vol. 33, no. 4, p. 041403, 2015.

[115] K. Prabhakaran and T. Ogino, "Oxidation of Ge (100) and Ge (111) surfaces: an UPS and XPS study," *Surf. Sci.*, vol. 325, pp. 263–271, 1995.

[116] K. Prabhakaran and T. Ogino, "Oxidation of Ge(100) and Ge(111) surfaces: an UPS and XPS study," *Surf. Sci.*, vol. 325, no. 3, pp. 263–271, 1995.

[117] S. Rivillon, Y. J. Chabal, F. Amy, and A. Kahn, "Hydrogen passivation of germanium (100) surface using wet chemical preparation," *Appl. Phys. Lett.*, vol. 87, no. 25, pp. 1–3, 2005.

[118] S. Sun, Y. Sun, Z. Liu, D. I. Lee, S. Peterson, and P. Pianetta, "Surface termination and roughness of Ge(100) cleaned by HF and HCl solutions," *Appl. Phys. Lett.*, vol. 88, no. 2, pp. 1–3, 2006.

[119] A. Ohta, T. Fujioka, H. Murakami, S. Higashi, and S. Miyazaki, "X-ray photoelectron spectroscopy study of interfacial reactions between metal and ultrathin Ge oxide," *Jpn. J. Appl. Phys.*, vol. 50, no. 10 PART 2, pp. 3–8, 2011.

[120] J. M. Hill, D. G. Royce, C. S. Fadley, L. F. Wagner, and F. J. Grunthaner, "Properties of oxidized silicon as determined by angular-dependent X-ray photoelectron spectroscopy," *Chem. Phys. Lett.*, vol. 44, no. 2, pp. 225–231, Dec. 1976.

[121] M. Matsui, H. Murakami, T. Fujioka, A. Ohta, S. Higashi, and S. Miyazaki, "Characterization of chemical bonding features at metal/GeO_2 Interfaces by X-ray photoelectron spectroscopy," *Microelectron. Eng.*, vol. 88, no. 7, pp. 1549–1552, 2011.

[122] W. Smekal, W. S. M. Werner, and C. J. Powell, "Simulation of electron spectra for surface analysis (SESSA): a novel software tool for quantitative Auger-electron spectroscopy and X-ray photoelectron spectroscopy," pp. 1059–1067, 2005.

[123] J. P. Dismukes, L. Ekstrom, and R. J. Paff, "Lattice Parameter and Density in Germanium-Silicon Alloys," *J. Phys. Chem.*, vol. 68, no. 10, pp. 3021–3027, 1964.

[124] N. M. Ravindra, R. A. Weeks, and D. L. Kinser, "Optical properties of GeO_2," *Phys. Rev. B*, vol. 36, no. 11, pp. 6132–6134, 1987.

[125] S. Hofmann, "Depth Profiling," in *Practical Surface Analysis by Auger and X-ray Photoelectron Spectroscopy*, D. Briggs and M. P. Seah, Eds. New York, NY: John Wiley & Sons, Inc., 1983, pp. 141–179.

[126] F. J. Grunthaner and J. Maserjian, "Experimental Observations of the Chemistry of the SiO2/Si Interface," *IEEE Trans. Nucl. Sci.*, vol. 24, no. 6, pp. 2108–2112, Dec. 1977.

[127] D. Mori *et al.*, "Comparative study of GeO_2/Ge and SiO_2/Si structures on anomalous charging of oxide films upon water adsorption revealed by ambient-pressure X-ray photoelectron spectroscopy," *J. Appl. Phys.*, vol. 120, no. 9, 2016.

[128] J. M. C. Thornton and R. H. Williams, "A photoemission study of passivated silicon surfaces produced by etching in solutions of HF," *Semicond. Sci. Technol.*, vol. 4, no. 10, pp. 847–851, 1989.

[129] G. Lucovsky, S. S. Chao, J. E. Tyler, and G. De Maggio, "An XPS study of sputtered a-Si,Ge alloys," *J. Vac. Sci. Technol.*, vol. 21, no. 3, pp. 838–844, 1982.

[130] Z. H. Lu, "Air-stable Cl-terminated Ge(111)," *Appl. Phys. Lett.*, vol. 520, no. October 2018, p. 520, 1995.

[131] K. Ikeda, S. Imai, and M. Matsumura, "Atomic layer etching of germanium," *Appl. Surf. Sci.*, vol. 112, pp. 87–91, Mar. 1997.

[132] M. S. Carroll, J. C. Sturm, and M. Yang, "Low-Temperature Preparation of Oxygen- and Carbon-Free Silicon and Silicon-Germanium Surfaces for Silicon and Silicon-Germanium

Epitaxial Growth by Rapid Thermal Chemical Vapor Deposition," *J. Electrochem. Soc.*, vol. 147, no. 12, pp. 4652–4659, 2000.

[133] W. F. Zhang, T. Nishimula, K. Nagashio, K. Kita, and A. Toriumi, "Conduction band offset at GeO_2/Ge interface determined by internal photoemission and charge-corrected x-ray photoelectron spectroscopies," *Appl. Phys. Lett.*, vol. 102, no. 10, pp. 2–6, 2013.

[134] P. W. Loscutoff and S. F. Bent, "REACTIVITY OF THE GERMANIUM SURFACE: Chemical Passivation and Functionalization," *Annu. Rev. Phys. Chem.*, vol. 57, no. 1, pp. 467–495, 2006.

[135] I. Ohdomari, H. Akatsu, Y. Yamakoshi, and K. Kishimoto, "Study of the interfacial structure between Si(100) and thermally grown SiO_2 using a ball-and-spoke model," *J. Appl. Phys.*, vol. 62, no. 9, p. 3751, 1987.

[136] C. Mastail *et al.*, "Oxidation of Germanium and Silicon surfaces (100): A comparative study through DFT methodology," *IOP Conf. Ser. Mater. Sci. Eng.*, vol. 41, no. 1, pp. 0–10, 2012.

[137] G. Hollinger and F. J. Himpsel, "Oxygen chemisorption and oxide formation on Si(111) and Si(100) surfaces," *J. Vac. Sci. Technol. A Vacuum, Surfaces, Film.*, vol. 1, no. 2, pp. 640–645, Apr. 1983.

[138] W. S. M. Werner, W. Smekal, and C. J. Powell, "NIST Database for the Simulation of Electron Spectra for Surface Analysis (SESSA) - User's Guide," *NIST Database Simul. Electron Spectra Surf. Anal. - User's Guid.*, 2011.

[139] W. S. M. Werner, "Simulation of electron spectra for surface analysis using the partial-intensity approach (PIA)," *Surf. Interface Anal.*, vol. 37, no. 11, pp. 846–860, Nov. 2005.

[140] M. Chudzicki, W. S. M. Werner, A. G. Shard, Y.-C. Wang, D. G. Castner, and C. J. Powell, "Evaluating the Internal Structure of Core–Shell Nanoparticles Using X-ray Photoelectron Intensities and Simulated Spectra," *J. Phys. Chem. C*, vol. 119, no. 31, pp. 17687–17696, Aug. 2015.

[141] W. S. Liu *et al.*, "Wet oxidation of GeSi at 700°C," *J. Appl. Phys.*, vol. 71, no. 8, pp. 4015–4018, 1992.

[142] J. M. Madsen, Z. Cui, and C. G. Takoudis, "Low temperature oxidation of SiGe in ozone: Ultrathin oxides," *J. Appl. Phys.*, vol. 87, no. 4, pp. 2046–2051, 2000.

[143] A. Jablonski and C. J. Powell, "Formalism and parameters for quantitative surface analysis by Auger electron spectroscopy and x-ray photoelectron spectroscopy," *Surf. Interface Anal.*, vol. 20, no. 9, pp. 771–786, 1993.

[144] A. Jablonski, "Comparison of the attenuation lengths and the inelastic mean-free path for photoelectrons in silver," *J. Vac. Sci. Technol. A Vacuum, Surfaces, Film.*, vol. 8, no. 1, p. 106, 1990.

[145] W. S. M. Werner, W. H. Gries, and H. Störi, "Analytical expression describing the attenuation of Auger electrons and photoelectrons in solids," *Surf. Interface Anal.*, vol. 17, no. 10, pp. 693–704, 1991.

[146] H. K. Liou, P. Mei, U. Gennser, and E. S. Yang, "Effects of Ge concentration on SiGe oxidation behavior," *Appl. Phys. Lett.*, vol. 59, no. 10, pp. 1200–1202, 1991.

[147] C. T. Chang and A. Toriumi, "Preferential oxidation of Si in SiGe for shaping Ge-rich SiGe gate stacks," *Tech. Dig. - Int. Electron Devices Meet. IEDM*, p. 21.5.1-21.5.4, 2015.

[148] G. Iovino, S. Agnello, F. M. Gelardi, and R. Boscaino, "Diffusive equilibrium properties of O_2 in amorphous SiO_2 nanoparticles probed via dependence of concentration on size and pressure," *J. Phys. Chem. C*, vol. 118, no. 31, pp. 18044–18050, 2014.

[149] P. E. Hellberg, S. L. Zhang, F. M. D'Heurle, and C. S. Petersson, "Oxidation of silicon-germanium alloys. II. A mathematical model," *J. Appl. Phys.*, vol. 82, no. 11, pp. 5779–5787, 1997.

[150] J. Nyéki, C. Girardeaux, G. Erdélyi, A. Rolland, and J. Bernardini, "Equilibrium surface segregation enthalpy of Ge in concentrated amorphous SiGe alloys," *Appl. Surf. Sci.*, vol. 212–213, no. SPEC., pp. 244–248, 2003.

Appendix A

A.1   Idealized Spectrometer

To obtain an expression for differential peak intensity that can be integrated to yield a useful expression for total peak intensity, some simplifying assumptions will be made. These assumptions are based on an idealized spectrometer.
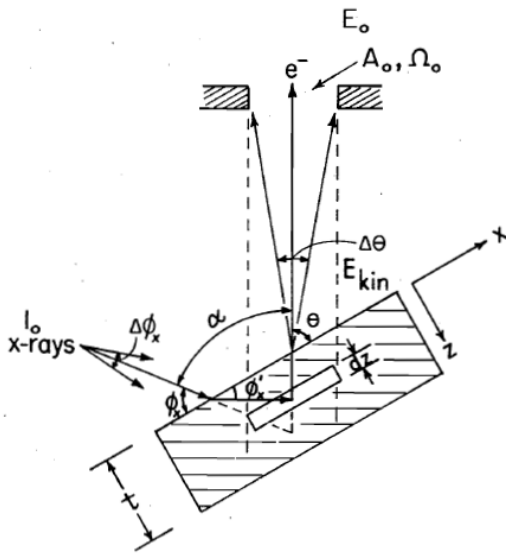

Figure A.1.1: Idealized spectrometer geometry for calculating photoelectron peak intensities from solid specimens.

- Assume X-ray flux is some constant I_o over the entire surface

- Assume the target specimen is atomically flat

- Assume the specimen in polycrystalline to avoid single-crystal anisotropies in emission

- An exponential inelastic attenuation law is assumed

  o $N = N_o \exp\left[-l / \Lambda_e (E_{kin})\right]$

- Elastic electron scattering effects are neglected

- For a given kinetic energy, the electron spectrometer is assumed to act as though a mean solid angle Ω_o is applicable over all specimen volume included in the projection of an effective aperture A_o along the mean electron emission direction (both Ω_o and A_o may be functions of the kinetic energy)

- The mean emission direction is assumed to be at an angle θ with respect to the surface

- The exciting radiation is incident at an angle φ_x with respect to the surface, and, due to refraction, the internal angle φ'_x must be less than φ_x. Such refraction and reflection effects only occur for incidence angles of less than or equal to one. Refraction and reflection will be ignored in this simplified model

- The angle α between the mean incidence and exit directions is held fixed at between approximately 45 – 105 degrees in most current XPS spectrometer